Modeling Diffusion, Deformation and Fracture in Thin Film Electrodes

By

Hamed Haft Baradaran

A DISSERTATION SUBMITTED IN PARTIAL FULFILLMENT OF THE REQUIREMENTS FOR THE DEGREE OF DOCTOR OF PHILOSOPHY IN THE SCHOOL OF ENGINEERING AT BROWN UNIVERSITY

PROVIDENCE, RHODE ISLAND

MAY 2013

This dissertation by Hamed Haft Baradaran is accepted in its present form

by the School of Engineering as satisfying the

dissertation requirement for the degree of Doctor of Philosophy.

Date_____ _____

Huajian Gao, Advisor

Recommended to the Graduate Council

Date_____ _____

Brian W. Sheldon, Reader

Date_____ _____

Kyung-Suk Kim, Reader

Approved by the Graduate Council

Date_____ _____

Peter Weber, Dean of the Graduate School

Vita

Hamed Haft Baradaran received his B.S. degree in Civil Engineering in 2006 and his M.S. degree in Structural Engineering in 2008 from Sharif University of Technology, Iran. In 2009, he was awarded James R. Rice fellowship to pursue his Ph.D. in Solid Mechanics at Brown University.

Acknowledgements

This thesis is an outcome of my rewarding stay as a Ph.D. student in Solid Mechanics group at Brown. My most sincere thanks go to my advisor, Prof. Huajian Gao, for his guidance, support and encouragement during my research. I have always benefited from his inspiring vision over the course of my studies at Brown.

I would like to particularly thank the members of the thesis committee, Prof. Sheldon and Prof. Kim, for reviewing my work. The fruitful collaboration with Prof. Sheldon, Prof. Curtin, Dr. X. Xiao, and Dr. M. W. Verbrugge is gratefully acknowledged. I would like also to appreciate helpful discussions with Prof. J. Song, and Dr. S. K. Soni.

Finally, I would like to thank my parents for their everlasting love and support.

Table of Contents

List of Tables vi

List of Figures vii

1. Introduction 1

2. Atomistic-based continuum modeling of strongly-coupled diffusion, stress, and solute concentration 7

2.1. Continuum modeling of diffusion 9

2.1.1. Chemo-mechanical potential 10

2.1.2. Diffusion-induced stresses 14

2.1. 3. Stress dependent activation energy for diffusion 15

2.1.4. Generalized diffusion equation 17

2.1.5. Numerical solution methodology 19

2.2. Model validation via comparison with molecular dynamics simulation 20

2.2.1. Properties of H in Ni 20

2.2.2. Simulation of H Charging of Ni 22

2.3. Results and Analysis 26

2.3.1. Stress dependence of the activation energy 29

2.3.2. Concentration dependence of the solute binding energy 30

2.3.3. Effect of stoichiometric maximum limit 32

2.3.4. Comparison with the classical diffusion equations 33

2.3.5. Applicability and limitations for lithium diffusion in silicon 37

2.4. Summary 38

3. A surface locking instability for atomic intercalation into a solid 40

3.1. Surface locking instability for a free-standing plate 41

3.2. Surface locking instability for a cylindrical wire 46

3.3. Surface locking instability for a spherical particle 50

3. 4. Discussion 54

4. A critical size for Si thin film patterned electrodes, and interpretation of stress measurements 56

4.1. Crack spacing and emergence of a critical island size 59

4.2. A modified Stoney equation in the presence of interfacial sliding 64

4.2.1. Two-dimenisonal modifed Stoney equation 65

4.2.2. Three-dimensional modified Stoney equation 69

4.3. Interpretation of *in-situ* stress-measurements in Si patterned islands 76

4.4. Summary 82

5. Critical size for interfacial delamination of patterned Si thin film electrodes 83

5.1. Modification of the conventional theory of film delamination 85

5.2. Nucleation and growth of edge delamination cracks in the presence of large scale interfacial sliding 90

5.2.1. Plane strain analysis 90

5. 2.2. Axisymmetric analysis 96

5.3. Analysis of center delamination cracks in the presence of large scale interfacial sliding 102

5.3.1. Plane strain analysis 102

5.3.2. Axisymmetric analysis 111

5.4. Summary 116

6. Ratcheting of Si island electrodes on substrate due to cyclic intercalation 117

7. Concluding Remarks 130

7.1. Summary of the results 130

7.2. Limitations of the present work, and possible future research directions ... 133

Appendix 136

Bibliography 139

Parts of this thesis have been published in the following peer-reviewed publications:

- H. Haftbaradaran, J. Song, W.A. Curtin, H. Gao. *Continuum and atomistic models of strongly coupled diffusion, stress, and solute concentration.* Journal of Power Sources, 2011. **196**(1): p. 361-370.

- H. Haftbaradaran, H. Gao, W.A. Curtin. *A surface locking instability for atomic intercalation into a solid electrode.* Applied Physics Letters, 2010. **96**(9).

- H. Haftbaradaran, S. K. Soni, B.W. Sheldon, X. Xiao, H. Gao, *Modified Stoney Equation for Patterned Thin Film Electrodes on Substrates in the Presence of Interfacial Sliding.* Journal of Applied Mechanics, 2012. **79**(3).

- X. Xiao, P. Liu, M. W. Verbrugge, H. Haftbaradaran, H. Gao, *Improved cycling stability of silicon thin film electrodes through patterning for high energy density lithium batteries.* Journal of Power Sources, 2011. **196**(3): p. 1409-1416.

- S. K. Soni, B. W. Sheldon, X. Xiao, M. W. Verbrugge, A. Dongjoon, H. Haftbaradaran, H. Gao, *Stress Mitigation during the Lithiation of Patterned Amorphous Si Islands.* Journal of the Electrochemical Society, 2012. **159**(1): p. A38-A43.

- H. Haftbaradaran, X. Xiao, M.W. Verbrugge, H. Gao, *Method to deduce the critical size for interfacial delamination of patterned electrode structures and application to lithiation of thin-film silicon islands.* Journal of Power Sources, 2012. **206**: p. 357-366.

- H. Haftbaradaran, H. Gao, *Ratcheting of silicon island electrodes on substrate due to cyclic intercalation.* Applied Physics Letters, 2012. **100**(12).

List of Tables

2.1. Numerical values of the model parameters 21

5.1. Numerical estimates of the minimum length of the pre-existing crack required for full delamination for different island sizes based on the plane strain analysis 110

5.2. Numerical estimates of the minimum length of the pre-existing crack required for full delamination for circular islands of different sizes 116

List of Figures

2.1: A solid plate under atomic intercalation. (a) A plate of thickness *w* under uniform charging flux J_n on both of its faces. (b) The corresponding atomistic problem for H diffusion in Ni with the simulation cell being free along *x* direction and periodic along *y* and *z* directions. During simulations, flux J_n of H atoms enter the simulation cell from the top surface while a reflecting boundary condition is imposed at the bottom surface 14

2.2: Concentration-dependent binding energy $\Delta\mu_0$ as a function of $\tilde{c} = c / c_{\max}$ at 0 K .. 25

2.3: Activation energy barrier of diffusion as a function of the normal stress acting perpendicular to the diffusion direction 25

2.4: Actual flux data versus the predictive relation as a function of time 26

2.5: Concentration profile across the thickness; dots are MD results and solid lines are the continuum model predictions 28

2.6: Concentration profile across the thickness; atomistic simulation vs. continuum predictions neglecting the stress-diffusivity coupling 30

2.7: Concentration profile across the thickness; atomistic simulation vs. continuum model neglecting the concentration dependence of the binding energy of the solution .. 31

2.8: Concentration profile across the thickness; atomistic simulation vs. continuum model without the saturation cap, Equation (2.20). 33

2.9: Concentration profile across the thickness; atomistic simulation vs. classical model without saturation cap, Equation (2.21). 36

2.10: Concentration profile, atomistic simulation vs. classical model with saturation cap, Equation (2.22). 37

3.1: Surface locking in a planar electrode under galvanostatic charging. (a) A plate electrode is subject to a uniform current density on its faces. (b) Evolution of the solute concentration profile in the subcritical case of $\mu\tilde{i}_n = 7.2$. (c) Evolution of the solute concentration profile in the supercritical regime of $\mu\tilde{i}_n = 7.7$. (d) Evolution of the surface gradient of solute concentration for various values of $\mu\tilde{i}_n$. The results indicate that surface locking occurs above a critical value between $7.7 \geq (\mu\tilde{i}_n)_{cr} > 7.2$, in agreement with the analytical solution which predicts $(\mu\tilde{i}_n)_{cr} = e^2 \approx 7.39$. 45

3.2: Surface locking in a cylindrical electrode under galvanostatic charging. (a) A cylindrical wire is subject to a uniform current density on its surface. (b) Evolution of the solute concentration profile in the subcritical case of $\mu\tilde{i}_n = 4.4$. (c) Evolution of the solute concentration profile in the supercritical regime of $\mu\tilde{i}_n = 5.2$. (d) Evolution of the surface gradient of solute concentration for various values of $\mu\tilde{i}_n$. The results indicate that surface locking occurs above a critical value between $5.2 \geq (\mu\tilde{i}_n)_{cr} > 4.4$, in agreement with the theoretical analysis. 50

3.3: Surface locking in a spherical electrode under galvanostatic charging. (a) A sphere is subject to a uniform current density on its surface. (b) Evolution of the solute concentration profile in the subcritical case of $\mu\tilde{i}_n = 5.1$. (c) Evolution of the solute

concentration profile in the supercritical regime of $\mu\tilde{i}_n = 6.9$. (d) Evolution of the surface gradient of solute concentration for various values of $\mu\tilde{i}_n$. The results indicate that surface locking occurs above a critical value between $6.9 \geq \mu\tilde{i}_n > 5.1$, in agreement with the theoretical analysis. 54

4.1: A 100 nm-thick Si film on Cu substrate after 12 cycles (Ref. [22]). 58

4.2: (a) A periodically cracked continuous thin film on a thick substrate; (b) Free-body diagram for half-period of the cracked film. 60

4.3: Evolution of nominal stress σ_{nom} (see Equation 4.6) vs. capacity in (a) 7 μm, and (b) 17 μm islands. (Ref. [132]). 62

4.4: Micrographs demonstrating lateral expansion and contraction of Si islands on Ti current collector due to lithiation and delithaition. (a) As-deposited 17 μm x 17 μm Si islands; (b) Lateral dimensions of the Si islands expand by about 30% parallel to the substrate, demonstrating sliding along the interface; (c) Si islands return to their original size after delithiation. The scale bar is 50 μm (Ref. [136]). 63

4.5: Modified Stoney equation for two-dimensional patterned films on substrate. (a) The geometry of the problem, and (b) the reciprocity theorem for determining the curvature of the system. 66

4.6: Modified Stoney equation for two-dimensional patterned films on substrate: comparison of FEM calculations and theoretical predictions of curvature for two-dimensional patterned films on substrate. 69

4.7: Modified Stoney equation for three-dimensional patterned films on substrate, and comparison with FEM calculations. (a) The geometry of the problem, and (b) the reciprocity theorem for determining the curvature of the system. 70

4.8: Comparison of FEM calculations and theoretical predictions of curvature for (a) circular patches where the solid line is the theoretical prediction; (b) square patches where the solid line is based on a fitting scheme. 74

4.9: Nominal stress (Equation 4.6) vs. capacity. Solid lines are fits obtained from full sliding model by tuning the interfacial strength τ_0 (Equation 4.26). The dashed, and dotted lines are predictions obtained respectively from Equations (4.27), and (4.28), without allowing for lateral expansion of the islands. 79

4.10: Nominal stress (Equation 4.6) vs. capacity. Solid lines are predictions based on partial sliding along the interface (Equation 4.32). Deviation of the predicted values form the experiment suggest that plastic deformation might have happened during lithiation.

..... 81

5.1: SEM images of patterned Si islands surface morphology after 30 cycles, showing that (a) while 7 μm x 7 μm islands stay well-adhered to the substrate (scale bar = 10 μm), (b) 40 μm x 40 μm islands have delaminated away from the substrate (scale bar = 20 μm) (Ref. [22]). 85

5.2:. Schematic of an edge delamination crack in a thin film on substrate in the presence of large scale interfacial sliding. (a) The crack grows in a steady state manner when the film width is much larger than the interfacial sliding zone at the film edge. (b) The interfacial delamination becomes dependent on the island size as the sliding zones from island edges overlap. In this case, the energy release rate for interfacial delamination is expected to decrease as the island size is reduced. 88

5.3: Schematic of (a) a Si island on substrate with edge delamination cracks and (b) free-body diagram of the island. 91

5.4: Plane strain analysis of interfacial delamination of a Si island on substrate. Elastic energy release rate and surface energy growth rate *vs*. crack length for various island sizes. 92

5.5: Plane strain analysis of interfacial delamination of a Si island on substrate. (a) Length of the arrested edge crack as a function of the island size; (b) Changes in the elastic energy and surface energy as a function of the crack length for different island sizes. 94

5.6: Schematic of (a) a Si circular island on substrate with an annular edge crack and (b) a free-body diagram of the island. 98

5.7: Axisymmetric analysis of interfacial delamination of a circular Si island on substrate. Elastic energy release rate and surface energy growth rate *vs*. crack length for various island sizes. 101

5.8: Axisymmetric analysis of interfacial delamination of a circular Si island on substrate. (a) Length of the arrested edge crack as a function of the island size; (b) Changes in the elastic energy and surface energy as a function of the crack length for different island sizes. 102

5.9: Schematic of (a) a Si island on substrate with a center crack an (b) a free-body diagram of the island. 103

5.10: Plane strain analysis of interfacial delamination of a Si island on substrate with a center crack at the interface: (a) Elastic energy release rate and surface energy growth rate *vs*. crack length for various island sizes; Total elastic energy of the island, total surface energy of the system and their changing rates associated with crack growth for (b) $l/l_{cr}^{*}=1.1$, (c) $l/l_{cr}^{*}=2/\sqrt{3}$, (d) $l/l_{cr}^{*}=1.5$; (e) Phase diagram indicating whether a preexisting crack will grow or not, and if so whether it will lead to full delamination, for given crack length and island size. 109

5.11: Schematic of (a) a circular Si island on substrate with a penny-shaped center crack and (b) a free-body diagram of the island. 113

6.1: Schematic of a Si island on substrate under cyclic lithiation and delithiation. (a) Geometry of the entire system and (b) the free-body diagram of half of the island. Free-body diagrams at the end of (c) intercalation half-cycles and (d) deintercalation half-cycles. 119

6.2: The rigid-perfectly plastic cohesive law used for modeling the interfacial sliding with differential sliding resistance during lithiation and delithiation half cycles. Here, τ_0 denotes the interfacial sliding strength during the lithiation half-cycle and τ_0' denotes the sliding strength during the delithiation half-cycle. 120

6.3: Finite element simulations of deformation in a periodic array of islands. Ratcheting of the islands after (a) 1 cycle and (b) 10 cycles with differential sliding resistance and $l > l_{cr}$. Ratcheting of the islands after (c) 1 and (d) 10 cycles with differential yield stress for Si and $l > l_{cr}$. Elastic reversible response of an array of islands with $l < l_{cr}$ after (e) 1 cycle and (f) 10 cycles. The thickness direction has been magnified by a factor of 4. 123

6.4: Deformation within half of a single island, after (a) 1, (b) 2, (c) 5, and (d) 10 cycles with differential sliding resistance and $l > l_{cr}$. The thickness direction has been magnified by a factor of 2. The figure shows incremental accumulation of compressive deformation with cycling. 124

6.5: Displacement of the edge of the island (point A in Figure 6.1), in absolute value, vs. the number of cycles. Comparison of the theoretical predictions with the FEM calculations. 125

6.6: Plan view of a 250 nm thick Si continuous film cycled at C/2.5 rate. (a) Film has fractured after 1 cycle. (b) The gap between the islands has substantially widened after 30 cycles. The matching edges and roughened surface of the islands suggest that the lateral dimensions of the islands have shrunk. The scale bars correspond to 2 μm of the actual dimensions (from Ref. [15]). 127

6.7: Tensile ratcheting deformation within half of a single island, after (a) 1, (b) 2, (c) 5, and (d) 10 cycles with differential sliding resistance and $l > l_{cr}$ The thickness direction has been magnified by a factor of 2. The figure shows incremental accumulation of tensile deformation. 129

Chapter 1

Introduction

Rechargeable battery cells have recently received much attention due to their broad potential applications in a variety of technologies including military, automobile, aerospace and medical industries [1]. Among various types of rechargeable batteries, lithium-ion (Li-ion) cells featuring higher energy capacity, higher operating voltage, lower self-discharge and lower maintenance requirement have become the most widely used secondary battery systems [2, 3]. Significant research has been directed towards increasing the charge and energy capacity of Li-ion batteries [1]. It has been shown that a noticeable increase in the charge capacity of batteries is achievable using Li-alloy (Li_xM; M = Sn, Si, Ge, Al, etc) anodes [4]. Silicon (Si) possesses the highest known theoretical charge capacity (4200 $mAhg^{-1}$) corresponding to the formation of $Li_{22}Si_5$, but this capacity is accompanied by a nearly 400% volume expansion [5]. Very large mechanical stresses associated with such a huge volume change during lithiation and delithiation are responsible for poor cycling behaviors of the Si anodes due to pulverization, fracture, loss of integrity and loss of electric contact with current collector. This major liability has obstructed the way toward widespread application of the Si anodes. In order to circumvent problems associated with mechanical degradation of Si electrodes, various approaches have been under investigation. For example, Si

composites with non-metallic matrices [6], such as TiN [7] and TiB_2 [8], and metallic composites, such as Mg_2Si [9] and SiAg [10], as well as Si-Sn alloys of different compositions [11] have been investigated as anode in Li-ion batteries. Reduction of the particle size to submicron regime has been shown promising in many studies. For example, Gratez, et al. [12, 13] investigated the electrochemical performance of nanostructured Si and Ge thin films on metallic substrates, and found improved capacity retention in nanofilms. Electrochemical and mechanical performance of thin film electrodes on substrates have also been a subject of broad investigation [14, 15]. A crucial step in understanding the mechanical behavior of Si electrodes has been taken by Sethurman et al.[16], and Soni et al. [17] via *in-situ* stress measurements on Si thin films during cycling. Their measurements suggest that Si yields during lithiation (in compression) at ~1.7 GPa, and delithiation (in tension) at ~1 GPa [16]. The stress-potential coupling in thin film electrodes [18], the effect of Li content on the biaxial modulus during cycling [19], and that of thickness on the charging capacity and yield stress of Si [17] have also been addressed in recent experiments.

A commonly observed phenomenon during cycling of thin film electrodes is through-the-thickness cracking, occasionally accompanied with delamination of the cracked film patches from the substrate. Morphology of crack patterns in Si [20], and Ti-Si thin films [21] of different film thicknesses within the submicron regime has been studied. While cracks have been observed in Si films as thin as 100 nm on Cu substrate [22], a systematic study of Si thin films with different thicknesses on stainless steel substrate has suggested that 100 nm thick films do not fracture after cycling up to 10

cycles, while thicker films do fracture after the same number of cycles [20], concluding that there is a critical size below which through-the-thickness cracking becomes impossible [13, 23, 24]. The effect of cycling rate on the fracture of thin film electrodes has been studied by Soni et al [23]. It has been suggested that substrate roughness could also contribute to the electrochemical performance of thin film electrodes [25, 26].

Nanowire electrodes made of various materials have also been thoroughly investigated [27-34]. Initially, it was shown that Si nanowires of 89 nm mean diameter can be charged up to nearly the theoretical capacity, at sufficiently low cycling rate with improved cycling efficiency [28]. In crystalline Si nanopillars, it has been observed that anisotropic expansion during initial lithiation [35, 36] could induce fracture [30, 37]. It has been suggested that Li embrittlement is responsible for a "leapfrog" cracking mechanism in ZnO nanowires [34]. In contrast, in SnO_2 nanowires, a high density of mobile dislocations is nucleated at the lithiation front and propagates along the length of the nanowire. A summary of the *in-situ* transmission electron microscopy observations during Li cycling of nanowires can be found in [38].

Besides numerous experimental studies, of which a brief summary was discussed above, there has been significant effort with the aim of modeling the coupled mechanical and electrochemical processes involved in Li-ion batteries. An initial effort along this line of thought, dealing with large deformation within electrodes as well as electrochemical processes, has been presented in [39, 40]. There have been various attempts to develop continuum models of diffusion-induced stresses [41-50]. Most of these models are subject to restrictions such as low solute concentrations, small stresses,

small deformation, and mostly ignore the coupling between the electrochemistry and mechanics. Recently, a rather sophisticated model accounting for coupling between various physical phenomena in Li-ion battery electrodes has been developed by Bower et al. [51, 52].

There exist numerous theoretical studies dealing with modeling of electrodes, mostly at the particle level. Theoretical models have been developed to predict critical sizes to avoid fracture in electrodes [13, 24, 53-55]. The effects of cycling rate with particular attention to crack nucleation and propagation has also been discussed in a number of papers [23, 53, 54, 56, 57]. Anisotropy effects on the kinetics of lithiation in crystalline Si nanopillars have been modeled in [36, 58]. Coupled large deformation and plasticity models have also been employed to predict deformation within the electrode particles [59]. Cohesive law models have been utilized to model progressive fracture of graphitic particle electrodes [60]. Fracture and delamination in composite electrodes have also been investigated [61].

In this thesis, we will focus on some mechanics aspects of energy-storage materials with particular attention to the Si electrodes in Li-ion batteries. Organization of this work is as follows:

In Chapter 2, we will develop an atomistic-based continuum model for diffusion within solid electrodes, accounting for the effect of the interplay between stress field and diffusivity, binding energy of solute atoms to the host atoms and effect of the maximum attainable stoichiometry. Our model is then tested against molecular dynamics simulations of hydrogen diffusion in nickel. The model is shown to give predictions in

excellent agreement with atomistic simulations. Employing this model, we then assess the role played by each of the individual effects above on the overall charging behavior. Limitations and applicability of the model to the Si electrodes in Li-ion batteries are discussed.

In Chapter 3, we will focus on the effect of coupling between the stress field within an electrode particle and diffusivity of the guest atoms in the host matrix. We will show that a surface locking instability emerges as a result of this coupling under constant charging flux, i.e. galvanostatic charging. This instability causes the inserted atoms to jam near the surface and does not allow them to get inside the electrode. We will discuss this instability in electrode particles of simple geometries. The new finding is that once the product of the electrode's characteristic size and charging current exceeds a critical value, the normal diffusion process is locked leading to accumulation of the inserted atoms within a boundary layer near the surface of the particle.

Our discussion will then turn to patterned Si thin film electrodes on metallic substrates in Chapter 4, which will remain the subject for the rest of this thesis. We will start by discussing size effects in patterned electrodes dealing with the lateral dimension of the islands in a patterned film, taking into account sliding along the interface between Si and the underlying metallic substrate. It is discussed why the characteristic spacing for fracture is about two orders of magnitude larger than the film thickness, in contrast to the conventional film-substrate systems where the crack spacing is expected to be on the same order as the film thickness, especially when the film is softer than the substrate. We then show that islands whose lateral size is below a critical size allow reversible

deformation during cycling. Interpretation of stress-curvature measurments in such electrodes is also discussed, using a modified Stoney equation whose derivation is presented in the same chapter.

In Chapter 5, we will address the issue of interfacial delamination in patterned thin films allowing for interfacial sliding. It is shown that in the presence of interfacial sliding, a size effect can be recognized: once the lateral size of the islands becomes larger than a critical size which can be much larger than the island thickness, spontaneous interfacial debonding becomes energetically favorable.

In Chapter 6, we will discuss a low-cycle fatigue mechanism, called ratcheting, associated with incremental accumulation of deformation within the patterned islands. This phenomenon happens in the presence of non-symmetrical variations in yield stress of Si and/or the interfacial sliding strength during lithiation and delithiation half-cycles. We will present theoretical as well as numerical finite element calculations to demonstrate this effect. The results are discussed together with relevant experimental observations.

Chapter 7 concludes this thesis with discussions on some limitations of the models/approaches presented in this thesis, as well as on possible theoretical and experimental studies in the future.

Chapter 2

Atomistic-based continuum modeling of strongly-coupled diffusion, stress, and solute concentration

There exists a significant volume of theoretical work dealing with continuum modeling of diffusion in battery electrodes in the literature. Among them, numerous continuum thermodynamics and kinetics models have been proposed such as the theoretical framework of porous electrodes [62, 63] and the dual foil cell-sandwich model [64, 65]. In addition, a large volume of publications has been devoted to the study of stress generation, deformation and fracture during diffusion. Study of diffusion-induced stresses based on an analogy with thermal stresses can be traced back to the work of Prussin [66]. The study was later broadened to include the development of stresses during mass transfer in thin plates, solid cylinders and spheres, where the stress-diffusion coupling was considered by including the elastic inclusion energy of solute in the chemical potential [50, 67]. During the past decade, an increasing number of continuum models of diffusion induced stresses during charging/discharging of electrodes has been developed [39-42, 44, 45, 68], some even accounting for the effects of surface tension and surface modulus [46, 69].

Despite these developments, continuum models of diffusion under very large stresses and high solute concentrations usually face the challenge of strongly nonlinear system behavior. Validation of such models is often subject to limitations in experimental techniques. For instance, Christensen and Newman [39] presented an integrative model accounting for a number of different physical effects whose experimental validations are still lacking. Moreover, most of the existing models are either strictly applicable only in the limit of dilute concentrations [41, 42, 44, 45] or do not account for non-conventional stress-diffusivity couplings that could be of importance for concentrated solutions and large stresses [39, 40, 68].

In this chapter, we take an atomistic-based approach to developing continuum models of strongly nonlinear and coupled diffusion under large stresses and high solute concentrations. The model includes the effects of solute-induced stresses on the activation energy of solute diffusion, an upper limit for solute concentration, the interaction energy between solute and host atoms, as well as the effect of the solute concentration on the Young's modulus of the host material. On the other hand, we neglect the effects of surface tension and surface modulus [46, 69] so that our model is really trying to capture the "bulk" behavior starting just inside the surface (associated with the flow of the material into the "bulk" due to an imposed flux at the "real" interface). In this way, our model is not a nanoscale model and has no special kinetics or energetics at the continuum surface. We will then compare the continuum model with atomistic simulations which are performed at nanoscale. The simulations have been specially designed to exclude complications at a real electrolyte/material interface by

artificially imposing an input flux inside the material just away from the outermost surface atomic layer, where bulk thermodynamics and kinetics applies (see Ref. [70] for the details of the atomistic simulations).

This chapter is organized as follows. In Section 2.1, we introduce a continuum analytical model taking into account the four nonlinear features mentioned above. In Section 2.2, a brief discussion of the general properties of hydrogen in nickel as a test system is presented along with a concise description of the atomistic simulations regarding H-Ni materials system, and simulation of the charging process. Section 2.3 contains our comparison of the analytical model against the atomistic simulations, and demonstrates the role of the factors noted above in achieving quantitative predictions in the continuum model. The validated continuum model then enables us to investigate the influence of each individual physical effect on the overall charging process separately, which is presented in Section 2.3. A comparative study between the MD results and two versions of the classical models is also presented in Section 2.4. We conclude this section with a discussion on the applicability of the present model to the case of Li-ion batteries with Si anodes. A summary of our results is given in Section 2.5.

2.1. Continuum modeling of diffusion

For simplicity, consider one-dimensional diffusion in a plate under large stresses and high solute concentrations. We start by introducing a chemo-mechanical potential including the effect of high solute concentrations on the entropy of the system, the work

required to insert an inclusion into an elastic matrix, and the concentration-dependent heat of solution. The diffusion-induced stresses are then presented for an infinitely extended free standing plate using small-deformation theory, considering that the Young's modulus of the plate may vary with the solute concentration. We then introduce the stress-diffusivity coupling through the effect of internal stress field on the activation energy of diffusion. Finally, the generalized governing 1-D diffusion equation is derived and the solution methodology is discussed.

2.1.1. Chemo-mechanical potential

To demonstrate the basic approach of simulation-based continuum modeling, we consider interstitial diffusion of solute atoms in a host solid. The interstitial sites of the host solid form a sublattice. With respect to this sublattice, the diffusion of the solute atoms can be viewed as a substitutional mechanism. The total number of interstitial sites in the original host lattice is assumed to be preserved.

In the continuum modeling of diffusion in solids, the drift velocity $\boldsymbol{v}$ and hence the flux of the diffusing species in the host material is given by [42, 71, 72]

$$J = c\boldsymbol{v} = -Mc\nabla\mu^*, \tag{2.1}$$

where M is the mobility of the diffusing component, c is the solute concentration and μ^* is the chemo-mechanical potential incorporating the chemical and mechanical energies of the system. In the presence of internal stresses, the chemo-mechanical potential is expressed in terms of the chemical potential of the solute atoms μ_s and

vacancies μ_v, partial molar volume of the solute Ω and the hydrostatic stress in the host solid σ_h as [71, 73]

$$\mu^* = \mu_s - \mu_v - \Omega\sigma_h, \tag{2.2}$$

where

$$\mu_i = \mu_i^0 + RT \log a_i . \tag{2.3}$$

Here, $i \equiv s, v$ corresponds to the solute and vacancy components respectively, μ_v^0 is the free energy of the host solid accommodating one mole of the vacant interstitial sites, μ_s^0 is the free energy of the same system when the interstitial sites are occupied by the solute atoms, R is the gas constant and T is the absolute temperature. The activity a_s accounts for the interaction energy between the host and solute atoms. A similar treatment of vacancies can be found in the thermodynamic description of adsorption equilibrium via vacancy solution theory [74, 75], where activity of the vacancies is interpreted as the interaction between the adsorbate molecules and the host solid [76-78].

Recognizing the existence of a stoichiometric maximum concentration $c_{\max}$, activities of the components are related to their site fractions through $a_s = \gamma_s \tilde{c}$ and $a_v = \gamma_v(1-\tilde{c})$, where $\tilde{c} = c / c_{\max}$ and, γ_v and γ_s are the activity coefficients of the vacancies and solute atoms respectively.

Therefore, the chemo-mechanical potential takes the following form

$$\mu^* = \mu_0^{sv} + RT\log\frac{\tilde{c}}{1-\tilde{c}} - \Omega\sigma_h + RT\log\frac{\gamma_s}{\gamma_v}, \tag{2.4}$$

where $\mu_0^{sv} = \mu_0^s - \mu_0^v$ is a constant. Equation (2.4) accommodates three important physical effects associated with high solute concentrations and large stresses as follows.

The second term on the right hand side of Equation (2.4) is due to the entropy of a simple solution where the solutes occupy a fixed set of sites, such as interstitial or substitutional sites in the host material. For dilute solutions, where $\tilde{c} << 1$, this term reduces to the usual form $RT\log\tilde{c}$. However, the entropy of the system should reduce to zero as all the available sites in the host are filled with the solutes and so it is not possible to reach the saturation point. Introduction of this effect enables the present model to recognize a saturation limit for the host solid. Throughout this paper, this effect is referred to as the saturation effect.

The third term on the right hand side of Equation (2.4) is the elastic energy associated with insertion of an inclusion of volume Ω into the matrix under the hydrostatic stress σ_h. This term was considered by Li [67], and is well-established in other contexts including diffusion around dislocations [79, 80]. This effect is interchangeably referred to as the effect of hydrostatic stress or inclusion energy in the rest of this chapter.

The last term on the right hand side of Equation (2.4) represents the deviation of the solution behavior from an ideal solution which is ideal over the entire range of its composition [81]. This term reduces to a constant for dilute solutions and vanishes for an ideal solution. However, at high solute concentrations, the change in the chemical

environment of the solution influences the interaction energy of the solute and host atoms. Since the activity coefficients γ_v and γ_s are related through the Gibbs-Duhem equation, they are determined based on the excess molar Gibbs free energy of the solution $G_{Ex}(\tilde{c})$ via $\frac{\tilde{c}(1-\tilde{c})}{RT}\frac{d^2G_{Ex}}{d\tilde{c}^2}=\frac{\partial\log\gamma_s}{\partial\log\tilde{c}}=\frac{\partial\log\gamma_v}{\partial\log(1-\tilde{c})}$, subject to the conditions $\gamma_s\to 1$ as $\tilde{c}\to 1$ and $\gamma_v\to 1$ as $\tilde{c}\to 0$ [81]. Therefore, one can simply verify that Equation (2.4) can be rearranged in the following form

$$\mu^* = \mu_0 + RT\log\frac{\tilde{c}}{1-\tilde{c}} - \Omega\sigma_h + \Delta\mu_0(\tilde{c}), \tag{2.5}$$

where $\mu_0=\mu_0^{sv}+(dG_{Ex}(0)/d\tilde{c})$ is the chemical potential of an infinitely dilute solution, and $\Delta\mu_0(\tilde{c})=(dG_{Ex}(\tilde{c})/d\tilde{c})-(dG_{Ex}(0)/d\tilde{c})$ is the concentration-dependent binding energy between the solute particles and the host atoms as a function of the local concentration, which vanishes for an infinitely dilute solution. In the following section, we adopt the two-parameter Margules equation for the excess free energy of a binary solution [81],

$$G_{Ex}(\tilde{c})=\tilde{c}(1-\tilde{c})[A_0\tilde{c}+B_0(1-\tilde{c})], \tag{2.6}$$

hence the concentration-dependent binding energy of the solution is given by

$$\Delta\mu_0(\tilde{c})=2(A_0-2B_0)\tilde{c}-3(A_0-B_0)\tilde{c}^2, \tag{2.7}$$

where A_0 and B_0 are the parameters of the Margules equation.

For an ideal dilute solution, where $\Delta\mu_0(\tilde{c}) = 0$ and $\tilde{c} << 1$, Equation (2.5) reduces to the classical chemical potential [42, 49, 50, 67].

2.1.2. Diffusion-induced stresses

Before proceeding to derive the generalized governing diffusion equation, we need to estimate the stress fields within the host solid. In this paper, we specialize the formulation to the case of an infinitely extended free-standing plate of width *w* subject to equal and uniform charging current densities on the side faces of the plate, as shown in Figure 2.1.

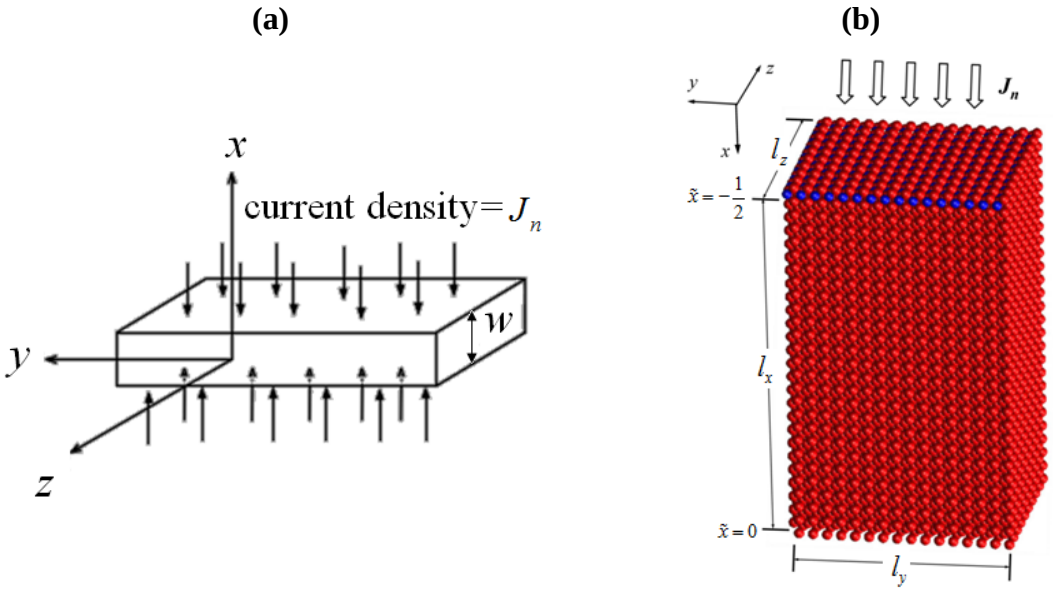

Figure 2.1: A solid plate under atomic intercalation. (a) A plate of thickness *w* under uniform charging flux J_n on both of its faces. (b) The corresponding atomistic problem for H diffusion in Ni with the simulation cell being free along *x* direction and periodic along *y* and *z* directions. During simulations, flux J_n of H atoms enter the simulation cell from the top surface while a reflecting boundary condition is imposed at the bottom surface.

The plate material is assumed to be an isotropic homogeneous linear elastic solid with Young's modulus E and Poisson's ratio ν. The Young's modulus of the material can be greatly affected as the solute concentration increases within the plate [82, 83] and so here we explicitly consider a concentration dependent Young's modulus $E(c)$. Following an analogy between thermal stresses and diffusion-induced stresses [41, 42, 49, 50, 66, 67], the biaxial stress in the plate at position *x* through the plate thickness is given by

$$\sigma_b(x) = \sigma_{yy}(x) = \sigma_{zz}(x) = \frac{E\Omega}{3(1-\nu)}\left[\frac{(Ec)_{avg}}{E_{avg}} - c(x)\right], \tag{2.8}$$

where $(Ec)_{avg} = \frac{1}{w}\int_{-w/2}^{w/2} E(c(x))c(x)\,dx$, $E_{avg} = \frac{1}{w}\int_{-w/2}^{w/2} E(c(x))\,dx$ and hence $\frac{(Ec)_{avg}}{E_{avg}}$ is the modulus-weighted average concentration in the plate. We assume that the plate faces are traction-free and thus $\sigma_{xx} = 0$. Therefore the hydrostatic stress σ_h in the plate is two-thirds of the biaxial stress,

$$\sigma_h(x) = \frac{2E\Omega}{9(1-\nu)}\left[\frac{(Ec)_{avg}}{E_{avg}} - c(x)\right]. \tag{2.9}$$

2.1.3. Stress dependent activation energy for diffusion

The diffusivity coefficient $\hat{D}$ is related to the mobility according to

$$\hat{D} = MRT\,. \tag{2.10}$$

Here we consider the effect of the internal stress field on the activation energy of diffusion, as follows. At the atomic scale, diffusion of a solute particle in a crystal lattice

is described as a sequence of jumps from one interstitial site to an adjacent site, during which the diffusing particle must surmount the energy barrier caused by its interactions with the surrounding host atoms. Atomistic and quantum mechanical simulations have shown that this energy barrier is strongly affected by the internal stresses acting on the neighboring crystal atoms in the directions normal to the diffusion [84], suggesting a dependence on the biaxial stress. This effect has been referred to as strain-activated mobility by Aziz et al. [85, 86] who showed that a stress-dependent mobility can cause a kinetically driven surface instability. In Chapter 3, we will demonstrate that such stress-mobility coupling can potentially lead to a surface locking instability in electrodes under galvanostatic intercalation [87].

Denoting the *change* in the activation energy due to the internal stresses as $\Delta E_b(\sigma_b)$, the diffusivity coefficient can be expressed as

$$\hat{D} = D e^{-\frac{\Delta E_b(\sigma_b)}{RT}}, \tag{2.11}$$

where D is the usual stress-free diffusivity. Normally, a tensile stress acting on the neighboring host atoms leads to a reduction in the energy barrier while a compressive stress increases it. Linearization of $\Delta E_b(\sigma_b)$ around the zero-stress value allows Equation (2.11) to be written as

$$\hat{D} = D e^{\frac{\alpha \Omega \sigma_b}{RT}}, \tag{2.12}$$

where α is a positive dimensionless coefficient. In the following section, we allow for a bilinear dependence of the activation energy on the biaxial stress and hence use $\alpha = \alpha_c$ for compressive stresses $\sigma_b < 0$ and $\alpha = \alpha_t$ for tensile stresses $\sigma_b > 0$. Aziz et al. [85] have reported numerical values for the stress-diffusivity coupling through experimental measurements for the amorphous-crystalline interfacial growth of Si along [001] plane.

2.1.4. Generalized diffusion equation

With the chemo-mechanical potential, diffusion-induced stresses, and stress-diffusivity coupling given above, we can now develop the generalized diffusion equation for the simple case of a plate. We start with the fundamental diffusion equation given by

$$\frac{\partial c}{\partial t} + \nabla . \boldsymbol{J} = 0 , \tag{2.13}$$

where $\boldsymbol{J}$ is obtained using Equation (2.1) and the chemo-mechanical potential μ^* is given in Equation (2.5). Since the present problem is essentially one dimensional along the *x*-direction, Equation (2.13) with the aid of Equations (2.1, 2.5, 2.10) takes on the following form

$$\frac{\partial c}{\partial t} = \frac{\partial}{\partial x}\left[\hat{D}\left(\frac{c_{\max}}{c_{\max} - c}\frac{\partial c}{\partial x} - \frac{\Omega c}{RT}\frac{\partial \sigma_h}{\partial x} + \frac{c}{c_{\max}}\frac{1}{RT}\frac{d\Delta\mu_0(\tilde{c})}{d\tilde{c}}\frac{\partial c}{\partial x} \right) \right]. \tag{2.14}$$

Given the stress field in Equations (2.8, 2.9) and the diffusivity $\hat{D}$ in Equation (2.12), Equation (2.14) can be casted into the dimensionless form

$$\frac{\partial \tilde{c}}{\partial \tau} = \frac{\partial}{\partial \tilde{x}}\left[e^{k_1\left(\frac{(\tilde{E}\tilde{c})_{avg}}{\tilde{E}_{avg}} - \tilde{c}\right)} \left(\frac{1}{1-\tilde{c}} + k_2 \tilde{E}(\tilde{c})\tilde{c} - k_2 \frac{d\tilde{E}(\tilde{c})}{d\tilde{c}} \left(\frac{(\tilde{E}\tilde{c})_{avg}}{\tilde{E}_{avg}} - \tilde{c} \right) \tilde{c} + \tilde{c} \frac{d\Delta\tilde{\mu}_0(\tilde{c})}{d\tilde{c}} \right) \frac{\partial \tilde{c}}{\partial \tilde{x}} \right], \quad (2.15)$$

where $\tau = \frac{Dt}{w^2}$ is a dimensionless time, $\tilde{x} = \frac{x}{w}$ is the dimensionless length parameter, $\tilde{E}(\tilde{c}) = \frac{E(c)}{E_0}$ is the Young's modulus normalized with respect to the reference modulus E_0 at zero solute concentration, $\tilde{E}_{avg} = \frac{E_{avg}}{E_0}$ and $(\tilde{E}\tilde{c})_{avg} = \frac{(E\,c)_{avg}}{E_0 c_{\max}}$. In Equation (2.15), $k_1 = \frac{\alpha \Omega^2 E_0 c_{\max}}{3(1-\nu)RT}$ and $k_2 = \frac{2\Omega^2 E_0 c_{\max}}{9(1-\nu)RT}$ are dimensionless parameters reflecting the stress-diffusion interactions, and $\Delta\tilde{\mu}_0(\tilde{c}) = \frac{\Delta\mu_0(\tilde{c})}{RT}$ is a dimensionless concentration-dependent binding energy. For a specified charging current density J_n at the plate faces $x = \pm w/2$, the required boundary conditions for Equation (2.15) are

$$e^{k_1\left(\frac{(\tilde{E}\tilde{c})_{avg}}{\tilde{E}_{avg}} - \tilde{c}\right)} \left(\frac{1}{1-\tilde{c}} + k_2 \tilde{E}(\tilde{c})\tilde{c} - k_2 \frac{d\tilde{E}(\tilde{c})}{d\tilde{c}} \left(\frac{(\tilde{E}\tilde{c})_{avg}}{\tilde{E}_{avg}} - \tilde{c} \right) \tilde{c} + \tilde{c} \frac{d\Delta\tilde{\mu}_0(\tilde{c})}{d\tilde{c}} \right) \frac{\partial \tilde{c}}{\partial \tilde{x}} = \pm \tilde{J}_n,$$

$$\tilde{x} = \pm 1/2, \quad (2.16)$$

where $\tilde{J}_n = \dfrac{J_n w}{FDc_{\max}}$ is a dimensionless flux, with F being the Faraday constant. By comparison of Equation (2.15) with the classical diffusion equation, one can define the effective diffusivity in the presence of all the aforementioned effects as

$$D_{eff} = De^{k_1\left(\frac{(\tilde{E}\tilde{c})_{avg}}{\tilde{E}_{avg}}-\tilde{c}\right)}\left(\frac{1}{1-\tilde{c}}+k_2\tilde{E}(\tilde{c})\tilde{c}-k_2\frac{d\tilde{E}(\tilde{c})}{d\tilde{c}}\left(\frac{(\tilde{E}\tilde{c})_{avg}}{\tilde{E}_{avg}}-\tilde{c}\right)\tilde{c}+\tilde{c}\frac{d\Delta\tilde{\mu}_0(\tilde{c})}{d\tilde{c}}\right), \tag{2.17}$$

where $\tilde{c}$, and thus D_{eff}, is an implicit function of position *x* through the plate. A special case of Equation (2.17) has been given by Wu [71].

2.1.5. Numerical solution methodology

The continuum model described above involves a highly nonlinear partial differential equation, Equation (2.15), to be solved numerically under the boundary condition of Equation (2.16) with zero initial concentration for Equation (2.15). The governing equation is solved using FEMLAB (COMSOL Multiphysics) via the general PDE mode as

$$\frac{\partial\tilde{c}}{\partial t}+\nabla.\boldsymbol{\Gamma}=0\,, \tag{2.18}$$

with $\boldsymbol{\Gamma}$ defined as

$$\boldsymbol{\Gamma}=-e^{k_1\left(\frac{(\tilde{E}\tilde{c})_{avg}}{\tilde{E}_{avg}}-\tilde{c}\right)}\left(\frac{1}{1-\tilde{c}}+k_2\tilde{E}\tilde{c}-k_2\frac{d\tilde{E}(\tilde{c})}{d\tilde{c}}\left(\frac{(\tilde{E}\tilde{c})_{avg}}{\tilde{E}_{avg}}-\tilde{c}\right)\tilde{c}+\tilde{c}\frac{d\Delta\tilde{\mu}_0(\tilde{c})}{d\tilde{c}}\right)\nabla\tilde{c}\,, \tag{2.19}$$

where coupling integration variables are used to define $\widetilde{E}_{avg}$ and $(\widetilde{E}\widetilde{c})_{avg}$. Symmetry of the problem is invoked to solve the governing equation over half the domain, $0 \geq \widetilde{x} \geq -0.5$, and 480 Lagrangian elements are used to discretize this domain. The Neumann boundary condition is applied at both boundary points with the flux $J_n = J_0(1-\widetilde{c})$ at $\widetilde{x} = -0.5$, designed to match the boundary condition in the molecular simulation (see next section), and zero flux at $\widetilde{x} = 0$, consistent with the symmetry of the problem. Necessary material parameters for the model system of hydrogen charging of Ni are obtained from the atomistic models described in the next section.

2.2. Model validation via comparison with molecular dynamics simulation

To demonstrate role of the various physical phenomena associated with stress and solute concentration included in the continuum model of Equations (2.15, 2.16), a model material of hydrogen (H) solutes in a nickel (Ni) host is considered. H in Ni provides a system where H occupies well-defined sites in the host Ni lattice, the H-induced volume change is large enough to induce large stresses. The diffusion of H in Ni under stress is easily characterized [70].

Molecular statics and dynamics can be used (i) to obtain the material parameters entering the continuum model and (ii) to explicitly model the charging of a Ni plate by an imposed flux of H atoms through the surfaces of the plate. The results can then be compared to the predictions of the continuum model.

2.2.1. Properties of H in Ni

Interatomic embedded-atom-method [88] (EAM) potential developed by Angelo et al. [89] has been used to characterize the interactions between atoms in the system. At equilibrium, H atoms occupy octahedral sites in FCC Ni with a maximum attainable molar concentration $c_{\max} = \frac{4}{N_A a_0^3}$ corresponding to the cubic hydride phase NiH, where N_A and a_0 are Avogadro's number and the Ni cubic cell lattice constant, respectively. The dimensionless concentration $\tilde{c} = c / c_{\max}$ is thus identical to the H/Ni ratio. Table 2.1 shows the numerical values for the partial molar volume Ω, the Young's modulus E_0, and the Poisson ratio [70]. Changes in the mechanical properties of the material as H is added to Ni is neglected as the Young's modulus for the fully-hydrided NiH material is only about 10% larger than that of pure Ni.

Concentration-dependent binding energy of the solution in eV/atom obtained using atomistic simulations can be approximated via $\Delta\mu_0(\tilde{c}) = -0.80\tilde{c} + 0.37\tilde{c}^2$ (which is identical to the two-parameters Margules equation (see Equation (2.7)) with parameters $A_0 = 0.15$, $B_0 = 0.28$ in the same units), by creating a range of $\mathrm{NiH}_{\tilde{c}}$ random solid solution materials and computing the energy per H atom. As shown in Figure 2.2, the energy per H is increasingly negative with increasing $\tilde{c}$, favoring higher H concentrations, for this EAM potential [90].

Diffusion of H in Ni occurs by H motion from one octahedral site to a neighboring site, corresponding to motion along the family of $\{110\}$ directions in the fcc lattice. The activation energy E_b of H diffusion in the [110] direction under an applied

uniaxial stress σ along $[1\bar{1}0]$ has been computed [70], and using the activation energy under zero stress $E_b(0)$ as the reference value, $\Delta E_b(\sigma) = E_b(\sigma) - E_b(0)$ is given in Figure 2.3, showing that a tensile stress decreases ΔE_b while a compressive stress increases it. To conform to the simple continuum model of Equation. (2.12), we fit the results to a bilinear curve to estimate the values of α under compression ($\alpha = \alpha_c = 0.180$) and under tension ($\alpha = \alpha_t = 0.404$). When no stress is present, $\Delta E_b = 0$ and the diffusivity is just *D* and is controlled by the zero-stress activation energy of 0.46 eV. Below, a brief description of molecular dynamics simulations of charging at *T*=800K. The temperature has been chosen to facilitate diffusion within the time constraints of MD, for which *D*= $1.28 \pm 0.06 \times 10^{-9}$ m^2/s [70].

2.2.2. Simulation of H Charging of Ni

The details of the atomistic simulations are beyond the scope of this work, and is given in Ref. [70]. However, in the following, a brief description of the problem simulated via MD is discussed. With the material system identified and characterized, a series of H-charging simulations have been conducted using Molecular Dynamics (MD). The sample is a ½-plate geometry with simulation cell dimensions l_x=6.2 nm, l_y=4.0 nm and l_z=3.6 nm, with the crystal orientation corresponding to $x = [110]$, $y = [1\bar{1}0]$, and $z = [00\bar{1}]$ as shown in Figure 2.1b. To mimic a semi-infinite plate in the lateral directions *y* and *z*, the simulation cell is periodic in these directions. To represent one-half

of the full plate, charging occurs into the $\tilde{x} = -1/2$ surface and a symmetry boundary is used at $\tilde{x} = 0$.

The simulation temperature is fixed at 800 K using a Nosé–Hoover thermostat [91, 92] and the simulation cell sizes in all directions fluctuate during the simulation using a barostat in order to maintain zero external pressure conditions [93, 94]. The flux of H atoms is controlled by inserting H atoms at the desired rate J_0 into the layer of octahedral interstitial sites at $\tilde{x} = -1/2$.

To insert an H atom, one site, among the N=160 possible sites in this layer, is chosen randomly for insertion at time intervals of $(\sqrt{2}N_A J_0 N a_0^{\,2})^{-1}$ and an H atom insertion is attempted. If the chosen site is already occupied by an H atom, the insertion attempt is aborted. As H is inserted during charging, the concentration in the insertion layer increases due to insertion and decreases due to diffusion into the plate. The mean flux achieved in the simulation is then the desired flux multiplied by the probability of a successful insertion $(1-\tilde{c}(\tilde{x} = -1/2))$ where $\tilde{c}(\tilde{x} = -1/2)$ is the surface concentration, or $J_n = J_0(1-\tilde{c})\big|_{\tilde{x}=-1/2}$ (Figure 2.1). Note that the actual influx is always subject to statistical fluctuations on top of the mean behaviors described above. The outcome of the simulation is the actual flux J_n as a function of time as well as the H concentration profile, defined as the average number of H atoms in the lateral cross-section at position x, as a function of time. The simulation results are converted into dimensionless quantities using the scalings identified in the development of the continuum model.

Simulations are done at a number of charging rates, $\widetilde{J}_0 = \dfrac{J_0 w}{FDc_{\max}}$ =1.18, 5.89, 11.79, 117.9. Figure 2.4 shows the actual influx $\tilde{J}_n$ as a function of time for the above-mentioned values of the input flux. On the same figure, the predicted flux according to the approximation $\tilde{J}_n = \tilde{J}_0(1-\tilde{c})\big|_{\tilde{x}=-1/2}$ is shown. Aside from the inevitable statistical fluctuations in the actual influx, Figure 2.4 indicates that the above linear estimate is satisfactory for use in the continuum model.

Table 2.1. Numerical values of the model parameters.

Ω (m^3/mole)	$c_{\max}$ (mole/m^3)	E_0 (GPa)	ν
2.053×10^{-6}	1.51×10^{5}	205	0.31

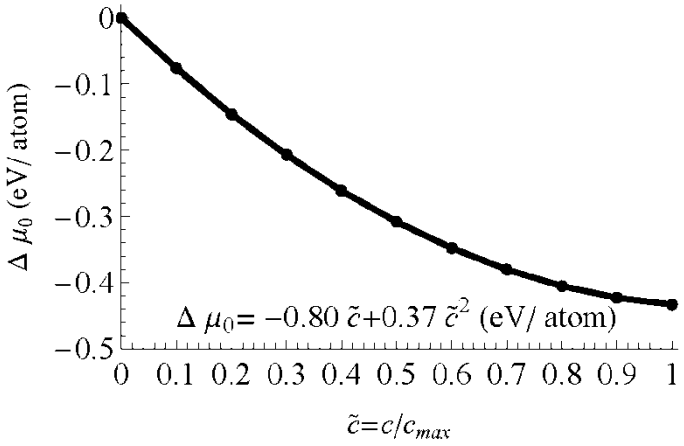

Figure 2.2: Concentration-dependent binding energy $\Delta\mu_0$ as a function of $\tilde{c} = c / c_{\max}$ at 0 K.

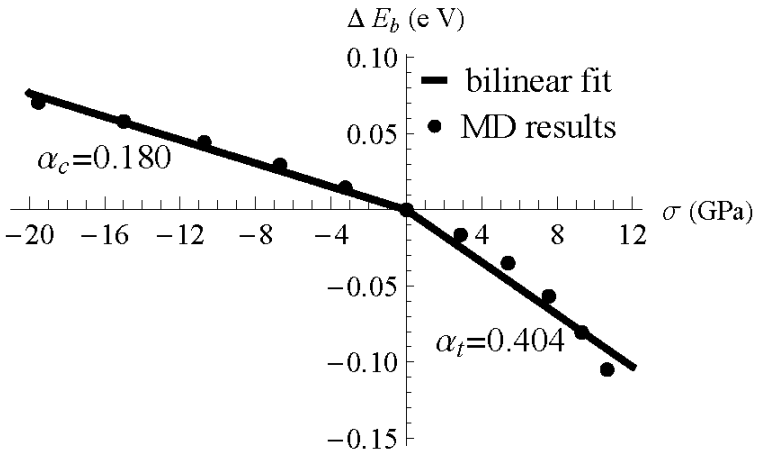

Figure 2.3: Activation energy barrier of diffusion as a function of the normal stress acting perpendicular to the diffusion direction.

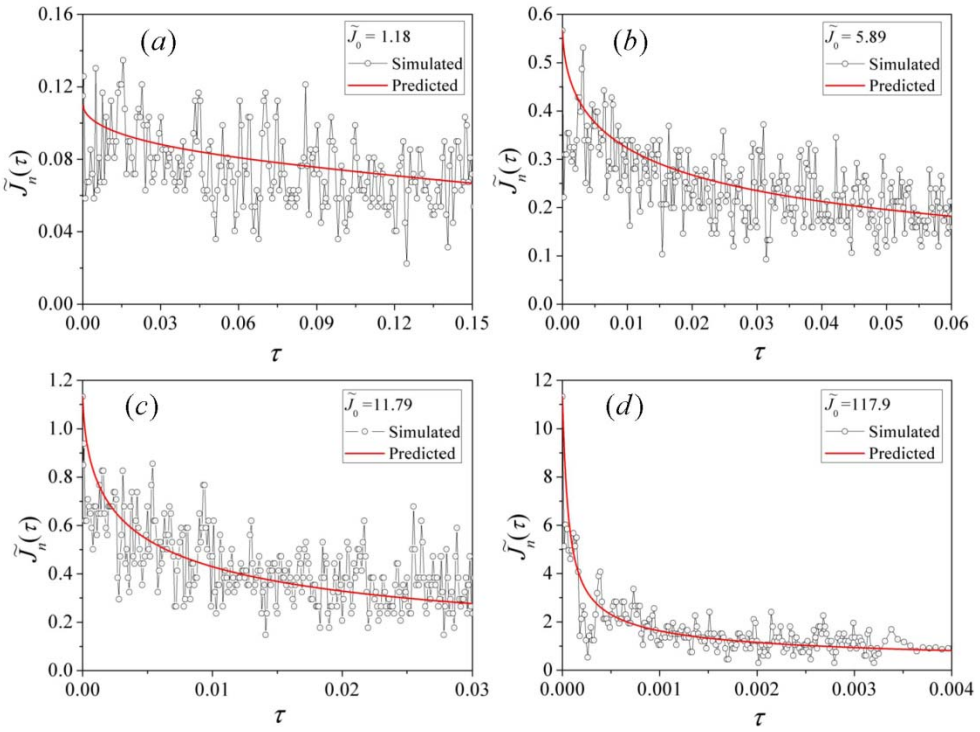

Figure 2. 4: Actual flux data versus the predictive relation as a function of time.

2.3. Results and Analysis

The predictions of the H concentration profile through the plate at various times as obtained from the MD simulations and as predicted by the continuum model are shown in Figure 2.5 for various charging rates $\tilde{J}_0 = \dfrac{J_0 w}{FDc_{\max}}$ =1.18, 5.89, 11.79, 117.9. In this figure, and in the rest of this chapter, the atomic simulation results are shown as discrete points, corresponding to the average H concentration at each lateral octahedral site location x at each time, and the continuum predictions are shown as solid lines. For all charging rates and at all times shown, the continuum predictions are in excellent

agreement with the MD results. This broad result validates the use of the continuum model for describing diffusion with strongly-coupled stress effects.

As H is injected at the surface, the near-surface concentration rises, inducing a compressive stress in this region, which suppresses the H diffusivity in this region but also generates an energetic driving force for diffusion; see Equations (2.12) and (2.5). As the near-surface concentration increases further, with stress continuing to increase, the mean flux $J_n = J_0(1-\tilde{c})\big|_{\tilde{x}=-1/2}$ decreases and the surface concentration reaches a near-steady state value. At low flux levels, the surface concentration remains well below unity and the concentration profile is relatively smooth and convex. At high flux levels, however, the surface concentration approaches unity and the concentration profile is concave and then convex, showing an inflection point. The flow of H into the plate resembles the motion of a diffuse interface.

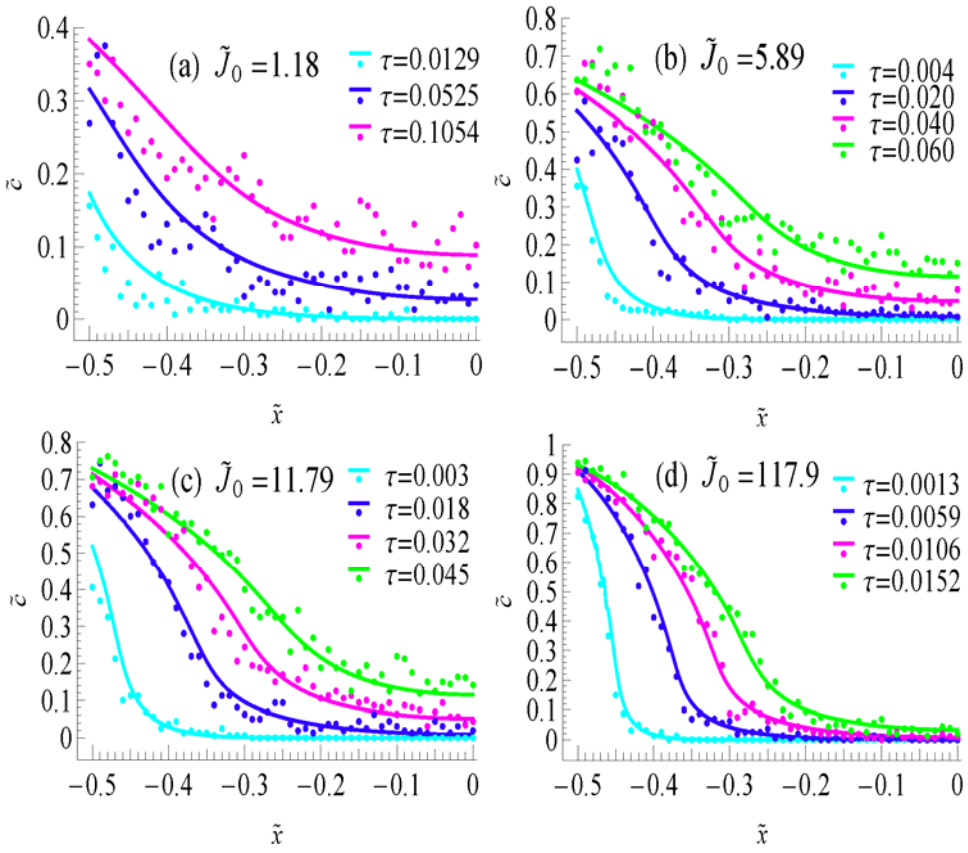

Figure 2.5: Concentration profile across the thickness; dots are MD results and solid lines are the continuum model predictions.

An advantage of the continuum model, discussed in Section 2.1, is that it enables us to study the individual contribution of stress-dependent activation energy, existence of a stoichiometric maximum limit, and the concentration-dependent heat of solution to the overall continuum model. To this end, limiting cases of the full model are considered in which one or more of the described physical effects are removed from the model while the others are preserved. In all subsequent figures, the simulation data remains unchanged from that shown in Figure 2.5, since it is not possible to alter the characteristics of the physical system within the MD simulation.

2.3.1. Stress dependence of the activation energy

To assess the effect of stress-diffusivity coupling, the dependence of activation energy on stress is removed from the continuum model by considering the special case $k_1 = 0$ in Equation (2.15), corresponding to setting the physical parameters $\alpha_c, \alpha_t = 0$. Figure 2.6 shows the numerical results from the continuum model in comparison with the full MD results. In the absence of stress-diffusivity coupling, the diffusion coefficient near the plate surface, which is under compressive stress, is overestimated. Thus, more material is driven into the plate and the concentration profiles are overestimated in the interior regions. Also, as the charging flux increases, the effect of stresses on the energy barrier becomes more significant to the overall charging process.

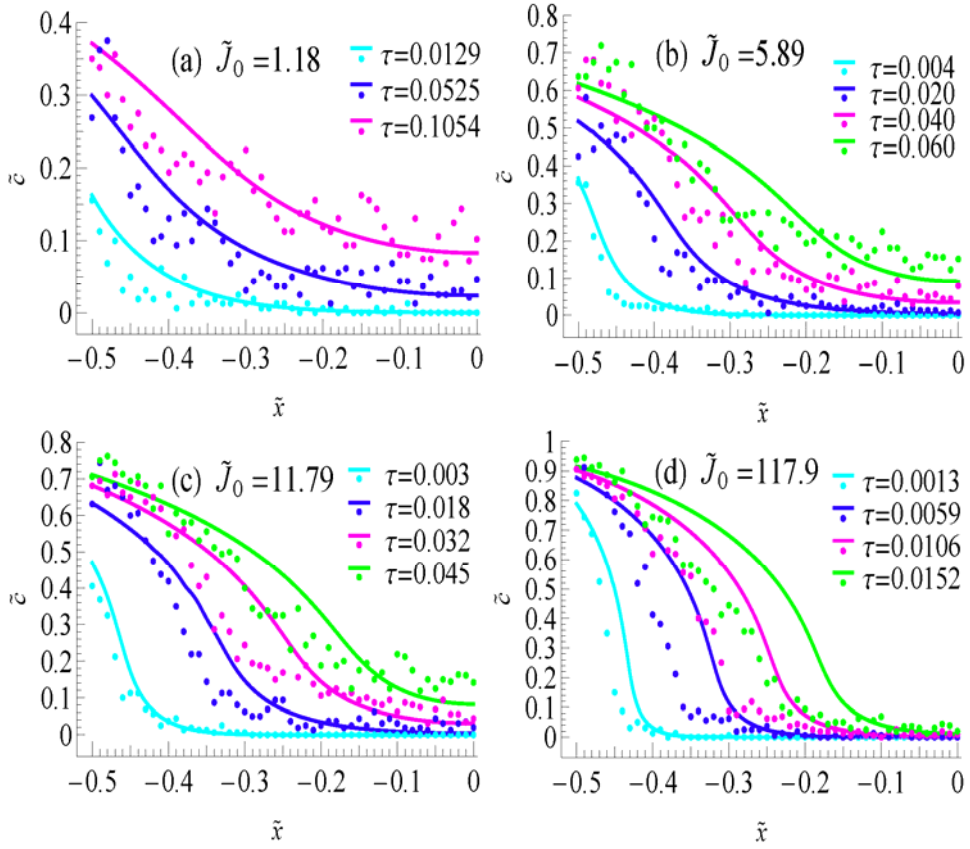

Figure 2.6: Concentration profile across the thickness; atomistic simulation vs. continuum predictions neglecting the stress-diffusivity coupling.

2.3.2. Concentration dependence of the solute binding energy

The role of the concentration-dependence of the binding energy in influencing the diffusion can be examined by setting $\Delta\tilde{\mu}_0(\tilde{c}) = 0$ in Equation (2.15). Numerical results in this limit are shown in Figure 2.7, where the predicted concentration profile is substantially more uniform than the full MD results. This is anticipated because the binding energy function prefers high H concentrations and so creates a driving force on

the H atoms that acts in the opposite direction to the concentration gradient. Hence, when the binding energy is set to zero, the continuum model predicts a smoother concentration profile, as compared to the full problem. Figure 2.7 thus reveals the pivotal role of this binding energy at high solute concentrations.

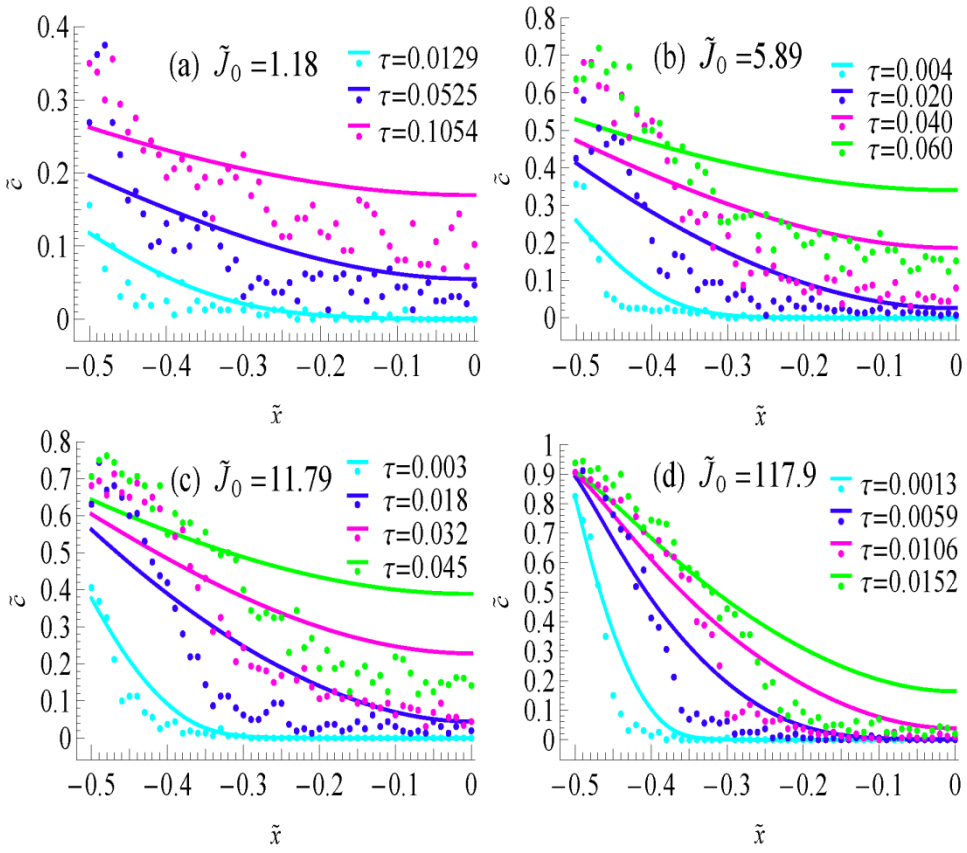

Figure 2.7: Concentration profile across the thickness; atomistic simulation vs. continuum model neglecting the concentration dependence of the binding energy of the solution.

2.3.3. Effect of stoichiometric maximum limit

To examine the contribution of the "saturation cap" imposed by entropic considerations, this effect is removed from the continuum model by taking the dilute concentration limit, in which Equation (2.15) (with $\widetilde{E}(\tilde{c}) = 1$ for the Ni-H system), takes on the form

$$\frac{\partial \tilde{c}}{\partial \tau} = \frac{\partial}{\partial \tilde{x}}\left[e^{k_1(\tilde{c}_{avg} - \tilde{c})} \left(1 + k_2 \tilde{c} + \tilde{c}\Delta\tilde{\mu}_0'(\tilde{c})\right) \frac{\partial \tilde{c}}{\partial \tilde{x}} \right]. \tag{2.20}$$

Equation (2.20) clearly underestimates the effective diffusivity as compared to Equation (2.15). This is particularly influential near the plate surface early in the charging process (not shown in Figure 2.8) which leads to less solute in the system at later times. This results in underestimation of the concentration profiles at later times as shown in Figure 2.8, mainly inside the material and for high fluxes. As well, the profiles obtained according to this model are sharper than those predicted by MD, which is directly related to the underestimation of the effective diffusivity.

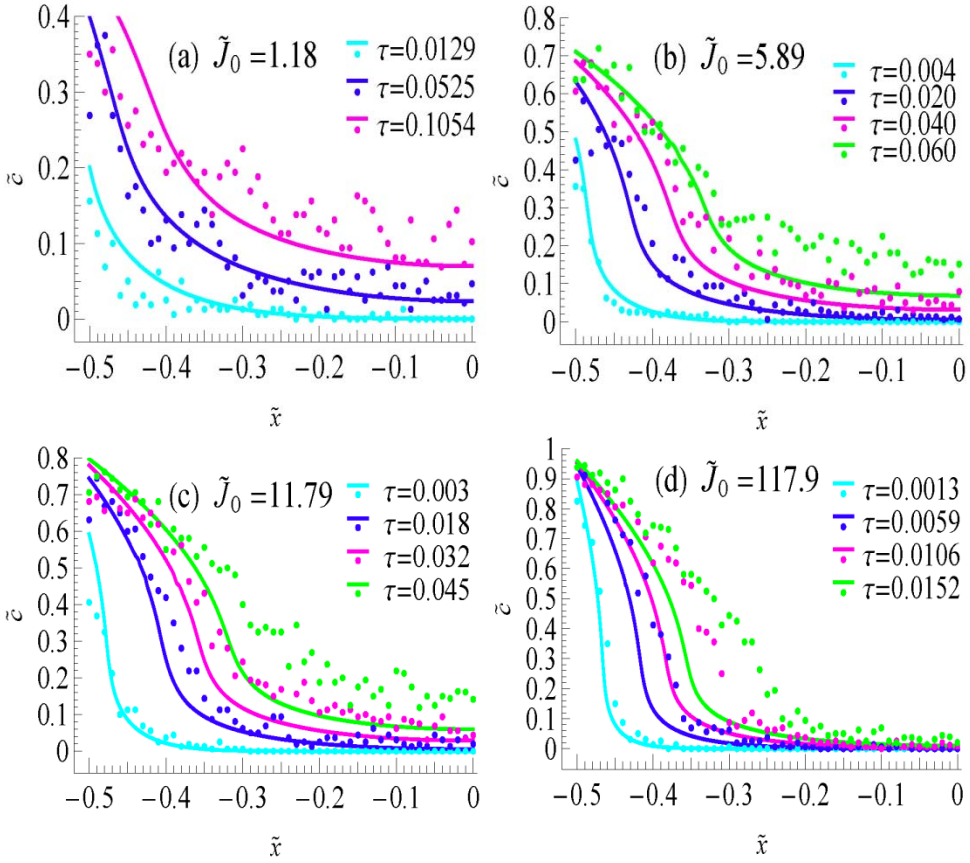

Figure 2.8: Concentration profile across the thickness; atomistic simulation vs. continuum model without the saturation cap, Equation (2.20).

2.3.4. Comparison with the classical diffusion equations

In this section, two versions of the classical diffusion equations are employed to predict the concentration profile, and the results are compared with the MD results. In both models, the effects of stress-activation coupling, hydrostatic stress and concentration-dependent heat of solution are not included, i.e. $k_1 = k_2 = \Delta\tilde{\mu}_0(\tilde{c}) = 0$. In the first model, the saturation cap is not considered, and therefore Equation (2.15) is reduced to

$$\frac{\partial \tilde{c}}{\partial \tau} = \frac{\partial^2 \tilde{c}}{\partial \tilde{x}^2}. \tag{2.21}$$

Concentration profiles as obtained according to this model are given in Figure 2.9, together with the MD results. It should be noted that even though the saturation cap is not considered in this case, the charging flux decreases linearly to zero as the surface concentration tends to the saturation concentration. Hence, the concentration remains below the saturation concentration. A clear feature of the MD results which is not captured by this model is the emergence of the inflection point in the concentration profile. When the saturation cap is imposed in the classical model, the governing Equation (2.15) is reduced to

$$\frac{\partial \tilde{c}}{\partial \tau} = \frac{\partial}{\partial \tilde{x}}\left(\frac{1}{1-\tilde{c}}\frac{\partial \tilde{c}}{\partial \tilde{x}}\right). \tag{2.22}$$

Figure 2.10 compares the concentration profiles predicted by this model and the MD results. Although introduction of the saturation cap in the diffusion equation enables the model to capture the double-curvature behavior of the concentration profile, the figure shows the deviation of this model from the MD results. In particular, near the plate surface, the competition between the combined effect of the stress dependent activation energy and the concentration dependent heat of solution (both of which slow the diffusion) and the effect of the hydrostatic stress (which enhances the diffusion) is missing in this model. Figure 2.10 indicates that in the regime of high charging rate the outcome is evidently an overestimation of the influx and hence the concentration profile.

According to Figures 2.9 and 2.10, one could erroneously conclude that the classical diffusion equations are quantitatively satisfactory except for the highest flux case $\tilde{J}_0 = 117.9$, but this arises here only because of the cancellation of a number of independent competing effects. These effects do not necessarily cancel out in general. Even with significant cancellations in some regimes, Figure 2.9 demonstrates that the classical diffusion equation fails in predicting the concentration profiles within the battery electrode for the high-flux charging regime of most practical importance. For other systems such as Li in Si, the physical effects described in this paper might come into play with different weights compared to H in Ni, highlighting one effect over the others.

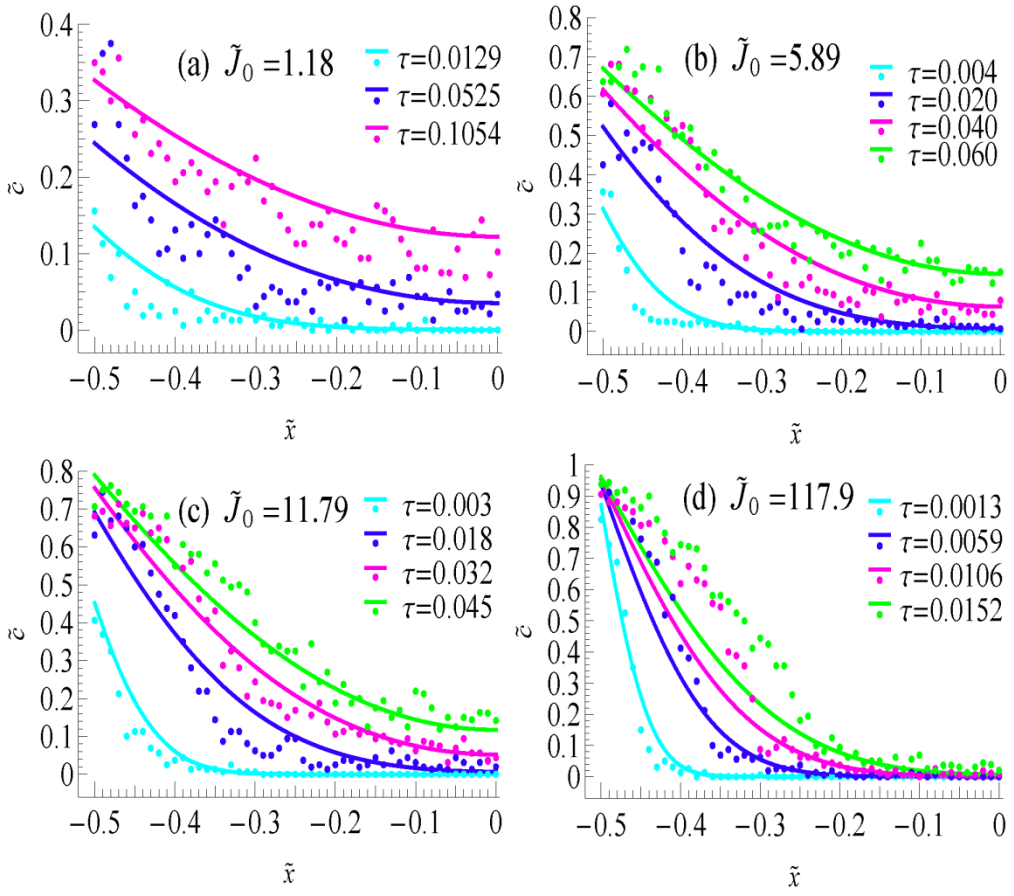

Figure 2.9: Concentration profile across the thickness; atomistic simulation vs. classical model without saturation cap, Equation (2.21).

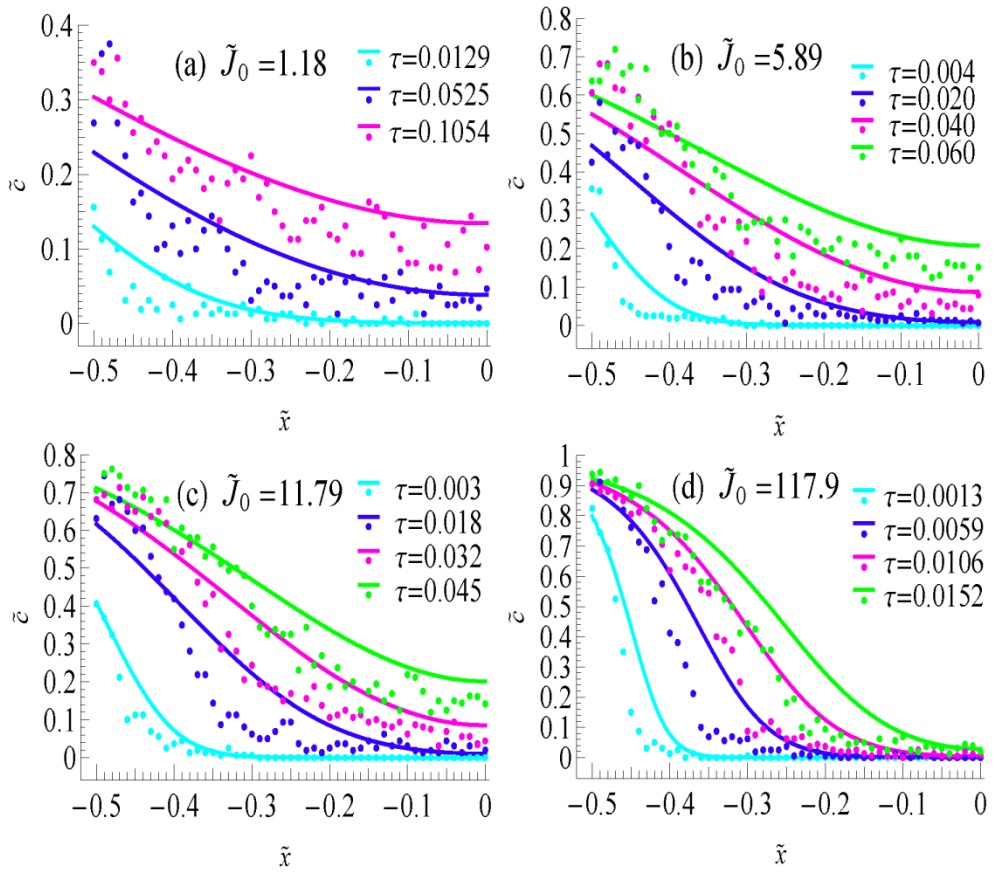

Figure 2.10: Concentration profile, atomistic simulation vs. classical model with saturation cap, Equation (2.22).

2.3.5. *Applicability and limitations for lithium diffusion in silicon*

The present model is considered as an underlying framework for simulation of Li diffusion in Si. In this case, however, some additional complexities are important, including the structural change of the Si lattice resulting in amorphization. This would lead to an additional entropy in the system, emergence of inelastic behavior [16, 95, 96], and a strong influence on the partial molar volume of Li during intercalation/deintercalation [97]. Furthermore, due to the 400% volume change arising

during the cycling of Si, the deformation can easily exceed beyond the realm of small-deformation theory employed in the present model [51]. However, the important nonlinear stress-diffusivity coupling considered here could be further highlighted for the Li/Si system, where huge deformation and large stresses are present [98]. Furthermore, at high concentrations, the effect of solute saturation on the entropy of the system and that of the concentration-dependent binding energy [99-101] should play substantial roles near the stoichiometric limit of the solution. Another feature of the Li/Si system that has been addressed in the present model is the change in the Young's modulus during intercalation. Although negligible for the case of hydrogen in nickel, the Young's moduli of Li-Si phases are greatly reduced relative to Si [82], even without amorphization.

2.4. Summary

A continuum framework has been developed for modeling highly nonlinear behavior associated with atomic-scale diffusion at high solute concentrations and very large stresses. The continuum model introduces a stress-diffusivity coupling through the effect of internal stresses on the activation energy of diffusion. The stoichiometric maximum concentration of the solute is explicitly recognized as the saturation limit by modifying the free energy of the system to account for high solute concentrations. The effect of the concentration-dependent binding energy between the host and solute atoms as a result of change in the chemical environment of the solution is accommodated. Finally, the

mechanical properties of the host solid are also considered as a function of the solute concentration in the model.

The model was then validated for the case of hydrogen diffusion in nickel, and the continuum model predictions proved to be in excellent agreement with atomistic simulations. It was demonstrated that each of the above-mentioned effects, with the exception that change in mechanical properties of the host solid is negligible for the test system of this paper, plays a significant role in the overall predictions of the continuum model, especially at high charging rates. A comparative study between two versions of the classical diffusion equations and MD simulations was also presented. Capabilities and limitations of the continuum model for modeling diffusion of lithium in silicon anodes were discussed.

Chapter 3

A surface locking instability for atomic intercalation into a solid

Experiments on thin films and nanowire electrode are suggesting that there exist some critical values for particle size and charging current, below which nearly complete charging capacity is attainable [13, 28, 102, 103]. In order to facilitate our understanding of the size- and rate-effects in battery systems, a fundamental step is to understand how mechanical stresses might affect atomic diffusion into solids. Diffusion-induced stresses (DIS) in solids have long been modeled by analogy with thermal stresses in a variety of systems and geometries [42, 44, 49, 66, 104]. However, with the exception of a few theoretical studies dealing with crack growth or nucleation [53-57], most of the existing studies do not usually indicate any terminal size or charging rate beyond which complete charging/discharging becomes impossible in the absence of fracture. Here, we note that the classical theories of diffusion-induced stresses are formulated for systems with relatively small stresses while the silicon anodes typically experience very large deformation and stresses. Among many possible effects associated with large stresses, special attention is focused on the coupling between internal stresses and activation energy for diffusion. In this chapter, we will show that a critical phenomenon of

spontaneous surface locking arises under galvanostatic charging conditions as soon as the stress-activation coupling is considered. In this phenomenon, a smooth charging process is abruptly replaced by spontaneous locking of diffusion near the surface of electrode once the product between charging current and electrode size exceeds a critical value. The same phenomenon persists for electrodes with planar, cylindrical and spherical geometries [87].

3.1. Surface locking instability for a free-standing plate

Consider a free-standing, infinitely extended plate of thickness *w* subject to a constant uniform charging current density i_n on both of its side faces, as shown in Figure 3.1a. The diffusion process can be described by the one-dimensional diffusion equation along the *x*-axis as

$$\frac{\partial c}{\partial t} = \frac{\partial}{\partial x}\{D\frac{\partial c}{\partial x}\} \tag{3.1}$$

where *c* is the solute concentration and D is the diffusivity, which is treated as a constant in most existing studies on DIS [42, 44, 49, 66, 104]. On the other hand, atomistic simulations have revealed that internal stresses can strongly influence the activation energy for diffusion [84]. For instance, diffusivity of hydrogen in nickel at room temperature can be doubled when the normal stress acting perpendicular to the diffusion direction reaches about 2 GPa [70]. Normally, a tensile stress decreases the energy barrier while a compressive stress raises it. The reason is that diffusion of a solute particle in a host material takes place as a sequence of jumps between adjacent interstitial sites.

The probability for each jump could be significantly enhanced (suppressed) by a tensile (compressive) stress. Denoting the change in energy barrier due to the internal stresses by ΔE_b, the diffusivity D can be expressed as $D = D_0 \exp(-\Delta E_b / RT)$, where D_0 is the diffusivity in the absence of internal stress, R is the gas constant and T is absolute temperature. For atomic diffusion into a plate, we assume a linear dependence $\Delta E_b = -\alpha \Omega \sigma_b$, where α is a positive dimensionless constant, Ω is the partial molar volume of the solute and σ_b is the biaxial stress in the plate. The stress-dependent diffusivity can thus be written as [85-87]

$$D = D_0 \exp\left(\frac{\alpha \Omega \sigma_b}{RT}\right). \tag{3.2}$$

Assuming the plate is made of a homogeneous isotropic elastic solid, and treating the elastic deformation as a quasi-static process following the classical analogy between DIS and thermal stresses [66], the biaxial stress in the plate is

$$\sigma_b(x) = \frac{\Omega E}{3(1-\nu)}\left[c_{avg} - c(x)\right], \tag{3.3}$$

where E and ν are Young's modulus and Poisson's ratio of the plate, respectively, and $c_{avg} = \left(\int_{-w/2}^{w/2} c\,dx\right)/w$ is the average solute concentration in the plate. The diffusion equation becomes

$$\frac{\partial c}{\partial t} = \frac{\partial}{\partial x}\left\{D_0 \exp\left[\frac{\alpha \Omega E}{3(1-\nu)RT}(c_{avg} - c)\right]\frac{\partial c}{\partial x}\right\} \tag{3.4}$$

with boundary conditions

$$D_0 \exp\left[\frac{\alpha \Omega E}{3(1-\nu)RT}(c_{avg}-c)\right]\frac{\partial c}{\partial x} = \pm\frac{i_n}{F}, \qquad x = \pm w/2 \tag{3.5}$$

where F is Faraday's constant. If the initial solute concentration is zero and charging starts at $t = 0$, mass conservation indicates $c_{avg} = 2i_n t / F w$. We recast the governing equation in a non-dimensional form

$$\frac{\partial \tilde{c}}{\partial \tau} = \frac{\partial}{\partial \tilde{x}}\left\{\exp[\mu(2\tilde{i}_n\tau - \tilde{c})]\frac{\partial \tilde{c}}{\partial \tilde{x}}\right\} \tag{3.6}$$

with

$$\exp[\mu(2\tilde{i}_n\tau - \tilde{c})]\frac{\partial \tilde{c}}{\partial \tilde{x}} = \pm\tilde{i}_n, \qquad \tilde{x} = \pm 1/2 \tag{3.7}$$

where $\tilde{c} = \Omega c$, $\tau = \frac{D_0 t}{w^2}$, $\tilde{x} = \frac{x}{w}$, $\mu = \frac{\alpha\Omega E}{3(1-\nu)RT}$, and $\tilde{i}_n = \frac{i_n \Omega w}{F D_0}$. The steady-state solution to this equation takes the form

$$\tilde{c}^{st} = 2\tilde{i}_n\tau + f(\tilde{x}) \tag{3.8}$$

where $f(\tilde{x})$ satisfies

$$\exp[-\mu f(\tilde{x})]\frac{df(\tilde{x})}{d\tilde{x}} = 2\tilde{i}_n\tilde{x}, \text{ or } f(\tilde{x}) = -\frac{1}{\mu}\log[\mu\tilde{i}_n(A-\tilde{x}^2)]. \tag{3.9}$$

Here, A is an integration constant to be determined from mass conservation $\tilde{c}_{avg}^{st} = 2\tilde{i}_n\tau$, which relates A to $\mu\tilde{i}_n$ as

$$\int_{-1/2}^{1/2}\log[A-\tilde{x}^2]d\tilde{x} + \log[\mu\tilde{i}_n] = 0. \tag{3.10}$$

However, a careful inspection of the steady-state solution

$\tilde{c}^{st} = 2\tilde{i}_n\tau - \frac{1}{\mu}\log[\mu\tilde{i}_n(A-\tilde{x}^2)]$ indicates that it diverges at the top and bottom surfaces

$\tilde{x} = \pm 1/2$ in the critical case of $A = 1/4$. Setting $A = 1/4$, Equation (3.10) can be solved for the critical value of $\mu\tilde{i}_n$ as

$$(\mu\tilde{i}_n)_{cr} = \frac{\alpha\Omega^2 i_n w E}{3(1-\nu)RTFD_0} = e^2. \tag{3.11}$$

This critical value corresponds to a surface locking instability induced by the biaxial stress in the plate. Atomic diffusion into the plate causes compressive stress near the surface and tensile stress near the center of the electrode. The stress-activation coupling described in Equation (3.2) suggests that diffusion is slowed down near the surface by the compressive stress there. Under galvanostatic charging conditions, a slower diffusivity near the surface leads to accumulation of solute near the surface and even higher compressive stress, hence a runaway instability resulting in "surface locking". Equation (3.11) shows that surface locking occurs as soon as $\mu\tilde{i}_n$ exceeds $e^2 \approx 7.39$. To visualize the transient process that leads to surface locking, a finite element scheme (FEM) is employed to solve the governing equation numerically. Due to the symmetry of the problem, the nonlinear diffusion equation is solved for $1/2 \geq \tilde{x} \geq 0$ using 500 quadratic Lagrange elements. Figure 3.1b shows the evolution of solute concentration in the subcritical case of $\mu\tilde{i}_n = 7.2$, whereas Figure 3.1c shows the behavior in the supercritical case of $\mu\tilde{i}_n = 7.7$. One readily sees that the smooth charging process in the subcritical regime is replaced with surface locking in the supercritical regime. Figure 3.1d shows

the concentration gradient at the plate surface as a function of time for various values of $\mu\tilde{i}_n$. The surface locking occurs above a critical value in the range $7.7 \geq (\mu\tilde{i}_n)_{cr} > 7.2$, in perfect agreement with the analytical solution.

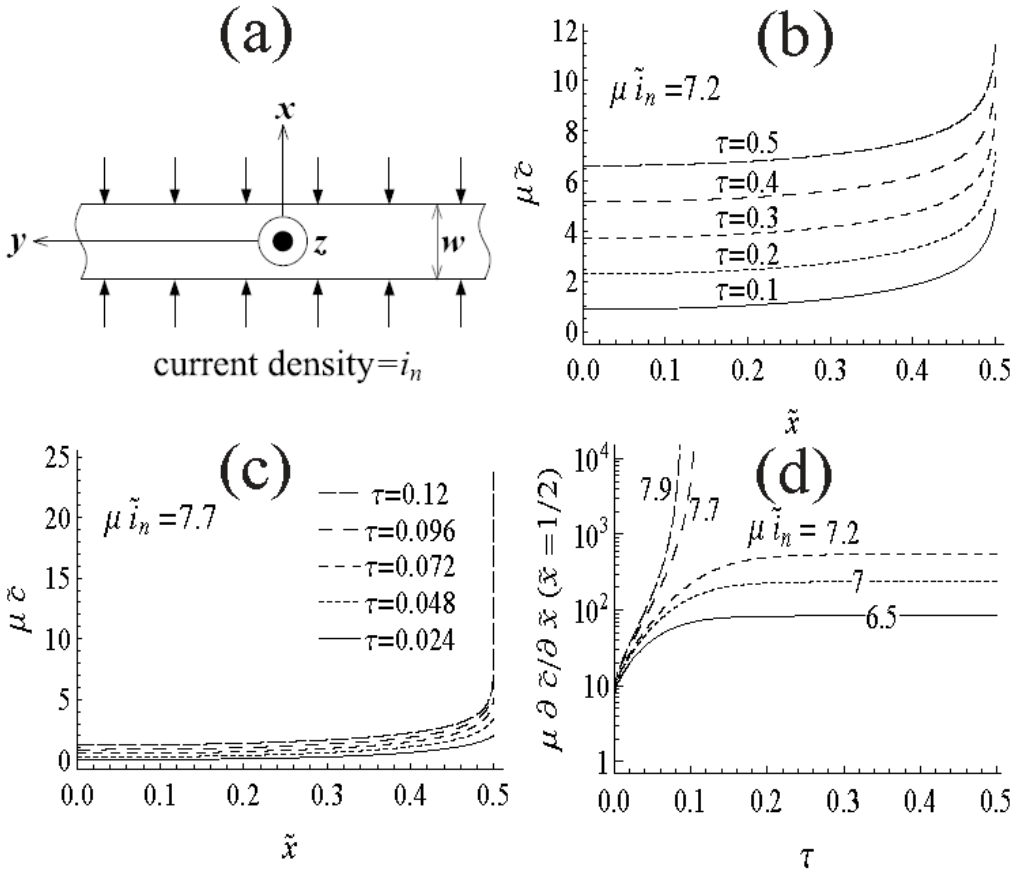

Figure 3.1: Surface locking in a planar electrode under galvanostatic charging. (a) A plate electrode is subject to a uniform current density on its faces. (b) Evolution of the solute concentration profile in the subcritical case of $\mu\tilde{i}_n = 7.2$. (c) Evolution of the solute concentration profile in the supercritical regime of $\mu\tilde{i}_n = 7.7$. (d) Evolution of the surface gradient of solute concentration for various values of $\mu\tilde{i}_n$. The results indicate that surface locking occurs above a critical value between $7.7 \geq (\mu\tilde{i}_n)_{cr} > 7.2$, in agreement with the analytical solution which predicts $(\mu\tilde{i}_n)_{cr} = e^2 \approx 7.39$.

3.2. Surface locking instability for a cylindrical wire

In this section, we will consider an infinitely long cylindrical wire with circular cross-section of radius r_0, with zero net axial force, subject to a constant uniform charging current density i_n on its surface (see Figure 3.2a). Using the symmetry of the problem, the diffusion equation can be reduced to the following radial diffusion equation

$$\frac{\partial c}{\partial t} = \frac{1}{r}\frac{\partial}{\partial r}\{r D \frac{\partial c}{\partial r}\}, \tag{3.12}$$

subject to the boundary condition

$$D\frac{\partial c}{\partial r} = \frac{i_n}{F} \qquad \text{at} \qquad r = r_0 \tag{3.13}$$

In this case, the radial diffusivity D is considered as a function of stress according to Equation (3.2), except that the biaxial stress σ_b is replaced by the average of circumferential and axial stresses in the wire,

$$D = D_0 \exp[\frac{\alpha\Omega}{RT}(\frac{\sigma_{\theta\theta} + \sigma_{zz}}{2})], \tag{3.14}$$

where [50]

$$\sigma_{\theta\theta} = \frac{\Omega E}{6(1-\nu)}[c_{avg}(r_0) + c_{avg}(r) - 2c], \tag{3.15}$$

$$\sigma_{zz} = \frac{\Omega E}{3(1-\nu)}[c_{avg}(r_0) - c], \tag{3.16}$$

and

$$c_{avg}(r) = \frac{2}{r^2}\int_0^r \rho c(\rho) d\rho \,. \tag{3.17}$$

Given the stress field, the concentration-dependent diffusivity coefficient, given by Equation (3.14), can be introduced into the radial diffusion Equation (3.12). Assuming that the solute concentration is zero in the beginning of the charging process, it can be shown that $c_{avg}(r_0) = 2i_n t / Fr_0$, and Equation (3.12) can be casted into the following dimensionless form

$$\frac{\partial \tilde{c}}{\partial \tau} = \frac{1}{\tilde{r}}\frac{\partial}{\partial \tilde{r}}\{\tilde{r}\exp[\frac{\mu}{4}(6\tilde{i}_n\tau + \tilde{c}_{avg}(\tilde{r}) - 4\tilde{c})]\frac{\partial \tilde{c}}{\partial \tilde{r}}\}, \tag{3.18}$$

with the boundary condition

$$\exp[\mu(2\tilde{i}_n\tau - \tilde{c})]\frac{\partial \tilde{c}}{\partial \tilde{r}} = \tilde{i}_n, \qquad \text{at} \quad \tilde{r} = 1, \tag{3.19}$$

where $\tau = \frac{D_0 t}{r_0^{\,2}}$, $\tilde{r} = \frac{r}{r_0}$, $\mu = \frac{\alpha\Omega E}{3(1-\nu)RT}$, $\tilde{c}_{avg}(\tilde{r}) = \Omega c_{avg}(r_0\tilde{r})$, and $\tilde{i}_n = \frac{i_n \Omega r_0}{FD_0}$.

Analogous to the analysis presented before, we will assume that there exists a steady state solution for Equation (3.18) in the form of

$$\tilde{c}^{st} = 2\tilde{i}_n\tau + f(\tilde{r}) \,. \tag{3.20}$$

Upon substitution of Equation (3.20) into Equation (3.18), the following ordinary differential equation is obtained,

$$2\tilde{i}_n = \frac{1}{\tilde{r}}\frac{d}{d\tilde{r}}\{\tilde{r}\exp[\frac{\mu}{4}(f_{avg}(\tilde{r}) - 4f)]\frac{df}{\partial \tilde{r}}\}, \tag{3.21}$$

where $f_{avg}(\tilde{r}) = \frac{2}{\tilde{r}^2}\int_0^{\tilde{r}} \rho\, f(\rho) d\rho$. Note that with $\tilde{c}^{st}$ as given in Equation (3.20), one can easily verify that $f_{avg}(1) = 0$. Equation (3.21) can be integrated with respect to $\tilde{r}$, and using the finiteness condition at $\tilde{r} = 0$, it can be reduced to

$$\tilde{i}_n \tilde{r} = \exp[\frac{\mu}{4}(f_{avg}(\tilde{r}) - 4f)]\frac{df}{\partial \tilde{r}}. \tag{3.22}$$

Here, note that Equation (3.22), written for $\tilde{r} = 1$, with $f_{avg}(1) = 0$, implies that $\tilde{c}^{st} = 2\tilde{i}_n \tau + f(\tilde{r})$ satisfies the boundary condition (3.19).

We are not aware of a technique which could be employed to obtain an analytical solution for Equation (3.22). However, following the analysis presented in the Appendix, one can show that

$$\frac{dp}{d\tilde{r}}(\tilde{r} = 1) > \frac{df}{\partial \tilde{r}}(\tilde{r} = 1) > \frac{dq}{d\tilde{r}}(\tilde{r} = 1), \tag{3.23}$$

where $p(\tilde{r})$ and $q(\tilde{r})$ satisfy

$$\tilde{i}_n \tilde{r} = \exp[\frac{\mu}{4}(p(0) - 4p)]\frac{dp}{\partial \tilde{r}}, \qquad p_{avg}(1) = 0, \tag{3.24}$$

$$\tilde{i}_n \tilde{r} = \exp[-\mu q]\frac{dq}{\partial \tilde{r}}, \qquad q_{avg}(1) = 0. \tag{3.25}$$

Equations (3.24,3.25) can now be solved analytically. Straightforward analysis shows that $\frac{dp}{d\tilde{r}}(\tilde{r} = 1)$ tends to infinity for $\mu \tilde{i}_n > 2e^{3/4}$, and $\frac{dq}{d\tilde{r}}(\tilde{r} = 1)$ tends to infinity for

$\mu \tilde{i}_n > 2e$. Therefore, according to the inequality (3.23), $\frac{df}{d\tilde{r}}(\tilde{r} = 1)$ has a finite value for $\mu \tilde{i}_n < 2e^{3/4}$, but tends to infinity for $\mu \tilde{i}_n > 2e$. Therefore, the critical value for $\mu \tilde{i}_n$ falls somewhere between $2e^{3/4}$ and $2e$.

In order to verify the analytical results obtained above, we have employed a FEM scheme to solve Equations (3.18, 3.19). FEM results obtained with 1000 quadratic Lagrange elements are shown in Figure 3.2. In this figure, $\tau = D_0 t / r_0^2$ and $\tilde{r} = r / r_0$. Figure 3.2b shows the concentration profile in the cylinder in the subcritical case of $\mu \tilde{i}_n = 4.4$, whereas Figure 3.2c shows the behavior in the supercritical case of $\mu \tilde{i}_n = 5.2$. Figure 3.2d illustrates the evolution of the concentration gradient at the surface of the cylinder for various values of $\mu \tilde{i}_n$. Surface locking is seen to occur above a critical value somewhere between $5.2 \geq (\mu \tilde{i}_n)_{cr} > 4.4$, in agreement with the analytical solution.

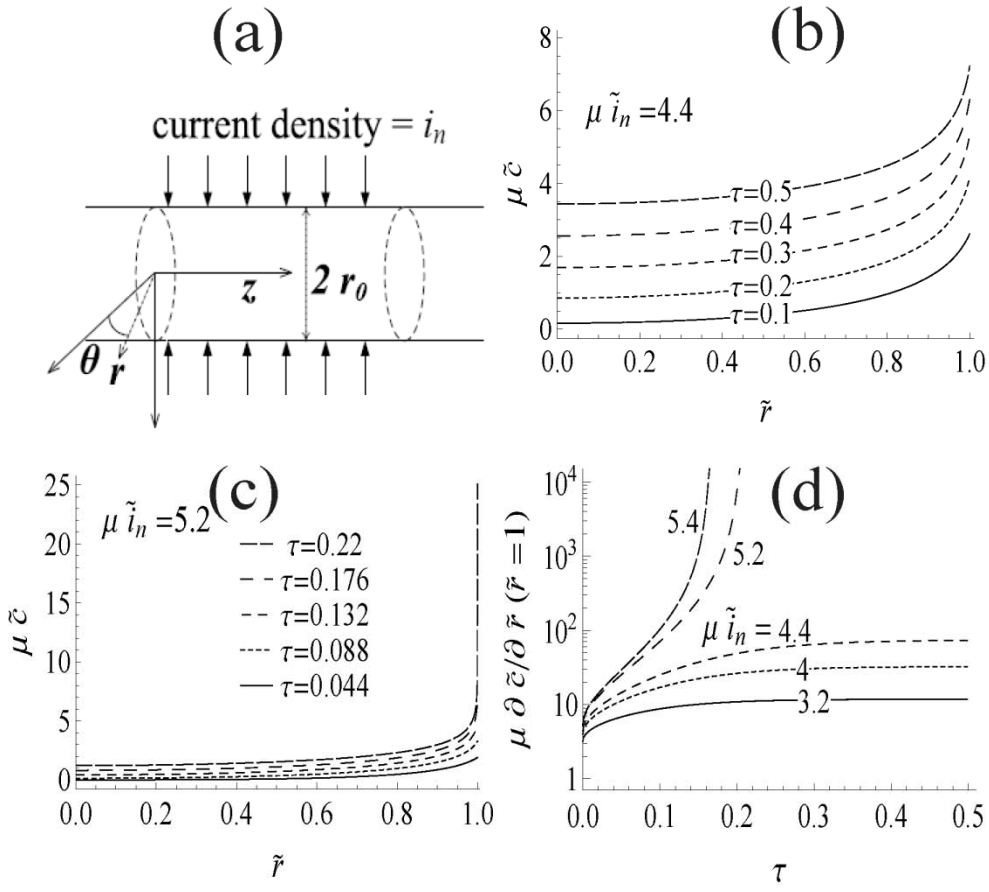

Figure 3.2: Surface locking in a cylindrical electrode under galvanostatic charging. (a) A cylindrical wire is subject to a uniform current density on its surface. (b) Evolution of the solute concentration profile in the subcritical case of $\mu\tilde{i}_n = 4.4$. (c) Evolution of the solute concentration profile in the supercritical regime of $\mu\tilde{i}_n = 5.2$. (d) Evolution of the surface gradient of solute concentration for various values of $\mu\tilde{i}_n$. The results indicate that surface locking occurs above a critical value between $5.2 \geq (\mu\tilde{i}_n)_{cr} > 4.4$, in agreement with the theoretical analysis.

3.3. Surface locking instability for a spherical particle

In this section, we will consider galvanostatic charging of a spherical particle with radius r_0 subject to galvanostatic charging with uniform current density i_n on its surface,

Figure 3.3a. As a result of spherical symmetry, the governing equation collapses to the radial diffusion equation

$$\frac{\partial c}{\partial t} = \frac{1}{r^2}\frac{\partial}{\partial r}\{r^2 D\frac{\partial c}{\partial r}\}, \tag{3.26}$$

subject to the boundary condition

$$D\frac{\partial c}{\partial r} = \frac{i_n}{F} \qquad \text{at} \qquad r = r_0 \tag{3.27}$$

Here, we will take the diffusivity D to depend on the hoop stress $\sigma_{\theta\theta} = \sigma_{\varphi\varphi}$ according to

$$D = D_0 \exp[\frac{\alpha\Omega}{2RT}(\sigma_{\theta\theta} + \sigma_{\varphi\varphi})], \tag{3.28}$$

where the stress components are given by [44]

$$\sigma_{\theta\theta} = \sigma_{\varphi\varphi} = \frac{\Omega E}{9(1-\nu)}[2c_{avg}(r_0) + c_{avg}(r) - 3c], \tag{3.29}$$

with

$$c_{avg}(r) = \frac{3}{r^3}\int_0^r \rho^2 c(\rho) d\rho. \tag{3.30}$$

Using the mass balance condition, it can be shown that $c_{avg}(r_0) = 3i_n t / Fr_0$, and Equations (3.28, 3.29), the diffusion Equation (3.26) can be written in the following form

$$\frac{\partial \tilde{c}}{\partial \tau} = \frac{1}{\tilde{r}^2}\frac{\partial}{\partial \tilde{r}}\{\tilde{r}^2 \exp[\frac{\mu}{3}(6\tilde{i}_n\tau + \tilde{c}_{avg}(\tilde{r}) - 3\tilde{c})]\frac{\partial \tilde{c}}{\partial \tilde{r}}\}, \tag{3.31}$$

subject to the boundary condition

$$\exp[\mu(3\tilde{i}_n\tau - \tilde{c})]\frac{\partial \tilde{c}}{\partial \tilde{r}} = \tilde{i}_n, \qquad \text{at} \quad \tilde{r} = 1, \tag{3.32}$$

where $\tau = \frac{D_0 t}{r_0^{\,2}}$, $\tilde{r} = \frac{r}{r_0}$, $\tilde{c}_{avg}(\tilde{r}) = \Omega c_{avg}(r_0 \tilde{r})$, $\mu = \frac{\alpha \Omega E}{3(1-\nu) R T}$ and $\tilde{i}_n = \frac{i_n \Omega r_0}{F D_0}$.

Steady-state solution for Equations (3.32, 3.33), if existent, should have the form $\tilde{c}^{st} = 3\tilde{i}_n \tau + f(\tilde{r})$, which upon substitution into Equation (3.31) yields

$$3\tilde{i}_n = \frac{1}{\tilde{r}^2}\frac{d}{d\tilde{r}}\{\tilde{r}^2 \exp[\frac{\mu}{3}(f_{avg}(\tilde{r}) - 3f)]\frac{df}{d\tilde{r}}\}, \tag{3.33}$$

where $f_{avg}(\tilde{r}) = \frac{3}{\tilde{r}^3}\int_0^{\tilde{r}} \rho^2 f(\rho) d\rho$. One can easily show that $f_{avg}(1) = 0$. Equation (3.33) can be integrated to yield

$$\tilde{i}_n \tilde{r} = \exp[\frac{\mu}{3}(f_{avg}(\tilde{r}) - 3f)]\frac{df}{d\tilde{r}}. \tag{3.34}$$

Here, note that Equation (3.34), written for $\tilde{r} = 1$, with $f_{avg}(1) = 0$, implies that $\tilde{c}^{st} = 3\tilde{i}_n \tau + f(\tilde{r})$ also satisfies the boundary condition (3.32).

Similar to the analysis presented in the preceding section, instead of solving Equation (3.34), which is not a trivial task, we will consider the following two ordinary differential equations

$$\tilde{i}_n \tilde{r} = \exp[\frac{\mu}{3}(p(0) - 3p)]\frac{dp}{\partial \tilde{r}}, \qquad p_{avg}(1) = 0, \tag{3.35}$$

$$\tilde{i}_n \tilde{r} = \exp[-\mu q]\frac{dq}{d\tilde{r}}, \qquad q_{avg}(1) = 0. \tag{3.36}$$

It is straightforward to show that $\frac{dp}{d\tilde{r}}(\tilde{r} = 1)$ blows up for $\mu \tilde{i}_n > e^{16/9}/\sqrt[3]{2}$ and $\frac{dq}{d\tilde{r}}(\tilde{r} = 1)$ blows up for $\mu \tilde{i}_n > e^{8/3}/2$. Following an analogous analysis as in the Appendix, it can be shown that

$$\frac{dp}{d\tilde{r}}(\tilde{r}=1) > \frac{df}{\partial\tilde{r}}(\tilde{r}=1) > \frac{dq}{d\tilde{r}}(\tilde{r}=1), \tag{3.37}$$

and therefore, there exists a critical value for $\mu\tilde{i}_n$, in the range

$$e^{8/3}/2 > (\mu\tilde{i}_n)_{cr} > e^{16/9}/\sqrt[3]{2}\ , \tag{3.38}$$

beyond which the steady state solution for Equation (3.31) does not exist.

We have also performed FEM calculations to solve the governing equations and the results are given in Figure 3.3. Figure 3.3b plots the FEM results in the subcritical case of $\mu\tilde{i}_n = 5.1$ and Figure 3.3c shows the behavior in the supercritical case of $\mu\tilde{i}_n = 6.9$. Figure 3.3d plots the concentration gradient at the surface of the sphere as a function of time. Surface locking occurs above a critical value in the range $6.9 \geq (\mu\tilde{i}_n)_{cr} > 5.1$, in agreement with the steady-state analysis.

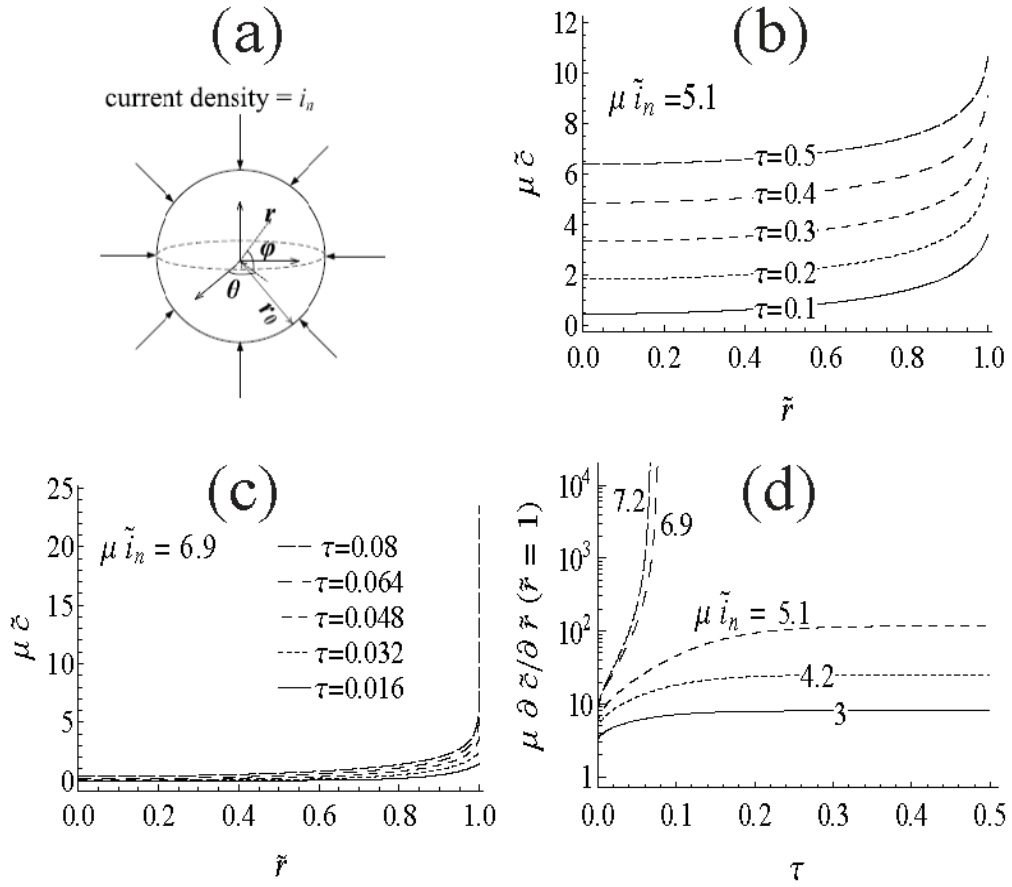

Figure 3.3: Surface locking in a spherical electrode under galvanostatic charging. (a) A sphere is subject to a uniform current density on its surface. (b) Evolution of the solute concentration profile in the subcritical case of $\mu\tilde{i}_n = 5.1$. (c) Evolution of the solute concentration profile in the supercritical regime of $\mu\tilde{i}_n = 6.9$. (d) Evolution of the surface gradient of solute concentration for various values of $\mu\tilde{i}_n$. The results indicate that surface locking occurs above a critical value between $6.9 \geq \mu\tilde{i}_n > 5.1$, in agreement with the theoretical analysis.

3. 4. Discussion

Our further investigation, through numerical analysis, indicates that the surface locking instability presented here always happens for a thin film on an infinitely thick

substrate, even for extremely small charging fluxes, suggesting a zero critical value for $(\mu \tilde{i}_n)_{cr}$ in such case. Further analysis shows that the surface locking phenomenon is not qualitatively affected by including the effect of hydrostatic stress in the chemical potential of the solute [67], albeit the critical value of $(\mu \tilde{i}_n)_{cr}$ can be significantly increased, making the diffusion more difficult to lock up. Since much experiments and theoretical studies are needed to verify if these non-classical solutions to diffusion equation are physically relevant, we leave more detailed investigations to future work.

Finally, we caution a number of potential pitfalls for the surface locking instability discussed here. First, we have not imposed the maximum stochiometric concentration limit for the solute. As the surface concentration approaches this limit, it will become increasingly difficult to maintain a constant charging current, and the boundary condition in our analysis will need to be modified. Also, a number of other effects, including the enthalpic contributions to the chemical potential, elastic anisotropy, changes in elastic modulus and large deformation characteristics at large solute concentrations could play important roles. Nevertheless, the present work demonstrates possible emergence of a host of phenomena that were not in the conventional theory of diffusion-induced stresses but could be critically important for the Lithium ion battery technology.

Chapter 4

A critical size for Si thin film patterned electrodes, and interpretation of stress measurements

Silicon thin film electrodes are among one of the simplest structures subject to broad experimental and theoretical investigations for application in Li-ion batteries [13, 14, 105]. At the same time, degradation and capacity loss in such structures is a common observation, not even limited to Si [106-111] (see Ref. [1] for a comprehensive review). A significant part of the capacity loss, in general in Si electrodes, and in particular, in Si thin film electrodes, has been attributed to a variety of mechanical failure modes. Among various failure modes, through-the-thickness cracks are commonplace in most of the thin film electrodes subject to electrochemical cycling. Such cracks, even if stable during cycling, could cause partial capacity loss, by providing new surfaces which upon later electrochemical operation are subject to passivation, and transform to solid-electrolyte-interphase.

The main approach taken in order to circumvent fracture in thin film electrodes is to decrease the particle size and the film thickness below the critical fracture size. Along this line of thought, Graetz et al. [13] suggested the following critical size,

$$a_c = \frac{2}{\pi}\frac{K_{1c}^2}{\sigma_y^2}, \tag{4.1}$$

where K_{Ic} is the fracture toughness, and σ_y is the yield stress of the polycrystalline Si. Using $K_{Ic} = 0.751$ MPa/m$^{1/2}$ [112], and $\sigma_y = 1$ GPa [113], the critical size a_c turns out to be about 300 nm . This result suggests that once size of the polycrystalline thin film reduces to less than a_c, according to the Griffith criterion [114], brittle fracture becomes impossible, and plastic deformation of the overall polycrystalline thin film becomes dominant. Zhao et al. [24] applied the Griffith criterion to estimate the critical film thickness h_c [115]

$$h_c = \frac{E\Gamma}{Z\sigma^2}, \tag{4.2}$$

where $Z = \frac{\pi c_e^{\,2}}{2}$ (with $c_e \sim 1.1215$) is a dimensionless driving force for channeling cracks extending through the entire thickness of the film when the elastic constants of the film are the same as those of the substrate [116, 117], Γ is the fracture energy of Si, and E is the Young's modulus. For Si thin film electrodes, stress σ in the film is bounded by the yield stress $\sigma_y = 1.75$ GPa (for lithiated Si) [16], , $E = 80$ GPa, $\Gamma = 10$ J/m^2, and based on Equation (4.2), Zhao et al. [24] estimated a critical film thickness of 130 nm. According to this analysis, brittle cracking becomes impossible within thin films thinner than the critical thickness given by Equation (4.2).

Experiments on 100 nm amorphous Si thin films on Cu substrate show that while through-the-thickness cracks form during cycling, the crack opening keeps increasing during cycling, and most importantly, the crack spacing is much larger than the film thickness [22]. Figure 4.1 shows the plan view of a 100 nm thick film after 12 cycles. This figure shows that crack spacing is of the order of 7-10 μm. The observed crack spacing in the Si thin film cannot be straightforwardly explained by conventional theories of thin film fracture mechanics.

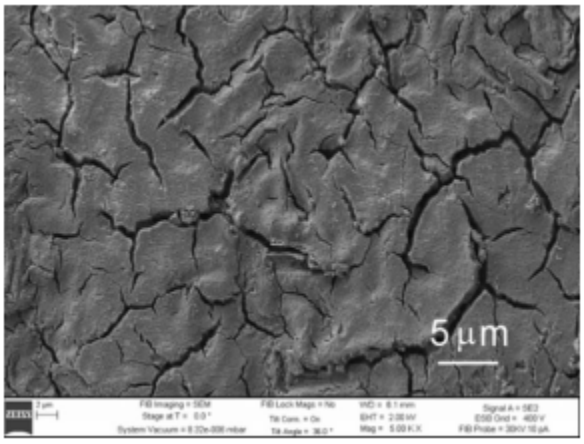

Figure 4.1: A 100 nm-thick Si film on Cu substrate after 12 cycles (Ref. [22]).

Most of the existing theories on crack patterns in thin films or multilayers [118-125] predict crack spacing on the same order as the film thickness except when the Young's modulus of the film is much larger than that of the substrate [124, 125]. This is generally consistent with experimental observations of crack patterns in engineering films/coatings [118, 120-122] as well as crack spacing in rock layers [123, 126]. Also, cracks in drying mud show an average spacing comparable to their depth [127], while

crack patterns in drying cornstarch and cooling lava even have columnar structures with crack spacing much smaller than the depth [128]. In contrast to these theories and observations, the aforementioned experiment shows that lithiated 100 nm thick Si films exhibited a mean crack spacing of 7-10 microns which is nearly two orders of magnitude larger than the film thickness. Since the Young's modulus of lithiated Si [19, 82] is actually smaller than that of Cu, this large difference between crack spacing and film thickness cannot be understood from the conventional theories of thin film fracture.

4.1. Crack spacing and emergence of a critical island size

In the following, we show that the apparent discrepancy mentioned above can be explained by considering plastic deformation within the Si thin film, as well as the shear resistance of the interface between lithiated Si and Cu. We note that Cu is known to yield at a tensile stress of about 70 MPa, and recent experiments have shown that [16] the lithiated Si film undergoes plastic flow as soon as the film stress reaches about $\sigma_Y^{Si} = 1 - 1.75$ GPa. Consider a Si film which already contained an array of cracks with spacing $2l_{cr}$ (Figure 4.2a). In this configuration, we ask if there exists a minimum crack spacing which would be so small that it does not allow an additional crack to be inserted in between the existing cracks. We assume this additional crack would form via plastic strain localization between two neighboring cracks in Si. Considering the free body diagram shown in Figure 4.2b, force equilibrium in the critical configuration when the Si patch just begins to yield indicates

$$\tau_{\text{int}} l_{cr} = \sigma_Y^{Si} h\,, \tag{4.3}$$

where τ_{int} is the interfacial shear strength between lithiated Si and Cu, which should be bounded by the shear flow stress of Cu and the interfacial friction strength, i.e.

$$\tau_{\text{int}} = \min(\tau_Y^{Cu}, \tau_f^{\text{int}})\,. \tag{4.4}$$

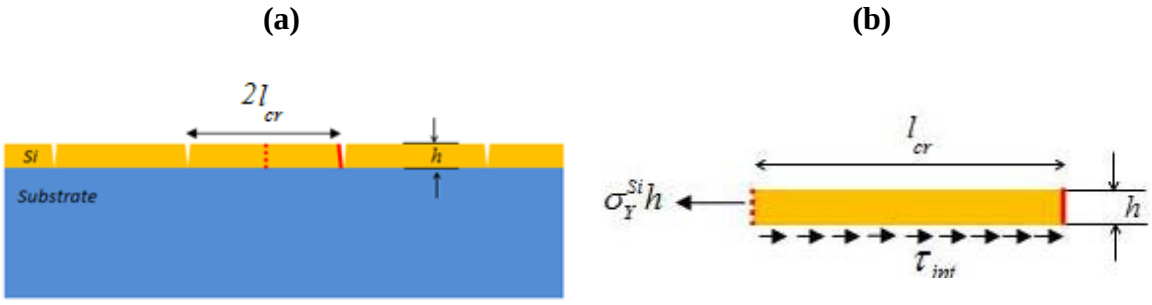

Figure 4.2: (a) A periodically cracked continuous thin film on a thick substrate; (b) Free-body diagram for half-period of the cracked film.

Since the shear flow stress of Cu is about $\tau_Y^{Cu} = 40$ MPa and the apparent friction strength of gold-mica (Silicate composite) interface has been measured to be also around $\tau_f^{\text{int}} = 40$ MPa [129], a rough estimate of the interfacial shear strength between lithiated Si and Cu is thus $\tau_{cr}^{\text{int}} = 40$ MPa. Further, taking $h =$ 100 nm and $\sigma_Y^{Si} = 1 - 1.75$ GPa immediately suggests that the minimum crack spacing preventing further plastic strain localization in Si film is

$$L_{cr} = 2l_{cr} = \frac{2\sigma_Y^{Si}}{\tau_{cr}^{\text{int}}} h\,, \tag{4.5}$$

which turns out to be around 5.1 to 8.9 μm. This length scale is in excellent agreement with the experimentally observed crack spacing in the 100 nm thick Si film. Below L_{cr}, plastic strain localization in Si becomes impossible because the stress in Si cannot reach the plastic flow stress of lithiated Si. Similar scaling laws as the one given in Equation (4.5) have been proposed for crack spacing in other material systems, such as Cr films on Al and stainless steel substrate [130], or silica films on Cu substrate [131].

The analysis presented above, once applied to patterned Si thin film electrodes, immediately suggests that when the lateral size of the islands falls below the critical length L_{cr}, given by Equation (4.5), stress in the island could not reach the yield stress, and hence, islands remain primarily elastic during cycling. Recent *in-situ* stress measurement in patterned Si islands are consistent with this conclusion [132]. Figure 4.3a shows variation of the nominal stress σ_{nom} vs. capacity, during the second and third charge/discharge of a pattern of square Si islands, with as-deposited thickness of 50 nm, lateral dimension of 7 μm, and edge-to-edge spacing of 5 μm on a quartz glass substrate whose thickness is 230 μm [132]. It should be noted that in this experiment, Si islands are actually deposited on a continuous 200 nm thick layer of Ti serving as the current collector in between Si islands and the quartz substrate. In Figure 4.3, the nominal stress σ_{nom} refers to a measure of the stress which is obtained by converting the curvature κ measured by the multi-beam optical stress sensor (MOSS) technique [115, 133] via the Stoney equation [134],

$$\sigma_{nom} = \frac{E_s h_s^{\,2} \kappa}{6(1-\nu_s)h_0}, \tag{4.6}$$

where h_0 is the as-deposited thickness of the islands, and h_s, E_s and ν_s are the thickness, Young's modulus and Poisson ratio of the substrate, respectively. This figure shows that the nominal stress-capacity curve has a nearly reversible behavior, which is indicative of nearly negligible plastic deformation in the system [132]. In contrast, Figure 4.3b shows the stress-capacity data for a set of square islands with lateral size of 17 μm and edge-to-edge spacing of 8 μm. In contrast to Figure 4.3a, stress irreversibility, and gradual shift of stress towards the tensile region, as evidence of plastic deformation, is clear in Figure 4.3b [132]. These observations are consistent with the analysis presented above.

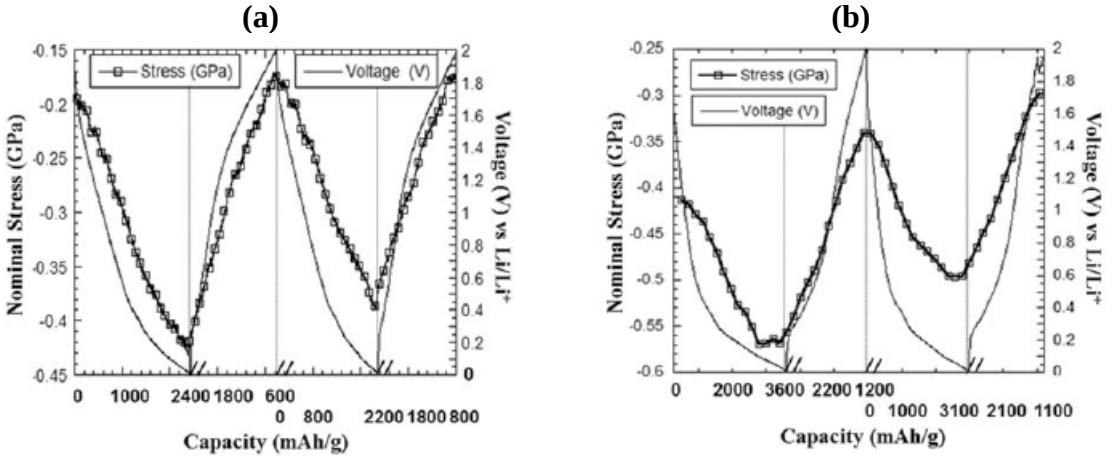

Figures 4.3: Evolution of nominal stress σ_{nom} (see Equation 4.6) vs. capacity in (a) 7 μm, and (b) 17 μm islands (Ref. [132]).

As mentioned before, application of the MOSS technique to patterned Si islands, requires a Stoney equation that relates wafer curvature to the stress in the islands. The stress-capacity data presented above are obtained using the usual Stoney equation, based on Equation (4.6). However, optical imaging of patterned Si thin films on Ti current collector, for which the stress-capacity data also exist, suggest that substantial relative sliding at the film-substrate interface takes place close to the edges of the island. Figure 4.4 shows an array of square Si islands with lateral dimension of 17 μm and thickness of 50 nm undergoing in-plane (as well as out-of-plane) expansion/contraction on a Ti current collector during lithiation/delithiation. It is observed that these Si islands undergo lateral expansions (up to ~30%), which can only occur in the presence of substantial interfacial sliding. Therefore, a modified Stoney formula that accounts for the effect of interfacial sliding is needed to relate curvature and stress in such systems [135].

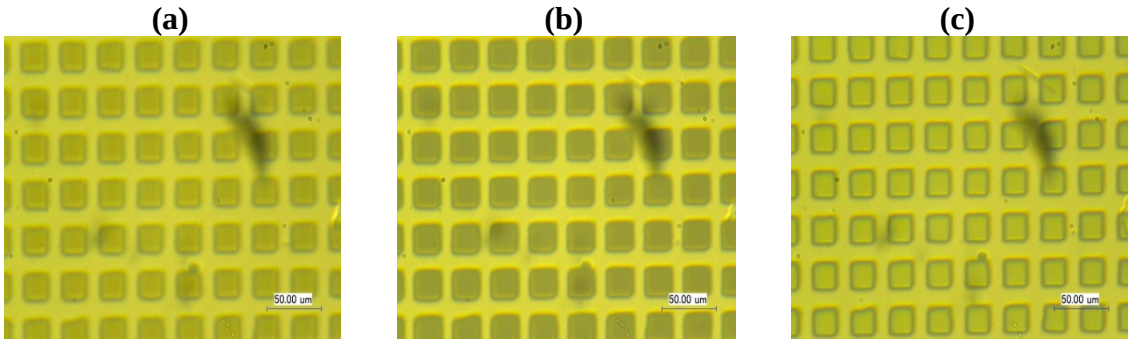

Figure 4.4: Micrographs demonstrating lateral expansion and contraction of Si islands on Ti current collector due to lithiation and delithaition. (a) As-deposited 17 μm x 17 μm Si islands; (b) Lateral dimensions of the Si islands expand by about 30% parallel to the substrate, demonstrating sliding along the interface; (c) Si islands return to their original size after delithiation. The scale bar is 50 μm (Ref. [136]).

Previously, the Stoney formula has been modified to deal with a variety of conditions such as non-uniformities (e.g. in the mismatch strain, material properties, and geometry [137-140]), large deformations [141], and discontinuities in the film (e.g. when a continuous film is replaced by an array of patterned lines [142, 143]), as well as other cases [115]. In these studies, the stress transfer zone is normally restricted to a very narrow region, on the order of the film thickness, close to the edges of the film. In the case of patterned Si islands on metallic current collectors, as discussed before, stress transfer occurs in a sliding zone which is expected to be much larger compared to the thickness of the islands, though small compared to the global dimensions of the whole film-substrate system. And, therefore, in such systems, the stress in the film can vary over a characteristic length scale much larger than the film thickness due to sliding at the film-substrate interface. Therefore, a modified Stoney formula that properly takes into account stress variation in the film is needed before one can relate the experimentally measured curvature data to the (maximum) stress in the patch.

4.2. A modified Stoney equation in the presence of interfacial sliding

In this section, modified versions of the conventional Stoney equation are presented for an array of islands under plane strain conditions in Section. 4.2.1, and for circular and square islands in Sections 4.2.2.

4.2.1. Two-dimenisonal modifed Stoney equation

We start by analyzing the two dimensional plane-strain problem of an array of thin film islands, each with length $2l$, thickness h_f and edge-to-edge gap $2s$ on a substrate of thickness h_s, as shown in Figure 4.5a. The Young's moduli of the film and substrate are denoted as E_f and E_s, respectively. Taking advantage of the symmetries in the problem, we focus on a half period of the structure with length $l+s$, located between section "A" passing through the midpoint of one patch and ending at section "B" bisecting the gap between the patch and its neighboring patch (Figure 4.5a). Figure 4.5b shows the free-body diagram of the portion of substrate between the two sections. To obtain the curvature induced in the substrate due to the stress in the film, we consider a virtual moment M at section "B" and invoke Betti's reciprocity theorem as follows. The total work done (per unit out-of-plane depth) by the interfacial stresses $\tau_{\text{int}}(x)$ through the displacement induced, along the interface, by the moment M is equal to the work done by the moment M through the rotation θ_τ induced by the islands at section "B":

$$M\,\theta_\tau = \int_0^l \tau_{\text{int}}(x)\,\delta_M(x)\,dx, \tag{4.7}$$

where $\delta_M(x)$ denotes the horizontal displacement at the interface induced by M. From the classical beam theory, the axial strain induced by M at the surface of the substrate is $\varepsilon_x = \dfrac{M\,h_s}{2\overline{E}_s I_s}$, where $\overline{E}_s = E_s$ for plane stress and $\overline{E}_s = \dfrac{E_s}{1-\nu_s^{\,2}}$ (ν_s being the Poisson ratio

of the substrate) for plane strain, and $I_s = \frac{1}{12} h_s^3$ is the moment of inertia of the substrate (per unit out-of-plane depth). Hence

$$\delta_M(x) = \varepsilon_x x = \frac{6M\,x}{\overline{E}_s h_s^2}. \tag{4.8}$$

On the other hand, the rotation θ_τ is related to the average curvature of the substrate κ via

$$\theta_\tau = -\kappa(l+s), \tag{4.9}$$

where the sign convention is such that tensile stress in the film causes positive curvature.

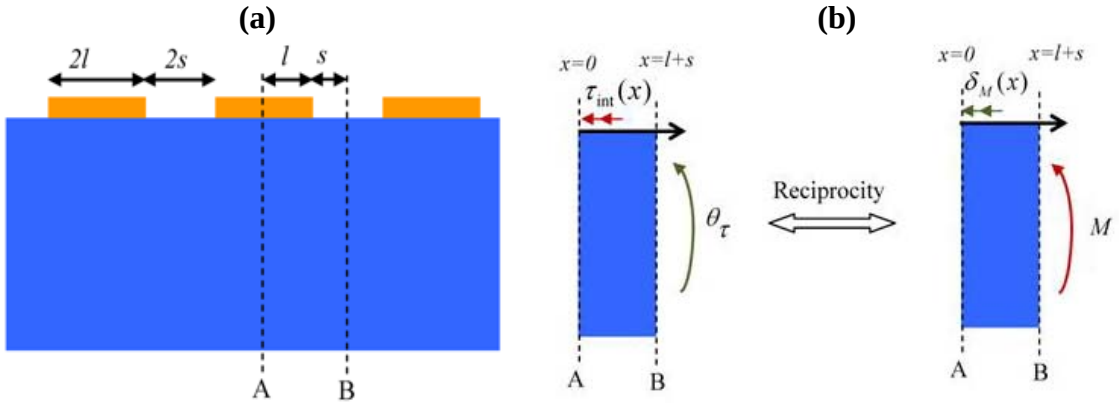

Figure 4.5: Modified Stoney equation for two-dimensional patterned films on substrate. (a) The geometry of the problem, and (b) the reciprocity theorem for determining the curvature of the system.

Substituting Equations (4.9, 4.8) into Equation (4.7), and introducing the dimensionless parameters $\tilde{x} = \frac{x}{l}$, $\tilde{\tau}_{\text{int}}(\tilde{x}) = \tau_{\text{int}}(x)/\tau_0$, where τ_0 is the interfacial sliding strength, the curvature κ can be expressed as

$$\kappa = -\frac{6\tau_0 l}{E_s h_s^2}\frac{l}{l+s}\int_0^1 \tilde{\tau}_{\text{int}}(\tilde{x})\,\tilde{x}\,d\tilde{x}\,. \tag{4.10}$$

To compute the integral on the right hand side of Equation (4.10), one needs to know the distribution of shear stress along the interface. Assuming that the film is thin enough to be treated as a membrane and that it would slide freely on the substrate as soon as the shear stress along the film-substrate interface attains τ_0, it can be shown that $\tau_{\text{int}}(x)$ should equal τ_0 within a distance l_p from the edge and then drops to zero beyond this region, i.e.

$$\tau_{\text{int}}(x) = -\begin{cases} \tau_0 \text{sign}(\sigma_f) & \text{for } l > x > l - l_p \\ 0 & \text{for } l - l_p > x > 0 \end{cases}. \tag{4.11}$$

A simple equilibrium consideration would show that the size of the sliding zone is $l_p = |\sigma_f| h_f / \tau_0$. Using Equation (4.11) along with this expression for l_p, Equation (4.10) then yields the following modified Stoney equation for curvature:

$$\kappa = \frac{6\tau_0 l}{E_s h_s^2}\frac{l}{l+s}\tilde{\sigma}_f\left(1 - \frac{\tilde{\sigma}_f}{2}\right)\text{sign}(\sigma_f), \tag{4.12}$$

where $\tilde{\sigma}_f = \frac{|\sigma_f| h_f}{\tau_0 l}$. In the limit of $\tilde{\sigma}_f << 1$, Equation (4.12) reduces to the conventional volume-averaged Stoney formula $\kappa = \frac{6\sigma_f h_f}{E_s h_s^2} \frac{l}{l+s}$.

In order to check the validity of the two-dimensional modified Stoney formula in Equation (4.12), we have performed finite element (FEM) calculations using ABAQUS to determine the curvature induced by a uniform thermal strain in an array of thin film patches on substrate. Three different patch spacings s = 1, 3 and 6 μm were considered. The Young's modulus and Poisson ratio of the patch are taken as 40 GPa and 0.22 (which are close to the values reported for lithitated Si [82]), and those of the substrate as 130 GPa and 0.34 (as given for copper by [115]). The patch length and thickness are taken to be 6 μm and 100 nm, respectively, and the substrate 50 μm thick. A rigid-plastic cohesive model is adopted to characterize the interfacial slipping under a sliding strength of 40 MPa. The results are shown in Figure 4.6 along with the theoretical prediction from the conventional Stoney formula as well as that from from the modified Stoney formula in Equation (4.12). The dimensionless parameter $\tilde{\kappa} = \frac{\kappa E_s h_s^2}{6\tau_0 l} \frac{l+s}{l}$ has been introduced. The predicted values of curvature from Equation (4.12), shown as the solid line in Figure 4.6, are in good agreement with the calculated results from FEM calculations. In contrast, the conventional Stoney formula exhibits up to 50 % underestimate of the maximum stress in the film.

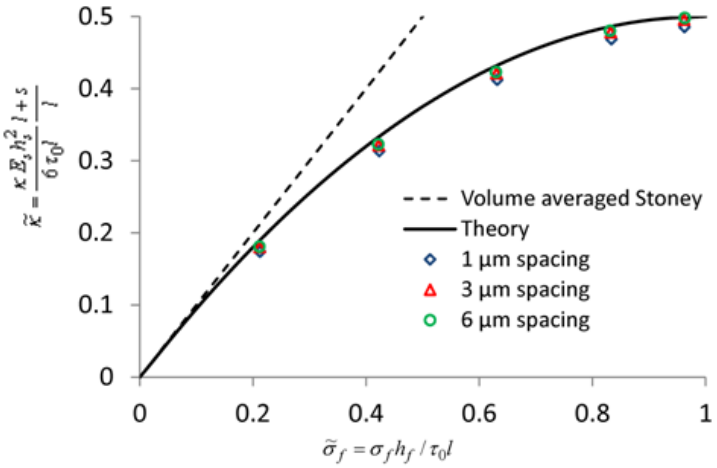

Figure 4.6: Modified Stoney equation for two-dimensional patterned films on substrate: comparison of FEM calculations and theoretical predictions of curvature for two-dimensional patterned films on substrate.

4.2.2 Three-dimensional modified Stoney equations

In this section, we will derive a modified Stoney formula for circular islands on substrate and then extend it to the more difficult case of square islands with the aid of FEM simulations.

(a) Circular islands

The approach taken in the preceding section may not be generally applicable to three-dimensional islands. For an array of circular islands, we consider a quarter of the unit cell of the periodic structure, as shown in Figure 4.7a and assume the stress within the island remains approximately axisymmetric. Following a procedure based on Betti's reciprocity theorem similar to the two dimensional case, it can be shown that the curvature induced in the substrate can be written in the following form

$$\kappa = -\frac{6\tau_0 R(1-\nu_s)}{E_s h_s^2}\frac{\pi R^2}{4(R+s)^2}\int_0^1 \tilde{\tau}_{\text{int}}(\tilde{r})\,\tilde{r}^2\,d\tilde{r}\,, \tag{4.13}$$

where R is the radius of the island, s is the half-spacing between islands, $\tilde{r} = \frac{r}{R}$ and ν_s is the Poisson ratio of the substrate. Compared to the two-dimensional case, the factor $1-\nu_s$ is a result of the three dimensional geometry.

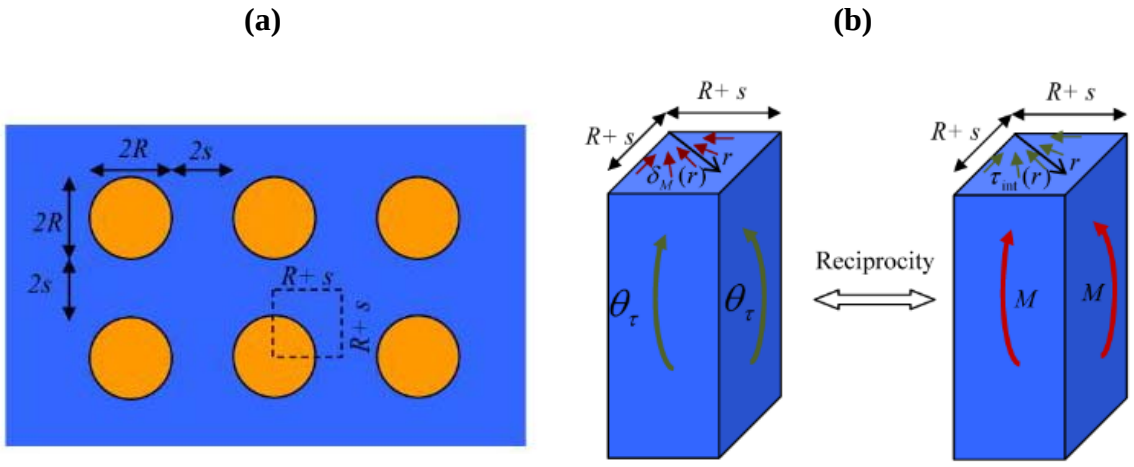

Figure 4.7: Modified Stoney equation for three-dimensional patterned films on substrate, and comparison with FEM calculations. (a) The geometry of the problem, and (b) the reciprocity theorem for determining the curvature of the system.

To calculate the integral in Equation (4.13), we again assume the following shear stress distribution at the interface

$$\tau_{\text{int}}(r) = -\begin{cases} \tau_0 \text{sign}(\sigma_f) & \text{for } R > r > r_p \\ 0 & \text{for } r_p > r > 0 \end{cases}. \tag{4.14}$$

in the limit of a very thin film. It follows that Equation (4.13) can be integrated to the following modified Stoney equation,

$$\kappa = \frac{6\tau_0 R(1-\nu_s)}{E_s h_s^2} \frac{\pi R^2}{4(R+s)^2} \left(\frac{1}{3} - \frac{\tilde{r}_p^3}{3}\right) \text{sign}(\sigma_f), \tag{4.15}$$

where, unlike the two-dimensional case, $\tilde{r}_p = \frac{r_p}{R}$ cannot be determined from equilibrium condition alone, but needs to be determined from both equilibrium and continuity conditions in the island. To determine $\tilde{r}_p$, the patch is considered as a plane-stress circular disk subject to a body force corresponding to the interfacial shear stress in the original problem. The axisymmetric deformation in the island is described by the following differential equation [144],

$$\frac{d}{dr}\left[\frac{1}{r}\frac{d}{dr}(ru)\right] + \frac{b(1-\nu_f{}^2)}{E_f} = 0, \tag{4.16}$$

where u is the radial displacement and b is the body force acting in the radial direction,

$$b = \frac{1}{h_f}\begin{cases} \tau_0 \,\text{sign}(\sigma_f) & \text{for } R > r > r_p \\ 0 & \text{for } r_p > r > 0 \end{cases}. \tag{4.17}$$

Now assume that the patch is subject to a uniform isotropic mismatch strain ε^*, as a result of Li insertion or other causes. The radial component of stress is related to the displacement via

$$\sigma_{rr} = \frac{E_f}{1-\nu_f{}^2}\left\{\frac{du}{dr} + \nu_f \frac{u}{r} - (1+\nu_f)\varepsilon^*\right\}. \tag{4.18}$$

Within the region $0 \le r \le r_p$, the differential Equation (4.16) and the boundary conditions $u = 0$ at both $r = 0$ and $r = r_p$ indicates that the stress in this region of the island is uniform,

$$\sigma_f = -\frac{E_f}{1-\nu_f}\varepsilon^*, \tag{4.19}$$

which is also the maximum stress in the island as a whole. Within the sliding region $r_p \le r \le R$, Equation (4.16) can be solved subject to boundary conditions $u = 0$ at $r = r_p$ and $\sigma_{rr} = 0$ at $r = R$, and finally r_p can be obtained in terms of ε^* from the continuity of σ_{rr} at $r = r_p$. Using Equation (4.19) to replace ε^* with the maximum stress σ_f in the island, we find that the result can be expressed in terms of the following dimensionless form

$$\tilde{r}_p = (1+\nu_f)(1-\nu_f)^{-2/3} A^{-1/3} - (1-\nu_f)^{-1/3} A^{1/3}, \tag{4.20}$$

where

$$A = (3\tilde{\sigma}_f - 2 - \nu_f) + \sqrt{9\tilde{\sigma}_f^2 - 6(2+\nu_f)\tilde{\sigma}_f + \frac{5+3\nu_f}{1-\nu_f}}, \tag{4.21}$$

and $\tilde{\sigma}_f = \dfrac{|\sigma_f| h_f}{\tau_0 R}$. Thus, for a given maximum stress σ_f, $\tilde{r}_p$ is given by Equations (4.20, 4.21), and the curvature can be obtained from Equation (4.15). It should be pointed out that Equation (4.15) in conjunction with Equations (4.20, 4.21) reduces to the

conventional volume-averaged Stoney formula $\kappa = \frac{6\sigma_f h_f (1-\nu_s)}{E_s h_s^2} \frac{\pi R^2}{4(R+s)^2}$ in the limit of $\tilde{\sigma}_f << 1$. Figure 4.8a shows the results of FEM calculations for three different cases with s = 1, 3, 6 μm and R =3 μm, along with the theoretical predictions from the above analysis and from the conventional Stoney formula, for the normalized curvature $\tilde{\kappa} = \frac{\kappa E_s h_s^2}{6(1-\nu_s)\tau_0 R} \frac{4}{\pi} \left(\frac{R+s}{R} \right)^2$. Numerical values for other parameters are the same as those adopted for the two dimensional case. It is seen that, while the theoretical predictions from Equations (4.15, 4.20, 4.21) are in fair agreement with the FEM simulations, the conventional Stoney formula could lead to significant underestimate of the maximum stress in the film.

(a)

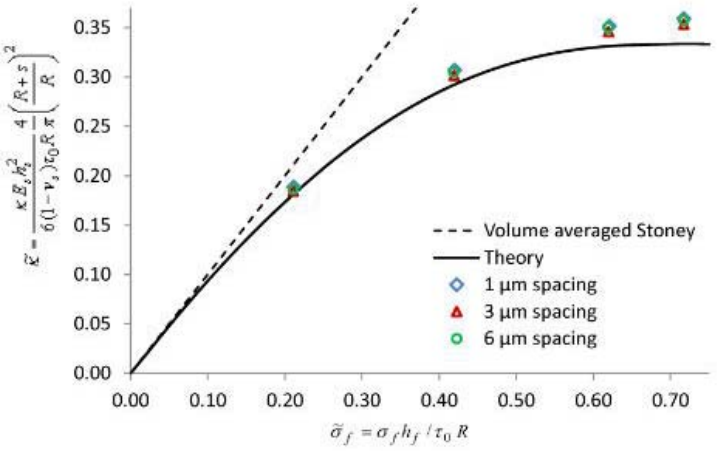

(b)

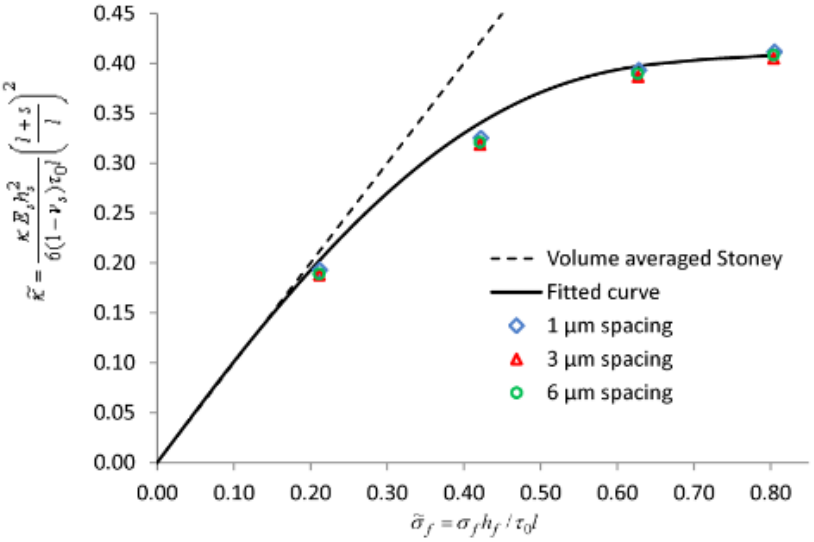

Figure 4.8: Comparison of FEM calculations and theoretical predictions of curvature for (a) circular patches where the solid line is the theoretical prediction; (b) square patches where the solid line is based on a fitting scheme.

(b) Square islands

For the case of square islands, the shear stresses along the interface seem too complicated for an analytical study. For a simplified treatment, the square patches can be approximated as an equivalent array of circular patches which induce the same curvature in the substrate at the same level of maximum stress. To this end, we rewrite Equation (4.15) in the following form

$$\kappa = \frac{6\tau_0 R_{eq}(1-\nu_s)}{E_s h_s^2}\left(\frac{l}{l+s}\right)^2 (\frac{1}{3} - \frac{\tilde{r}_p^3}{3}) \text{ sign}(\sigma_f). \tag{4.22}$$

Here, we assume that $\tilde{r}_p$ is still obtained through Equations (4.20, 4.21), but with dimensionless stress $\tilde{\sigma}_f = \frac{|\sigma_f| h_f}{\tau_0 l}$. Any change in the form of curvature dependence on the maximum stress is then lumped into an equivalent radius of the patch, which from a dimensional analysis should be in the form $R_{eq} = l\,\tilde{R}_{eq}(\tilde{\sigma}_f)$. For Equation (4.22) to be reduced to the conventional Stoney formula, $\tilde{R}_{eq}(\tilde{\sigma}_f)$ must tend to unity as $\tilde{\sigma}_f$ approaches zero. With this asymptotic behavior, we propose that $\tilde{R}_{eq}(\tilde{\sigma}_f) = 1 + \alpha\,\tilde{\sigma}_f{}^{\beta}$ where α and β are constants to be obtained from fitting Equation (4.22) to a set of FEM calculations. In the FEM simulations lateral size of the islands is 6 μm and the spacing between islands has been varied as shown in Figure 4.8b. Our calculations indicate that $\alpha = \frac{1}{4}$ and $\beta = \frac{1}{2}$ provide an acceptable fit, as shown in Figure 4.8b.

4.3. Interpretation of *in-situ* stress-measurements in Si patterned islands

In this section, we will apply the modified curvature-stress relationships presented in the previous section to the stress-measurement in patterned Si thin film electrodes. Figure 4.9 is the same nominal stress-capacity data presented in Figure 4.3. As it was mentioned earlier (see Figure 4.3a), reversibility of the stress data in this case suggests that the sliding zone should have been fully developed at some point during cycling. From Figure 4.8b, we note that the saturated value of

$$\widetilde{\kappa} = \frac{\kappa E_s h_s^2}{6(1-\nu)\tau_0 l}\left(\frac{l+s}{l}\right)^2 \tag{4.23}$$

is ~ 0.42. During cycling, half-length of the islands l changes with Li concentration. Ignoring change in the dimensions due to elastic strain, we can relate the instantaneous length l to the initial length l_0 according to

$$\lambda = \frac{l}{l_0} = (1+2.7\,z)^{1/3}, \tag{4.24}$$

where $z = \frac{\text{cpacity (mAh/g)}}{3579\ \text{(mAh/g)}}$ is the (dimensionless) state of charge [16]. Furthermore,

$\sigma_{nom} = \frac{\kappa E_s h_s^{\,2}}{6(1-\nu_s)h_0}$ form Equation (4.6), is related to $\widetilde{\kappa}$ via

$$\sigma_{nom} = \frac{\widetilde{\kappa}\tau_0 l_0}{h_0}\lambda^3\left(\frac{l_0}{l_0+s_0}\right)^2. \tag{4.25}$$

Using the saturated value of ~ 0.42 for $\widetilde{\kappa}$, Equation (4.25) can be written as,

$$\sigma_{nom} \sim 0.42\frac{\tau_0 l_0}{h_0}(1+2.7z)\left(\frac{l_0}{l_0+s_0}\right)^2. \quad (4.26)$$

Note that this equation does not predict a zero stress at zero capacity, because we have assumed that the shear lag zone is fully developed. Similarly, the nominal stress data presented in Figure 4.3a (for the second cycle) start from a non-zero stress which is due to a residual stress in the islands induced by the electrochemical reactions (and other irreversible phenomena) in the first cycle. However, after shifting Equation (4.26) to start from the stress measured at the end of the first cycle (this requires a prestress of ~ -70 MPa), an estimate of the interfacial shear stress τ_0 can be obtained by fitting. The linear fits (plotted as solid black lines) shown in Figure 4.9 suggest that the interfacial shear stresses (in absolute values) are ~13.4 MPa, and 18.4 MPa from the lithiation and delithiation data (shown respectively by open squares and circles), respectively.

The values obtained here for the interfacial stresses are much smaller than the yield stress of the underlying 200 nm-thick Ti current collector (which is expected to be larger than that of bulk Ti, i.e. ~100-120 MPa [145]), which suggests that stress relaxation is unlikely to be due to the plasticity in Ti, and rather highlights the interfacial sliding as the dominant mechanism of stress relaxation. This is also consistent with the micrographs of the patterned islands shown in Figure 4.4 which suggest a remarkable lateral expansion/contraction upon lithiation/delithiation. Also note that the values obtained here are comparable to the sliding resistance measured for gold-mica interface, i.e. 40 MPa [129].

It is interesting to compare the stress-capacity data of a patterned film with that of a continuous film. Experimental stress-capacity data for continuous 50 nm thin films show an initially linear response which can be approximated as $\sigma_{nom}^{\infty} = \sigma_0 - 0.00315c$, where c is capacity in mAh/g, σ_0 is the prestress in the film, and σ_{nom}^{∞} is the measured nominal stress in the film, both in GPa. This empirical equation yields ~1.2 GPa change in the nominal stress corresponding to the lithiation capacity of 380 mAh/g [17]. If one assumes that the islands are fully constrained against lateral expansion, then stress in the islands should be obtained through

$$\sigma_{nom} = \left(\frac{l_0}{l_0 + s_0} \right)^2 \sigma_{nom}^{\infty}. \tag{4.27}$$

The stress-capacity data using this equation is shown in Figure 4.9, by the dashed line. One can also use the linear elastic theory, in conjunction with the assumption that the islands are fully constrained against lateral expansion, and obtain the following equation for nominal stress

$$\sigma_{nom} = \frac{E_f}{1-\nu_f} \left(\frac{l_0}{l_0 + s_0} \right)^2 (1-\lambda)\lambda^3, \tag{4.28}$$

This equation is also shown in Figure 4.9 (the dotted line), for the representative values of $E_f = 40$ GPa, and $\nu_f = 0.22$. As evident in the figure, stress predicted from either of the Equations (4.27) or (4.28) grows very rapidly with concentration, suggesting that the reversible behavior observed in 7 μm islands cannot be explained without considering the relaxation effect caused by the interface.

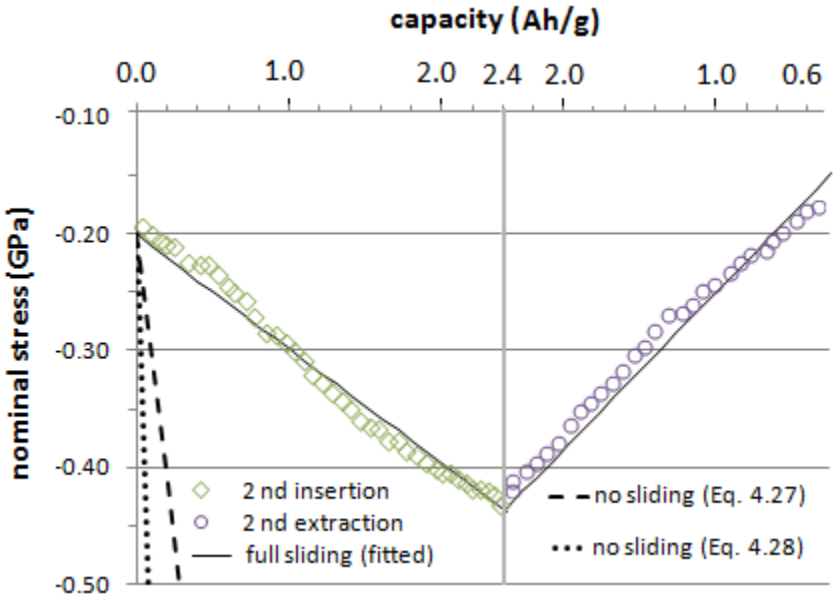

Figure 4.9: Nominal stress (Equation 4.6) vs. capacity. Solid lines are fits obtained from full sliding model by tuning the interfacial strength τ_0 (Equation 4.26). The dashed, and dotted lines are predictions obtained respectively from Equations (4.27), and (4.28), without allowing for lateral expansion of the islands.

With the value of τ_0 obtained above, one can estimate size of the sliding zone in a square island during intercalation, using the approximate equation

$$l_p \sim \frac{\sigma_{nom}^{\infty} h_0}{0.85\tau_0}, \tag{4.30}$$

where σ_{nom}^{∞} is the nominal stress in a continuous thin film, and the numerical factor 0.85 is an approximate factor obtained through finite element calculations. The sliding zone does not fully develop for a sufficiently large island, and the instantaneous half-length of the island can be calculated using an approximate equation [132]

$$l \sim l_p + (l_0 - \frac{l_p}{\lambda}) . \tag{4.31}$$

Having $\tilde{\sigma}_f = \frac{\sigma_f h_f}{\tau_0 l} = \frac{\sigma_{nom}^{\infty} h_0}{\tau_0 l}$, one can obtain $\tilde{\kappa}$ from Figure 4.8b, and finally σ_{nom} can be obtained as

$$\sigma_{nom} = \frac{\tau_0 l^3}{h_0 l_0^2} \frac{{l_0}^2}{\left(l_0 + s_0\right)^2} \tilde{\kappa} . \tag{4.32}$$

Prediction of σ_{nom} as a function of capacity, using Equation (4.32), for a pattern of islands with $2l_0 = 40$ μm, and spacing of $2s_0 = 18$ μm, is shown in Figure 4.10 (the solid lines)**.** The prediction is in good agreement with the experimental data for most of the intercalation half-cycle. However during Li-extraction, the predicted stress values deviate from the experimental data. This deviation can be understood by noting that, according to the analysis above, stress in the center of island σ_{nom}^{∞} reaches ~ 0.98 GPa, after intercalation up to 300 mAh/g, which is very close to the nominal yield stress of a continuous film in a charging half-cycle, suggesting possibility of plastic deformation during lithiation. This is also consistent with the observed irreversibility in the stress-capacity data shown in Figure 4.10.

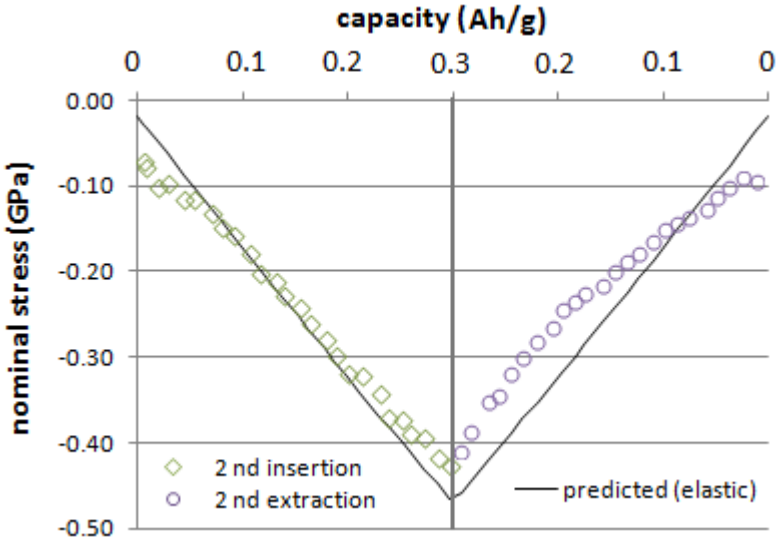

Figure 4.10: Nominal stress (Equation 4.6) vs. capacity. Solid lines are predictions based on partial sliding along the interface (Equation 4.32). Deviation of the predicted values form the experiment suggest that plastic deformation might have happened during lithiation.

One can also use Equation (4.30) to obtain size of sliding zone in an island when plastic flow happens in its center,

$$l_p \sim \frac{\sigma_{Y,nom}^{Si} h_0}{0.85\tau_0},$$

where $\sigma_{Y,nom}^{Si}$ is the nominal yield stress for a continuous thin film. Using $\sigma_{Y,nom}^{Si} = 1\,\text{GPa}$, and the initial thickness h_0=50 nm, we obtain $l_p \sim$ 4.39 μm. This suggests that islands smaller than $2l_p \sim$ 8.78 μm should remain elastic during intercalation, which is again consistent with the observation of reversible stress-capacity data in 7 μm islands.

4.4. Summary

In this chapter, crack spacing observed in continuous Si thin film electrode was explained in terms of plasticity in the film as well as the sliding resistance of the interface. Based on the experimental observation of crack spacing, we proposed that patterned thin films with islands smaller than the crack spacing should remain elastic during cycling. This prediction was shown in consistency with reversible stress data obtained through *in-situ* stress measurements. Furthermore, a modified Stoney equation was proposed in the presence of interfacial sliding. Application of the modified equation to the stress measurements in the patterned electrodes suggested that the magnitude of the shear stresses acting along the interface should be ~13.4 MPa to 18.4 MPa. Since this value is less than the yield stress of typical metallic substrates, it was concluded that in the systems of Si thin film electrodes on typical metallic current collectors, it is the interface which plays an important role in stress relaxation through allowing for lateral expansion of Si.

Chapter 5

Critical size for interfacial delamination of patterned Si thin film electrodes

The aim of this chapter is to present a method to deduce the critical size for interfacial delamination of thin film electrodes by examining the critical conditions for the nucleation and propagation of interfacial cracks at the film-substrate interface under plane strain and axisymmetric conditions. The motivation for this study has come from the following experimental observations on the delamination behaviors of Si thin film electrodes [22]. A first observation, already explained in the former chapter, was that a continuous Si thin film with thickness of 100 nm exhibited through-the-thickness cracks with spacing in the range of 5-10 μm due to lithiation and delithiation. Next, a set of experiments was performed to investigate the fracture behaviors of patterned Si thin film square islands on Cu with the same film thickness of 100 nm but 3 different lateral dimensions: 7 μm x 7 μm, 17 μm x 17 μm and 40 μm x 40 μm. Scanning electron microscope images of the 7 μm x 7 μm Si islands, as shown in Figure 5.1a, indicated that they stayed well adhered to the substrate, while a fraction of the 17 μm x 17 μm islands and all of the 40 μm x 40 μm islands peeled off the substrate after 30 charge cycles (see Figure 5.1b) [22]. Therefore, a critical island size seems to exist on the order of 10-20

μm for interfacial delamination of patterned thin films with thickness of 100 nm. The existing theories of interfacial delamination [115, 146-149] simply cannot explain why the 100 nm thick islands exhibit such size-dependent delamination behavior in the size range nearly two orders of magnitude beyond the film thickness. In the present study, we show that this effect can only be rationalized by considering thin film delamination in the presence of large scale interfacial sliding. In the previous chapter, we have already discussed existing evidences indicative of substantial interfacial sliding leading to crack spacing much larger than film thickness (in unpatterned continuous thin films), remarkable stress relaxation by allowing for lateral expansion, as well as prediction of a critical size below which islands remain elastic. By accounting for the effect of interfacial sliding, we will develop a method to deduce the critical size for interfacial delamination in patterned electrode structures by examining the critical conditions for the nucleation and propagation of edge or center cracks at the film-substrate interface under plane strain or axisymmetric conditions.

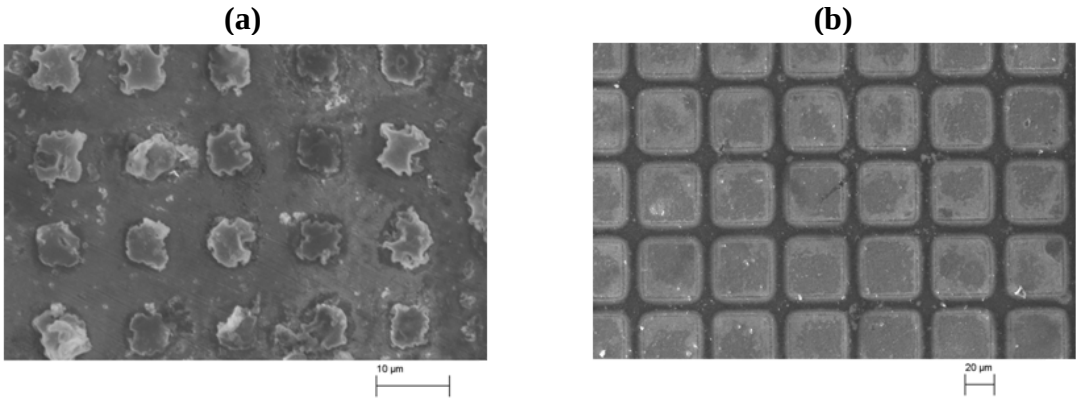

Figure 5.1: SEM images of patterned Si islands surface morphology after 30 cycles, showing that (a) while 7 µm x 7 µm islands stay well-adhered to the substrate (scale bar = 10 µm), (b) 40 µm x 40 µm islands have delaminated away from the substrate (scale bar = 20 µm), from Ref. [22].

This chapter is organized in the following order. In Section 5.1, the conventional theory of film delamination from substrate is briefly reviewed. It will be shown that the theory cannot explain the anomalous size effect observed in patterned Si thin film, unless one takes into consideration the effect of interfacial sliding. In Section 5.2, the behavior of edge cracks is analyzed by accounting for the effect of interfacial sliding, under plane strain as well as axisymmetric condition. In Section 5.3, a similar analysis is presented, for the interfacial cracks positioned at the center of islands. We conclude this chapter, in Section 5.4, with a summary of the results.

5.1. Modification of the conventional theory of film delamination

Theories of fracture mechanics and diffusion-induced stresses have been employed to model fracture of electrodes, with results suggesting existence of a critical

size and charging rate below which fracture becomes impossible [13, 20, 23, 24, 53-57, 150]. A widely accepted result is that sufficiently thin electrodes at sufficiently low charging rates are resistant against fracture in the thickness direction. In Si thin-film electrodes deposited on substrate, it is of particular importance to note that that although the electrochemical cycling could generate microcracks through the film thickness, the fractured film can still serve as the active material as long as it can remain adhered to the current collector. In fact, through-the-thickness cracks in such systems can alleviate diffusion-induced stresses by facilitating volume changes associated with Li insertion/extraction. Therefore, while fracture in thin film electrodes partly decreases their capacity due to the formation of solid-electrolyte interphase (SEI) layers at newly created cracked surfaces, film delamination is a far more critical issue to capacity fading in such electrodes.

Delamination of thin films on substrate has been widely studied in the literature (a treatise on this topic can be found in Ref. [115]). An assumption commonly made in modeling delamination of thin films on substrate is that the film is well-bonded to the substrate with no interfacial sliding. Under plane strain conditions, a well-known result is that the energy release rate associated with an edge delamination crack reaches a steady-state value of

$$G_0 = \frac{(1-\nu^2)\sigma_f^2 h}{2E}\ , \tag{5.1}$$

as soon as the crack size becomes comparable to or larger than the film thickness *h*, where σ_f is the stress in the film, and E and ν are the Young's modulus and Poisson ratio of the film, respectively [115, 148]. However, when the interfacial sliding strength is much smaller than the stress in the film, as is the case expected for a Si electrode on a current collector, a large scale interfacial sliding zone would be expected near the edges of the film. If the length of the film is larger than the size of the sliding zone, a delamination crack would grow in a steady state manner as soon as the crack size is larger than the film thickness. In this state, the energy release rate is independent of the crack size, and there is no size effect (Figure 5.2a). On the other hand, if the interfacial sliding zones from the island edges are so large that they extend over the entire island (Figure 5.2b), a strong delamination size effect would emerge over the size scale associated with the size of the sliding zones, rather than the film thickness. The shaded area in Figure 5.2b shows the region in which stress is released as two edge cracks nucleate and grow to a size *a*. It is evident that the shaded area in Figure 5.2b would shrink as the island size is reduced, and hence the energy release rate is expected to decrease. This is in contrast to the case shown in Figure 5.2a, which corresponds to a relatively large island size compared to the size of the sliding zones, leading to a size-independent energy release rate.

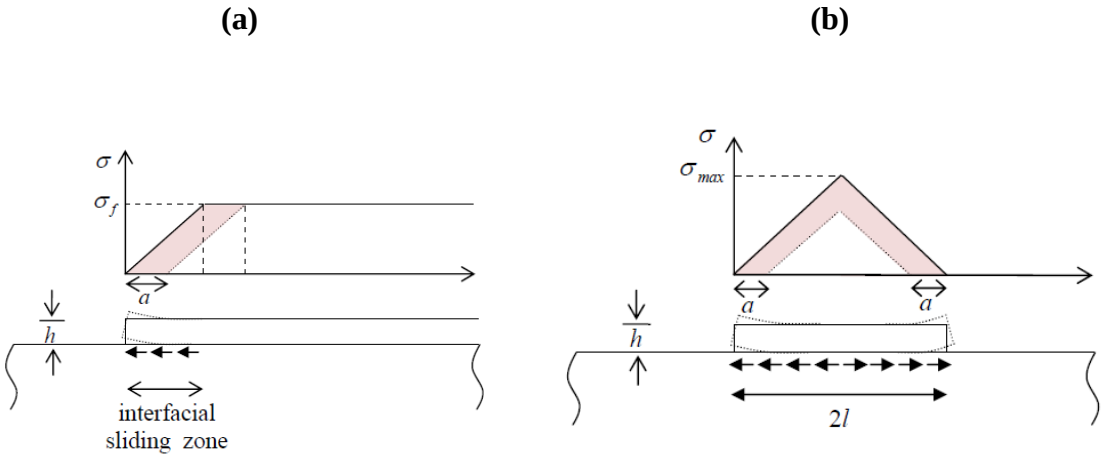

Figure 5.2:. Schematic of an edge delamination crack in a thin film on substrate in the presence of large scale interfacial sliding. (a) The crack grows in a steady state manner when the film width is much larger than the interfacial sliding zone at the film edge. (b) The interfacial delamination becomes dependent on the island size as the sliding zones from island edges overlap. In this case, the energy release rate for interfacial delamination is expected to decrease as the island size is reduced.

As the size of the interfacial sliding zones also determines the length scale over which the normal stress in the film reaches its maximum value, the size effects associated with interfacial sliding immediately suggests an explanation for the experimentally observed correlation between the fracture spacing in a continuous Si thin film and the critical size for interfacial delamination in patterned Si islands. Therefore, interfacial sliding between lithiated Si electrodes and substrate, which can occur on a much larger length scale than the film thickness, is a key to deducing the critical size for interfacial delamination in patterned Si electrodes. The reason that the conventional theories of interfacial delamination cannot explain the experimental observation that Si islands with thickness of 100 nm and length of 7 μm stayed well adhered on the substrate while those with the same thickness but length of 40 μm delaminated away can be attributed to the

fact that the assumption of well-bonded and non-slipping interface, while applicable to many conventional thin film-substrate systems, no longer holds in the case of lithiation of high-capacity electrodes.

In the following, we will deduce the critical size for interfacial delamination by detailed plane strain and axisymmetric analysis of potential nucleation and growth of edge and center interfacial cracks in the presence of large scale interfacial sliding. We will take advantage of the symmetry in the problem to simplify the analysis. Furthermore, we will treat the edge and center cracks separately, since their coexistence would decrease the elastic energy release rate in the islands as the driving force for crack nucleation and growth. The interface between the island and substrate is assumed to be well-bonded under small shear tractions but interfacial sliding is allowed as soon as the interfacial shear stress reaches a critical value τ_0. It is also assumed that the sliding follows a perfectly plastic response so that the interfacial shear stress never exceeds the sliding strength τ_0. The immediate consequence of this behavior is that the interfacial sliding zones start to develop at the edges of the film and spread toward the center of the island. Once they spread to the center of the island, the entire island would be sitting on top of a slippery surface and can freely expand upon further lithiation. This is the case as long as deformation within the island remains elastic, i.e. the maximum stress in the island does not exceed the flow stress of lithiated Si.

5.2. Nucleation and growth of edge delamination cracks in the presence of large scale interfacial sliding

In this Section, we will investigate the nucleation and growth of edge delamination cracks in a Si island with interfacial sliding zones spreading over the entire island. For simplicity, it will be assumed that the film is thin enough that variation of stress in the thickness direction can be neglected.

5.2.1. Plane strain analysis

Consider a Si island of length $2l$ and thickness h on a substrate, with edge delamination cracks of size a at the interface at both edges of the island, as shown in Figure 5.3. Assuming that the interfacial sliding zones from both edges of the island overlap, the axial stress distribution in half of the patch would be given as

$$\sigma_{xx} = \frac{\tau_0}{h}\begin{cases} l-a-x & l-a>x>0 \\ 0 & l>x>l-a \end{cases}, \tag{5.2}$$

where x is distance from the center of island. The total elastic energy stored, per unit out-of-plane length, in half of the island is obtained as

$$U_{el} = \int_0^{+l} \frac{1-\nu^2}{2E}\sigma_{xx}^2 dx = \frac{(1-\nu^2)\tau_0^2}{2hE}\frac{1}{3}(l-a)^3, \tag{5.3}$$

where E and ν are, respectively, the Young's modulus and Poisson's ratio of the film. To investigate the criterion for crack growth, we first note that the elastic energy release rate G is

$$G = -\frac{dU_{el}}{da} = \frac{(1-\nu^2)\tau_0^2}{2hE}(l-a)^2 . \tag{5.4}$$

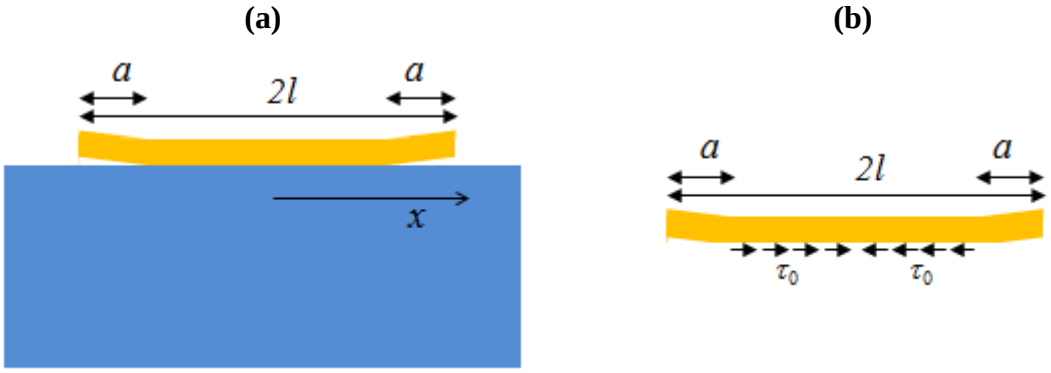

Figure 5.3: Schematic of (a) a Si island on substrate with edge delamination cracks and (b) free-body diagram of the island.

Interface delamination is accompanied with formation of new surfaces which increases the total free energy of the system. Denoting the interface fracture energy (toughness) by Γ, the total surface energy of the system U_{surf} increases at the rate of

$$\frac{dU_{surf}}{da} = \Gamma . \tag{5.5}$$

The Griffith condition for crack growth is that the elastic energy release rate must exceed the growth rate of surface energy, that is $G > dU_{surf}/da$, which yields

$$(l-a) > \sqrt{\frac{2hE\Gamma}{(1-\nu^2)\tau_0^2}} . \tag{5.6}$$

For an initially crack-free interface, i.e. $a = 0$, Equation (5.6) suggests that edge delamination at the interface is only favorable for islands larger than a critical length,

$$l > l_{cr,nuc} = \sqrt{\frac{2hE\Gamma}{(1-\nu^2)\tau_0^2}}\,. \tag{5.7}$$

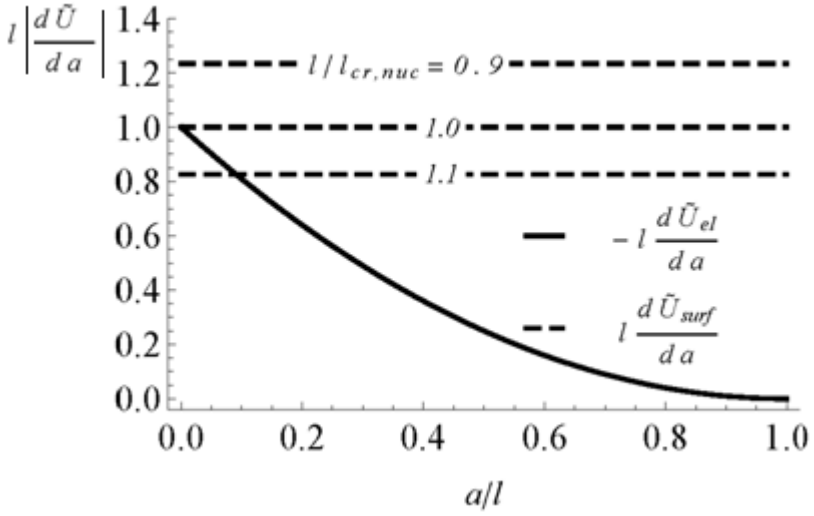

Figure 5.4: Plane strain analysis of interfacial delamination of a Si island on substrate. Elastic energy release rate and surface energy growth rate *vs*. crack length for various island sizes.

In this case, nucleation of edge interfacial cracks decreases the total free energy of the system. Figure 5.4 shows the variations of the elastic energy rate *vs*. the crack length a, where the dimensionless parameters $\widetilde{U}_{el} = \dfrac{2hEU_{el}}{(1-\nu^2)\tau_0^2 l^3}$ and $\widetilde{U}_{surf} = \dfrac{2hEU_{surf}}{(1-\nu^2)\tau_0^2 l^3}$ have been introduced. As shown in this figure, the elastic energy release rate associated with crack growth decreases with the crack length, while surface energy rises at a constant rate. Therefore, the crack is expected to be arrested at a residual length a_{arr}. This

residual length can be obtained from the condition that the total released elastic energy of the system prior to arresting has been completely consumed to create new surfaces, and thus there is no more energy available for crack to grow. In the absence of any source of energy dissipation, we can write

$$U_{el}(a=0)-U_{el}(a=a_{arr})=U_{surf}(a=a_{arr})-U_{surf}(a=0). \tag{5.8}$$

Straightforward manipulation shows that

$$a_{arr}=\frac{1}{2}\left(3l-\sqrt{3(4l_{cr,nuc}^2-l^2)}\right). \tag{5.9}$$

Figure 5.5a shows how a_{arr}/l varies with $l/l_{cr,nuc}$. One can easily verify that at this crack length, the elastic energy release rate becomes less than the surface energy growth rate. An interesting case happens when $a_{arr}\geq l$, corresponding to the scenario when the two edge cracks would grow all the way to the center of the island. In this case, the island will peel off from the substrate. It can be shown that this is the case only when the length of the island is larger than a critical length associated with full delamination,

$$l\geq l_{cr,del}=\sqrt{3}l_{cr,nuc}=\sqrt{\frac{6hE\Gamma}{(1-\nu^2)\tau_0^2}}. \tag{5.10}$$

To further elucidate the delamination mechanisms, Figure 5.5b shows changes in the dimensionless elastic and surface energies of the system, i.e. $\left|\Delta\widetilde{U}_{el}\right|=\widetilde{U}_{el}(0)-\widetilde{U}_{el}(a)$, and $\Delta\widetilde{U}_{surf}=\widetilde{U}_{surf}(a)-\widetilde{U}_{surf}(0)$, for various island sizes, as a function of the crack

length. It can be seen that, in the critical case of $l = l_{cr,del} = \sqrt{3} l_{cr,nuc}$, marked by a solid circle in Figure 5.5b, the total released elastic energy is just enough to drive the crack all the way to the center. As is evident from the same figure, larger islands with $l = 2l_{cr,nuc} > l_{cr,del}$ have even higher elastic energy and will delaminate away. However, for a shorter island with $l = 1.5 l_{cr,nuc} < l_{cr,del}$, the surface energy grows beyond the total elastic energy available in the island, indicating that the full delamination is impossible, in consistence with Equation (5.10). In the latter case, the ultimate length of the arrested crack can be obtained via Equation (5.9).

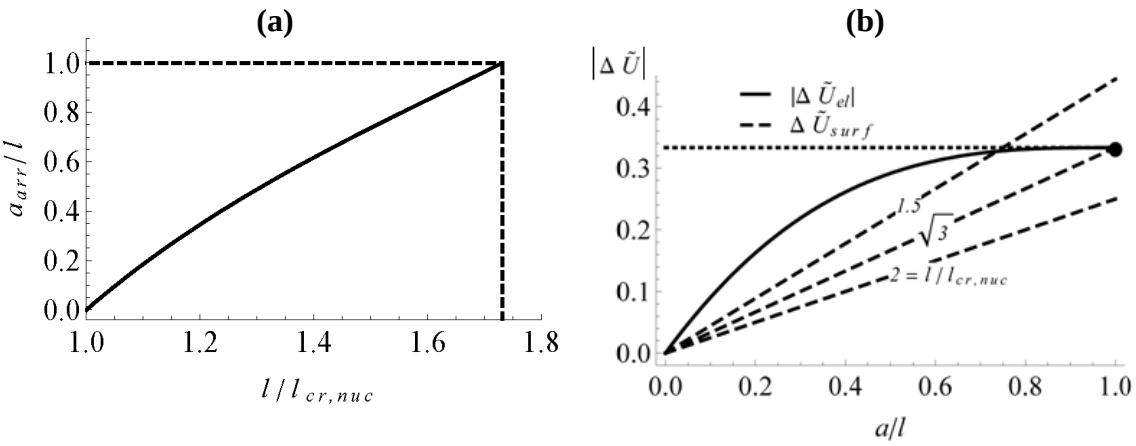

Figure 5.5: Plane strain analysis of interfacial delamination of a Si island on substrate. (a) Length of the arrested edge crack as a function of the island size; (b) Changes in the elastic energy and surface energy as a function of the crack length for different island sizes.

A couple of remarks are worth making at this point. While in the above analysis we have considered a pair of symmetrical edge interfacial cracks, one can verify through

straightforward analysis that consideration of a single edge crack does not change the results. Furthermore, in the present analysis, we have ignored the elastic energy stored in the substrate. Treating substrate as an elastic half-plane, a dimensional analysis would reveal that the ratio of elastic energy stored in the substrate to that in the film scales as $\frac{E h}{E_s (l-a)}$, where E_s is the Young's modulus of the substrate. Therefore, while our analysis is exact for the case of a rigid substrate, it remains valid even for an elastic substrate as long as the length of the island in contact with the substrate is much larger than the thickness of the island. This is indeed the case for patterned Si thin film electrodes with length on the order of tens of micrometers and thickness of a few hundred nanometers. As the island loses its contact with the substrate along the interface with contact area shrinking to a size comparable to the film thickness, the above assumption starts to break down. However, when this happens, the island can be considered as having effectively detached from the substrate.

For further physical insights, some numerical estimates of the critical length scales for interfacial delamination would be helpful. For a 100 nm thick Si patch with $E = 40$ GPa and $\nu = 0.22$ (for lithiated Si [19, 82]), $\tau_0 \approx 10$ MPa (for patterned Si thin films [132]), and a typical value of 1 J/m^2 for the interface energy Γ, the critical island sizes for crack nucleation and full delamination are estimated to be $2l_{cr,nuc} \approx 18.3$ μm and $2l_{cr,del} \approx 31$ μm, respectively, corresponding to maximum stresses of 0.92 GPa and 1.59 GPa in the center of the island prior to delamination. These results are in good agreement

with the experimentally observed critical island sizes for delamination and the typical values of film stress when this happens.

5.2.2. Axisymmetric analysis

In this section, we consider a circular island on substrate and investigate the criterion for the nucleation and growth of edge delamination under axisymmetric conditions. Following a similar approach adopted in the preceding section, we assume that the intercalation strain is large enough to cause sliding over the entire island. The radius of the island is denoted by R and the edge delamination crack considered here is an annular concentric ring whose front is located at distance a from the edge, as shown in Figure 5.6. In the following, we obtain the radial and tangential components of stresses in the film, at distance r from the center of island.

Consider a circular membrane of radius R_a, subject to a uniform mismatch strain ε^* and uniform radial shear stress τ_0. Deformation of the patch, within plane stress approximation and in the presence of interfacial shear traction as body-force per unit volume of the patch $b = \tau_0 / h$, can be described by the following differential equation

$$\frac{\partial}{\partial r}\left[\frac{1}{r}\frac{\partial}{\partial r}\left(r\,u_r\right)\right] + \frac{b(1-\nu^2)}{E} = 0, \tag{5.11}$$

where u_r is the radial displacement. General solution to the differential Equation (5.11) can be written in the form:

$$u_r = Ar + \frac{B}{r} - \frac{1}{3}\frac{\tau_0(1-\nu^2)}{E\,h}r^2, \tag{5.12}$$

where A and B are constants to be determined from boundary conditions. Radial and hoop stresses in the patch are related to the displacement field via

$$\sigma_{rr} = \frac{E}{1-\nu^2}\left\{\frac{\partial u_r}{\partial r} + \nu\frac{u_r}{r} - (1+\nu)\varepsilon^*\right\}, \tag{5.13}$$

$$\sigma_{\theta\theta} = \frac{E}{1-\nu^2}\left\{\nu\frac{\partial u_r}{\partial r} + \frac{u_r}{r} - (1+\nu)\,\varepsilon^*\right\}. \tag{5.14}$$

Upon satisfying the boundary conditions, $u_r = 0$ at $r = 0$, and $\sigma_{rr} = 0$ at $r = R_a$, the constants A and B are obtained as $A = \varepsilon^* + \frac{1}{3}\frac{\tau_0 R_a(1-\nu)(2+\nu)}{Eh}$, $B = 0$, and subsequently, by setting $R_a = R - a$ the stress components are found as

$$\sigma_{rr} = \frac{(2+\nu)}{3}\frac{\tau_0}{h}\left(R - a - r\right), \tag{5.15}$$

$$\sigma_{\theta\theta} = \frac{1}{3}\frac{\tau_0}{h}\left((2+\nu)(R-a) - (1+2\nu)r\right), \tag{5.16}$$

Figure 5.6: Schematic of (a) a Si circular island on substrate with an annular edge crack and (b) a free-body diagram of the island.

In the analysis presented above, we have neglected the elastic energy stored in the delaminated part of the film, as a thin membrane is susceptible to wrinkling. For the stress field given in Equations (5.15, 5.16), the strain energy density u, within the region $R-a>r>0$, is calculated as

$$u=\frac{\tau_0^2(1-\nu)}{18Eh^2}\left(2(2+\nu)^2(R-a)^2-6(1+\nu)(2+\nu)r(R-a)+(1+\nu)(5+4\nu)r^2\right). \qquad (5.17)$$

The total elastic energy stored in the film is obtained by integrating u over the entire island, i.e. $U_{el}=\int_0^{R-a}2\pi r h u\,dr$, which yields

$$U_{el}=\frac{\pi(1-\nu)(5+\nu)}{36}\frac{\tau_0^2}{Eh}(R-a)^4. \qquad (5.18)$$

The elastic energy release rate is then

$$G=-\frac{dU_{el}}{da}=\frac{\pi(1-\nu)(5+\nu)}{9}\frac{\tau_0^2}{Eh}(R-a)^3. \qquad (5.19)$$

The formation of the annular edge crack causes an increase in surface energy,

$$U_{surf} = \pi\left(R^2 - (R-a)^2\right), \tag{5.20}$$

which grows at a rate of

$$\frac{dU_{surf}}{da} = 2\pi(R-a)\Gamma\,. \tag{5.21}$$

Using Equations (5.19, 5.21), the Griffith condition for crack growth, i.e. $G > dU_{surf}/da$, gives

$$(R-a) > \sqrt{\frac{18E\,h\,\Gamma}{(1-\nu)(5+\nu)\tau_0^2}}\,, \tag{5.22}$$

suggesting that crack nucleation in an initially crack-free interface is favorable only for islands larger than a critical size,

$$R > R_{cr,nuc} = \sqrt{\frac{18E\,h\,\Gamma}{(1-\nu)(5+\nu)\tau_0^2}}\,. \tag{5.23}$$

Similar to Equation (5.8), the crack would arrest when the crack length reaches

$$a_{arr} = R - \sqrt{2R_{cr,nuc}^2 - R^2}\,. \tag{5.24}$$

Note this equation is valid as long as $R < \sqrt{2}R_{cr,nuc}$. For

$$R > R_{cr,del} = \sqrt{2}R_{cr,nuc}\,, \tag{5.25}$$

crack arrest is impossible and the edge crack would grow all the way to the center, leading to complete delamination.

For a 100 nm thick Si circular patch with $E = 40$ GPa and $\nu = 0.22$, $\tau_0 \approx 10$ MPa and $\Gamma = 1$ J/m^2, numerical estimates for the critical island sizes for nucleation and delamination by axisymmetric delamination are $2R_{cr,nuc} = 26.6$ and $2R_{cr,del} = 37.6$ μm, corresponding to maximum radial stresses of 0.98 and 1.39 GPa at the center of the island. Figure 5.7 shows variations of the dimensionless elastic energy release rate and surface energy growth rate as a function of crack size. In this figure, $\tilde{\tilde{U}}_{el} = \dfrac{18hEU_{el}}{\pi(1-\nu)(5+\nu)\tau_0^2 R^4}$ and $\tilde{\tilde{U}}_{surf} = \dfrac{18hEU_{surf}}{\pi(1-\nu)(5+\nu)\tau_0^2 R^4}$ are dimensionless elastic and surface energies, respectively. As shown in this figure, at $a = 0$, corresponding to the case of no preexisting crack, the elastic energy release rate is equal to the rate of increase in surface energy when $R = R_{cr,nuc}$. When $R > R_{cr,nuc}$ ($R < R_{cr,nuc}$), the elastic energy release rate becomes larger (smaller) than the surface energy growth rate at $a = 0$, indicating that crack nucleation is energetically favorable (unfavorable), since it decreases (increases) the total free energy of the system.

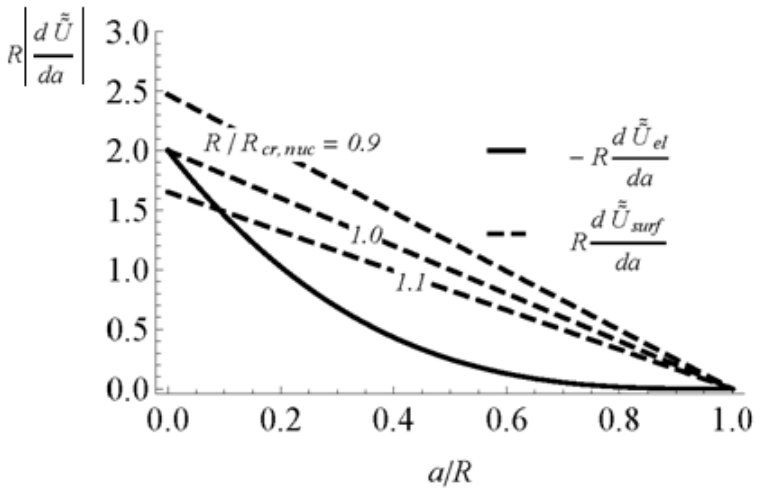

Figure 5.7: Axisymmetric analysis of interfacial delamination of a circular Si island on substrate. Elastic energy release rate and surface energy growth rate *vs*. crack length for various island sizes.

Figure 5.8a plots the dimensionless residual length of the arrested crack, a_{arr}/R, as a function of the dimensionless radius of the island $R/R_{cr,nuc}$. It can be seen from this figure that the length of the arrested crack would reach the radius of the island (i.e. $a_{arr} = R$) when $R = R_{cr,del} = \sqrt{2}R_{cr,nuc}$, corresponding to full delamination. Figure 5.8b plots the changes in dimensionless elastic and surface energies, $\left|\Delta\tilde{\tilde{U}}_{el}\right| = \tilde{\tilde{U}}_{el}(0) - \tilde{\tilde{U}}_{el}(a)$ and $\Delta\tilde{\tilde{U}}_{surf} = \tilde{\tilde{U}}_{surf}(a) - \tilde{\tilde{U}}_{surf}(0)$, for islands of different sizes as a function of the crack length. It indicates that for an island with $R = R_{cr,del} = \sqrt{2}R_{cr,nuc}$, the total released elastic energy is just sufficient to drive the crack all the way to the center. This critical case has been marked by a solid circle in Figure 5.8b. Further discussions are similar to the plane strain analysis.

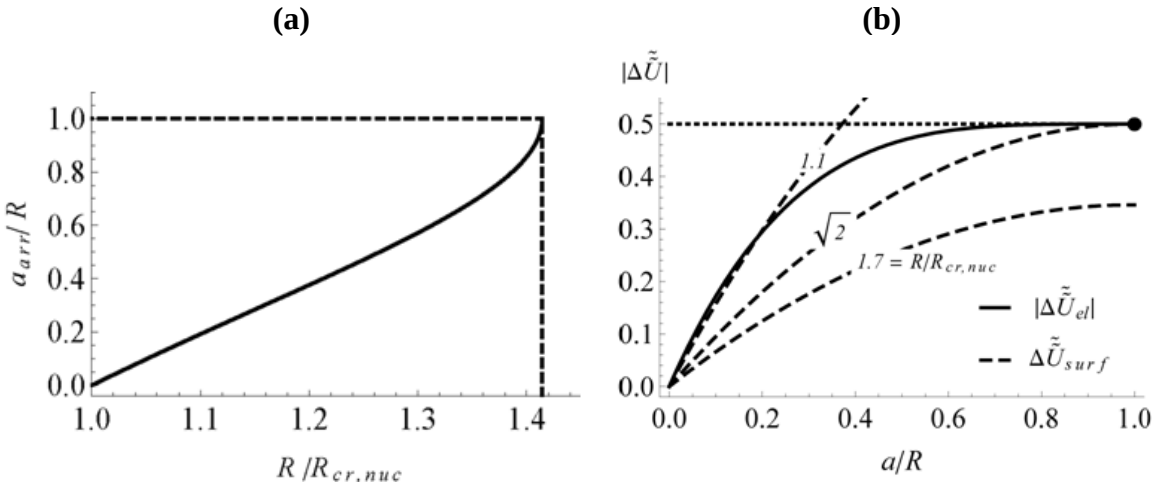

Figure 5.8: Axisymmetric analysis of interfacial delamination of a circular Si island on substrate. (a) Length of the arrested edge crack as a function of the island size; (b) Changes in the elastic energy and surface energy as a function of the crack length for different island sizes.

5.3. Analysis of center delamination cracks in the presence of large scale interfacial sliding

In this section, we consider interfacial cracks at the center of islands using a similar energy approach. Under the same assumptions as stated in Section 5.2, we consider the analysis under plane strain and axisymmetric conditions separately.

5.3.1. Plane strain analysis

Consider the same plane strain problem as in Section 5.2.1, but with an interface crack of length $2a$ located at the center of the island, as shown in Figure 5.9. Under the same assumption of overlapping interfacial sliding zones, the normal stress in the film at distance x from the center of island can be written as

$$\sigma_{xx} = \frac{\tau_0}{h}\begin{cases} l-a & a>x>0 \\ l-x & l>x>a \end{cases}. \tag{5.26}$$

It follows that the total elastic energy in half of the island is

$$U_{el} = \int_0^l \frac{(1-\nu^2)}{2E}\sigma_{xx}^2 dx = \frac{(1-\nu^2)\tau_0^2}{6Eh}(l-a)^2(l+2a), \tag{5.27}$$

and the elastic energy release rate as

$$G = -\frac{dU_{el}}{da} = \frac{(1-\nu^2)\tau_0^2}{hE}a(l-a). \tag{5.28}$$

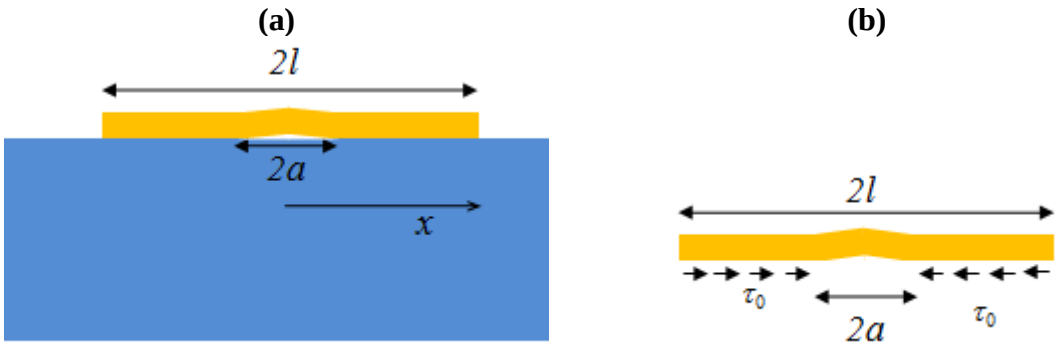

Figure 5.9: Schematic of (a) a Si island on substrate with a center crack an (b) a free-body diagram of the island.

Note that the energy release rate vanishes at $a = 0$, indicating that a preexisting crack is needed for the crack growth condition $G > \Gamma$. This is in contrast to the case of edge delamination where no preexisting cracks are necessary. As shown in the preceding section, even in an initially crack-free island, it is possible for an edge delamination crack to nucleate spontaneously. However, this is not the case for center cracks. To satisfy the

growth condition, the length of the preexisting center crack a_0 should fall in the following range

$$a_{0,max} > a_0 > a_{0,min}, \tag{5.29}$$

where $a_{0,min} = \frac{1}{2} l \left(1 - \sqrt{1 - \frac{4\Gamma E h}{(1-\nu^2)\tau_0^2 l^2}} \right)$, and $a_{0,max} = \frac{1}{2} l \left(1 + \sqrt{1 - \frac{4\Gamma E h}{(1-\nu^2)\tau_0^2 l^2}} \right)$.

The above equation breaks down for

$$\Gamma > \frac{(1-\nu^2) l^2 \tau_0^2}{4 E h}, \text{ or } l < l_{cr}^* = \sqrt{\frac{4 E h \Gamma}{(1-\nu^2)\tau_0^2}}, \tag{5.30}$$

indicating that no center crack can grow, regardless of its length, when the island size is small enough. For the case of $l > l_{cr}^*$, a preexisting crack of length $a_{0,max} > a_0 > a_{0,min}$ will grow. The crack will arrest when

$$U_{el}(a = a_0) - U_{el}(a = a_{arr}) = U_{surf}(a = a_{arr}) - U_{surf}(a = a_0), \tag{5.31}$$

where

$$U_{surf} = \Gamma (a - a_0), \tag{5.32}$$

is the surface energy of the system with respect to the initial state. Equation (5.31) can be solved for a_{arr} to obtain

$$a_{arr} = \frac{1}{4} \left(3l - 2a_0 + \sqrt{9l^2 + 12 a_0 l - 12 a_0^2 - \frac{48 \Gamma E h}{(1-\nu^2)\tau_0^2}} \right). \tag{5.33}$$

By comparing a_{arr} with l, we can determine the condition for complete delamination. Bearing in mind the condition for crack growth, $a_{0,.min} < a_0 < a_{0,max}$, complete delamination $a_{arr} > l$ requires

$$a_{0,min} < a_0 < a_{0,del}, \tag{5.34}$$

where

$$a_{0,del} = \frac{1}{4} l \left(1 + \sqrt{9 - \frac{48 \Gamma E h}{(1-\nu^2)\tau_0^2 l^2}} \right). \tag{5.35}$$

This equation breaks down for

$$\Gamma > \frac{3(1-\nu^2) l^2 \tau_0^2}{16 E h}, \text{ or } l < l^*_{cr,del} = \frac{2}{\sqrt{3}} l^*_{cr} = \sqrt{\frac{16 E h \Gamma}{3(1-\nu^2)\tau_0^2}}, \tag{5.36}$$

indicating that full delamination is impossible for sufficiently small islands. As expected, Equation (5.30), which inhibits any crack growth, gives a stronger condition than Equation (5.36), which allows growth but prevents full delamination. Figure 5.10a shows variations of the dimensionless elastic energy release rate as a function of the dimensionless crack length. As shown in this figure, the elastic energy release rate falls entirely below the rate at which the surface energy of the system increases for $l < l^*_{cr}$. However, for $l > l^*_{cr}$, these two curves intersect each other at two points corresponding to $a_{0,min}$ and $a_{0,max}$. The total elastic energy, the total surface energy, and their changing rate as a function of crack length are shown for various island sizes in Figures 5.10b-

5.10d. In each of these figures, the surface energy curve has been plotted for two different preexisting crack lengths $a_0 = a_{0,min}$, and $a_0 = 0.5l$. As shown in Figure 5.10b for $l = 1.1l_{cr}^* < l_{cr,del}^*$, neither of these two preexisting cracks can grow all the way to the edge, as the elastic energy in the patch is not sufficient to drive full delamination, i.e. $U_{el}(a = a_0) - U_{el}(a = l) < U_{surf}(a = l) - U_{surf}(a = a_0)$. This is consistent with the critical condition for complete delamination given by Equation (5.36). In the critical case of $l = \frac{2}{\sqrt{3}} l_{cr}^* = l_{cr,del}^*$, shown on Figure 5.10c, a preexisting crack with $a_0 = a_{0,min} = 0.25l$ can grow all the way to the edge leading to complete delamination, as Equation (5.31) is satisfied. In comparison, a preexisting crack with $a_0 = 0.5l$ is arrested when $U_{el}(a = a_0) - U_{el}(a = l) < U_{surf}(a = l) - U_{surf}(a = a_0)$. Figure 5.10d shows the case of $l = 1.5l_{cr}^* > l_{cr,del}^*$, in which both of the preexisting cracks considered here grow all the way to the edge, leading to full delamination, as they satisfy $U_{el}(a = a_0) - U_{el}(a = l) > U_{surf}(a = l) - U_{surf}(a = a_0)$.

(a)

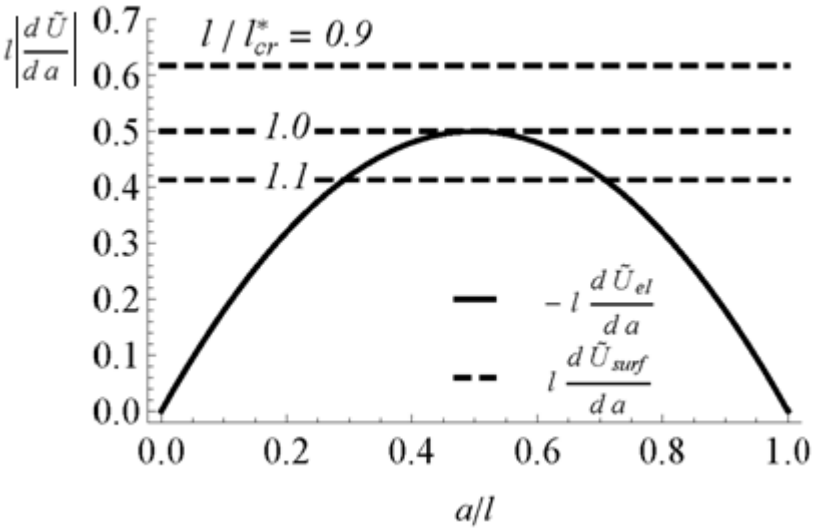
$l\left|\frac{d\tilde{U}}{da}\right|$
$l / l^*_{cr} = 0.9$
1.0
1.1
$-l\frac{d\tilde{U}_{el}}{da}$
$l\frac{d\tilde{U}_{surf}}{da}$
0.0
0.1
0.2
0.3
0.4
0.5
0.6
0.7
0.0
0.2
0.4
0.6
0.8
1.0
a/l

(b)

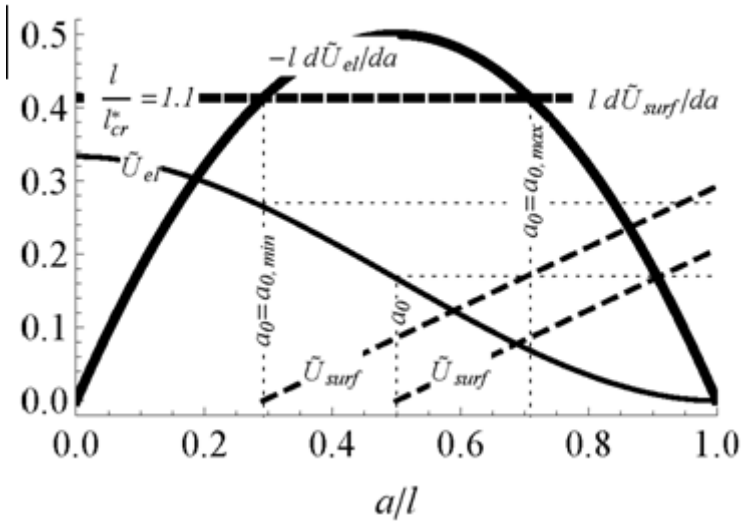
$\frac{l}{l^*_{cr}} = 1.1$
$-l\,d\tilde{U}_{el}/da$
$l\,d\tilde{U}_{surf}/da$
$\tilde{U}_{el}$
$a_0 = a_{0,min}$
a_0
$a_0 = a_{0,max}$
$\tilde{U}_{surf}$
$\tilde{U}_{surf}$
0.0
0.1
0.2
0.3
0.4
0.5
0.0
0.2
0.4
0.6
0.8
1.0
a/l

(c)

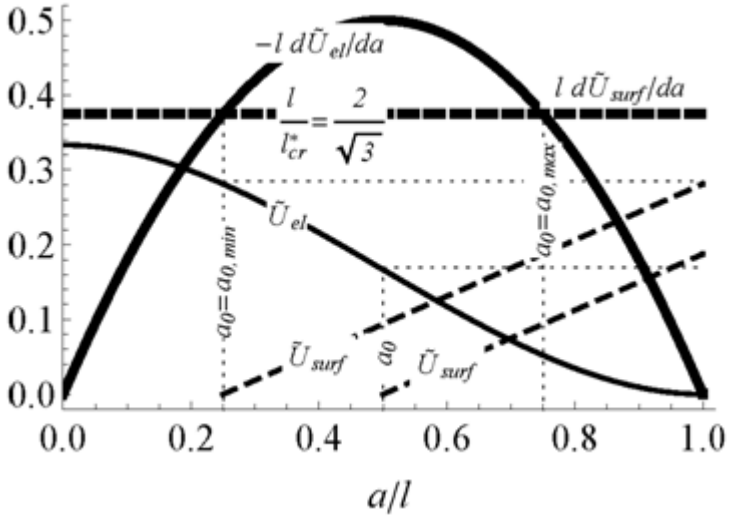
0.5
0.4
0.3
0.2
0.1
0.0
0.0
0.2
0.4
0.6
0.8
1.0
a/l
$-l\, d\tilde{U}_{el}/da$
$l\, d\tilde{U}_{surf}/da$
$\frac{l}{l^*_{cr}} = \frac{2}{\sqrt{3}}$
$\tilde{U}_{el}$
$a_0 = a_{0,min}$
$a_0 = a_{0,max}$
$\tilde{U}_{surf}$
a_0
$\tilde{U}_{surf}$

(d)

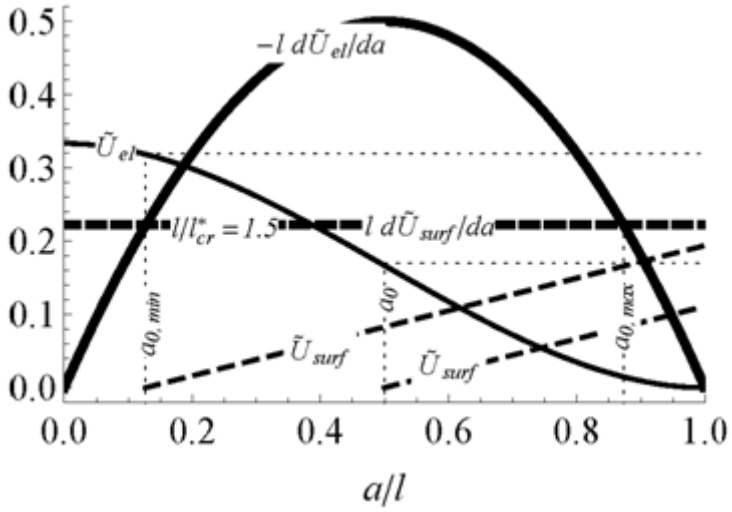
0.5
0.4
0.3
0.2
0.1
0.0
0.0
0.2
0.4
0.6
0.8
1.0
a/l
$-l\, d\tilde{U}_{el}/da$
$\tilde{U}_{el}$
$l/l^*_{cr} = 1.5$
$l\, d\tilde{U}_{surf}/da$
$a_{0,min}$
a_0
$a_{0,max}$
$\tilde{U}_{surf}$
$\tilde{U}_{surf}$

(e)

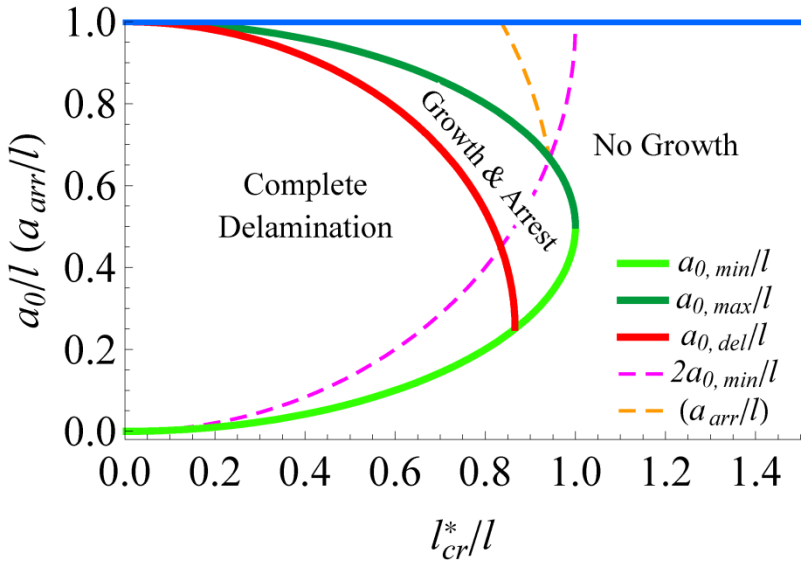

Figure 5.10: Plane strain analysis of interfacial delamination of a Si island on substrate with a center crack at the interface: (a) Elastic energy release rate and surface energy growth rate *vs*. crack length for various island sizes; Total elastic energy of the island, total surface energy of the system and their changing rates associated with crack growth for (b) $l/l^*_{cr} = 1.1$, (c) $l/l^*_{cr} = 2/\sqrt{3}$, (d) $l/l^*_{cr} = 1.5$; (e) Phase diagram indicating whether a preexisting crack will grow or not, and if so whether it will lead to full delamination, for given crack length and island size.

A summary of the analysis presented above can be cast in a phase-diagram shown in Figure 5.10e. In this figure, the horizontal axis is a measure of the island size or interface toughness, and the vertical axis shows the length of the preexisting crack. Three regions have been indicated on this figure, which are separated by solid curves. Given the dimensionless length of the preexisting crack a_0/l and the dimensionless size of the island l^*_{cr}/l, the phase diagram indicates whether the crack can grow or not, and if it can, whether it will be arrested. The dashed curve labeled as "$2a_{0,min}/l$" provides an example of the case of $a_0 = 2a_{0,min}$. As shown in the figure, this curve goes through all

three regions. For the segment of this curve which falls in the "Growth & Arrest" region, the length of the arrested crack has been shown by the dashed curve labeled as " $(\frac{a_{arr}}{l})$", which can be read out from the vertical axis for a given $\frac{l_{cr}^*}{l}$.

For 100 nm thick Si islands with $E = 40$ GPa and $\nu = 0.22$, $\tau_0 \approx 10$ MPa, and $\Gamma = 1$ J/m^2, the critical island sizes $2l_{cr}^*$ and $2l_{cr,del}^*$ are estimated to be 25.94 μm and 29.94 μm, respectively. The minimum length of the required pre-existing cracks for full delamination, and the corresponding maximum stresses in the film prior to crack growth, are given for different island sizes in Table 5.1. It should be noted that while the maximum stresses given in this table exceed the apparent flow stress observed in Si thin films (1-1.7 GPa)[16, 17], our assumption of overlapping interfacial sliding in the island is not necessarily violated. This is because the latter is, in fact, an *averaged* flow stress while the actual stress distribution in the film is not uniform.

Table 5.1. Numerical estimates of the minimum length of the pre-existing crack required for full delamination for different island sizes based on the plane strain analysis.

	$l/l_{cr,del}^*$	1	1.34	1.67	2
Island size	$2l$ (μm)	29.95	40	50	60
	$a_{0,min}$ (μm)	3.74	2.39	1.81	1.47
Max. stress	σ_{max} (GPa)	1.12	1.76	2.32	2.85

5.3.2. Axisymmetric analysis

In this section, we consider a central penny-shaped interfacial crack of radius a, as shown in Figure 5.11. Invoking the same assumption of overlapping interfacial sliding zones as in the foregoing section, stress components in the film can be obtained as in the following. Consider a membrane of radius R, subject to a uniform shear stress τ_0 within the region $R > r > a$ and zero shear stress within $a > r > 0$. In this case, the body-force in Equation (5.11) should be replaced by

$$b = \begin{cases} 0 & a > r > 0 \\ \dfrac{\tau_0}{h} & R > r > a \end{cases}. \tag{5.37}$$

This equation can be solved within $R > r > 0$ to give

$$u_r = \begin{cases} A_1 r + \dfrac{B_1}{r} & a > r > 0 \\ A_2 r + \dfrac{B_2}{r} - \dfrac{1}{3}\dfrac{\tau_0(1-\nu^2)}{E\,h} r^2 & R > r > a \end{cases}, \tag{5.38}$$

where A_1, A_2, B_1 and B_2 are constants to be determined from boundary conditions

$u_r = 0$ at $r = 0$, and $\sigma_{rr} = 0$ at $r = R_a$, and continuity conditions of the displacement as well as the radial stress at $r = a$. This yields

$$A_1 = \varepsilon^* - \frac{1}{6}\frac{\tau_0(1-\nu)}{E\,h}\left(2R^3(2+\nu) - 3aR^2(1+\nu) - a^3(1-\nu)\right),\ A_2 = A_1 + \frac{\tau_0 a(1-\nu^2)}{2Eh},$$

$B_1 = 0$ and $B_2 = \dfrac{-\tau_0 a^3(1-\nu^2)}{6Eh}$. Upon substitution of these constants in Equation (5.38), the radial and hoop stresses can be obtained from Equations (5.13, 5.14), as

$$\sigma_{rr} = \frac{\tau_0}{6hR^2}\begin{cases} 2(2+\nu)R^3 - 3(1+\nu)R^2 a - a^3(1-\nu) & a > r > 0 \\ (R-r)\left(2(2+\nu)R^2 + (1-\nu)\dfrac{a^3}{r^2}(R+r)\right) & R > r > a \end{cases}, \tag{5.39}$$

$$\sigma_{\theta\theta} = \frac{\tau_0}{6hR^2}\begin{cases} 2(2+\nu)R^3 - 3(1+\nu)R^2 a - a^3(1-\nu) & a > r > 0 \\ 2(2+\nu)R^3 - 2(1+2\nu)rR^2 - (1-\nu)\dfrac{a^3}{r^2}(R^2+r^2) & R > r > a \end{cases}. \tag{5.40}$$

The total elastic energy of the patch can thus be calculated as

$$U_{el} = \frac{\pi(1-\nu)\tau_0^2}{36EhR^2}\left((5+\nu)R^6 - 8(2+\nu)R^3a^3 + 9(1+\nu)R^2a^4 + 2(1-\nu)a^6\right). \tag{5.41}$$

The elastic energy release rate is then

$$G = -\frac{dU_{el}}{da} = \frac{\pi(1-\nu)\tau_0^2}{3EhR^2}a^2\left(2R^3(2+\nu) - 3(1+\nu)R^2a - (1-\nu)a^3\right). \tag{5.42}$$

During crack growth, the surface energy associated with the crack,

$$U_{surf} = \pi(a^2 - a_0^2)\Gamma, \tag{5.43}$$

would grow at a rate of

$$\frac{dU_{surf}}{da} = 2\pi a\Gamma. \tag{5.44}$$

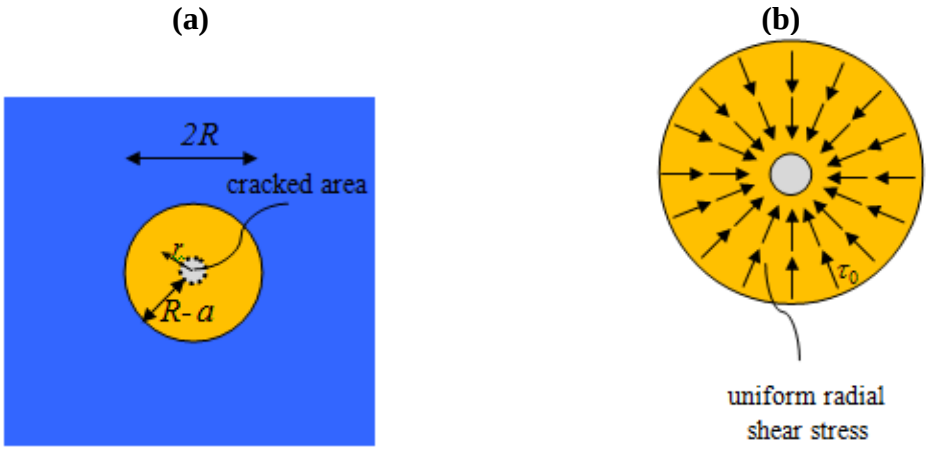

Figure 5.11: Schematic of (a) a circular Si island on substrate with a penny-shaped center crack and (b) a free-body diagram of the island.

While the elastic energy release rate and its first derivative with respect to the crack length vanish at $a = 0$, dU_{surf}/da vanishes at $a = 0$ but has a finite positive derivative with respect to a. Therefore $G < dU_{surf}/da$ in the vicinity of $a = 0$, and similar to the plane strain case, cracking at the center is impossible without a preexisting crack. While essential features of this problem remain similar to the plane strain analysis presented before, the algebraic calculations become rather complicated since the elastic energy is a sixth order polynomial with respect to the crack length. The details of the analysis are skipped here and the emphasis is directed at the main findings. Similar to the plane strain case, we can identify two critical length scales R_{cr}^*, and $R_{cr,del}^*$. If the island radius falls below R_{cr}^*, no preexisting circular crack can grow, regardless of its radius, while if the island radius falls below $R_{cr,del}^*$, no preexisting crack can lead to complete delamination. These length scales as a function of the Poisson's ratio of the island are shown in Figure

5.12a. For 100 nm thick Si islands with $E = 40$ GPa and $\nu = 0.22$, $\tau_0 \approx 10$ MPa, and $\Gamma = 1$ J/m^2, numerical estimates for the critical island sizes are $2R^*_{cr} \approx 31.2$ μm and $2R^*_{cr,del} \approx 37.6$ μm. The minimum length of the center cracks which leads to complete delamination, and the corresponding maximum stresses for different island sizes, are given in Table 5.2. A summary of the detailed analysis is presented in Figure 5.12b, in the form of a phase diagram similar to the one presented for the plane strain case, for the case $\nu = 0.25$.

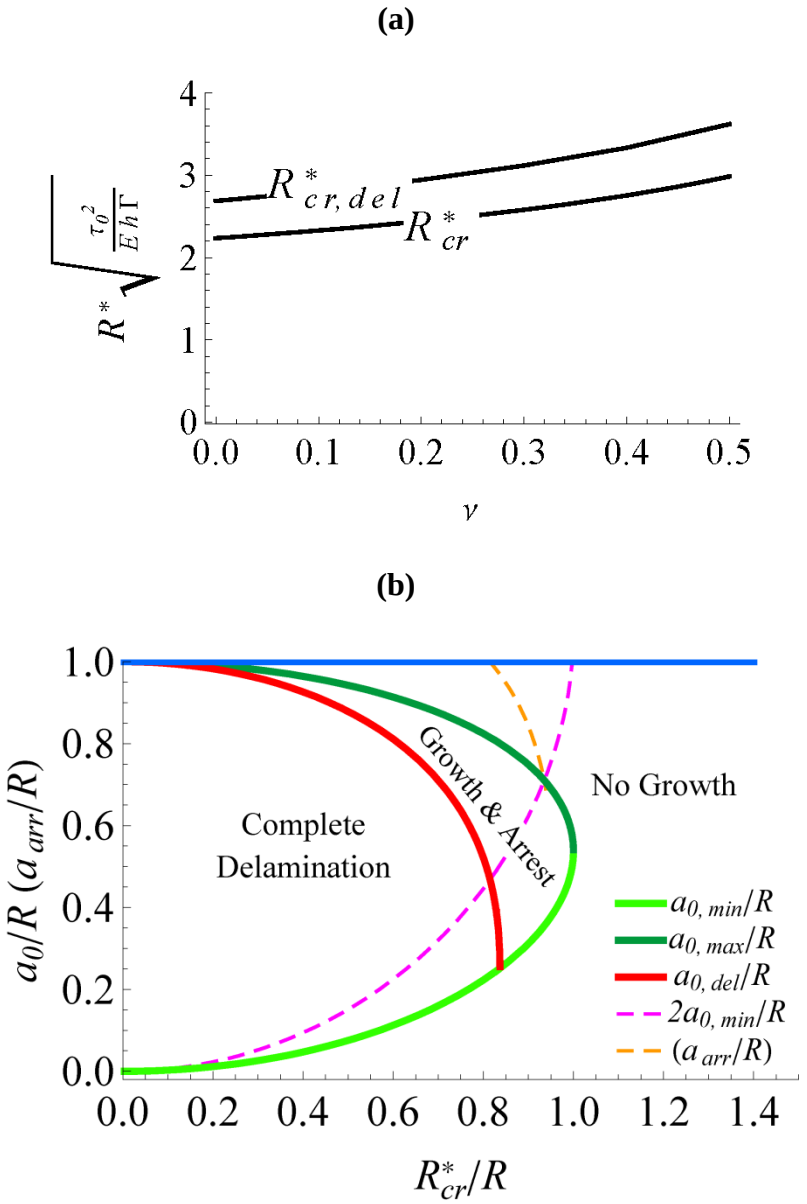

Figure 5.12: Axisymmetric analysis of interfacial delamination of a circular island on substrate. (a) Critical length scales as a function of the Poisson's ratio of the island; (b) Phase diagram in terms of preexisting crack length and island size.

Table 5.2. Numerical estimates of the minimum length of the pre-existing crack required for full delamination for circular islands of different sizes.

	$R / R^{*}_{cr,del}$	1	1.06	2.12	3.19
Island size	$2R$ (μm)	37.64	40	60	80
	$a_{0,min}$ (μm)	4.63	4.20	2.48	1.80
Max. stress	σ_{max} (GPa)	1.11	1.22	2.06	2.85

5.4. Summary

In summary, we have proposed a method to deduce the critical size for interfacial delamination of patterned thin film electrodes on substrate in the presence of large scale interfacial sliding. We have investigated the critical conditions of interfacial delamination with plane strain and axisymmetric analysis of both edge and center delamination cracks at the interface between thin film islands and the substrate. Our analysis shows that the overlapping interfacial sliding zones due to the finite interfacial sliding strength lead to a new class of size effects in interfacial delamination. Interfacial delamination of the electrodes becomes impossible when the island size falls below a critical length scale. Applications to lithiation of thin-film Si islands give results in excellent agreement with the experimentally observed size effects. The present work provides insights for optimized structural design to mitigate the mechanical degradation in high-capacity electrodes.

Chapter 6

Ratcheting of Si island electrodes on substrate due to cyclic intercalation

In the previous chapters, we have discussed some consequences of plastic deformation within patterned Si thin films and sliding along the interface between the islands and the substrate, in the context of delamination of such patterned islands as well as stress measurements in such electrodes. In the present chapter, we propose a plastic ratcheting mechanism in Si islands on substrate, which is activated as soon as the island size becomes large enough to allow for plastic deformation and there exist differences between the yield stress and/or interfacial sliding strength during lithiation and delithiation half-cycles. In the past, ratcheting has been studied as a low-cycle fatigue failure mode in a variety of materials and structures subject to cyclic thermal and/or mechanical loadings, such as pressure vessels [151], fiber-reinforced composites [152], thin multilayers on substrate [153], and interconnect structures [154]. In a typical ratcheting response under cyclic loads, plastic strain accumulates in a structure with each loading cycle, leading to localized failure after a finite number of cycles. It is thus crucial to avoid ratcheting in order to ensure structural stability under cyclic plasticity [155].

As it was discussed earlier in Chapter 4, in the presence of interfacial sliding, there exists a characteristic length scale for Si islands,

$$2l_{cr} = \frac{2\sigma_y h}{\tau_0}, \tag{6.1}$$

where σ_y is the flow stress of Si, τ_0 is the shear resistance of the sliding interface and h is the island's thickness (see Figure 6.1). In order for an island to remain elastic, the island size must stay below this characteristic size, i.e. $l < l_{cr}$, and plastic deformation occurs only in Si islands larger than the critical size given by Equation (6.1). In the following, we show that ratcheting in these islands would occur as soon as one recognizes the fact that the plastic yield stress of Si and/or the interfacial sliding strength can take different values during lithiation and delithiation half-cycles [156]. While experiments have already demonstrated that the yield stress of Si can differ by as much as 50% during lithiation and delithiation [16], the interfacial sliding strength could also vary from lithiation to delithiation. We show below that ratcheting would occur as soon as these variations in yield/sliding strength are recognized.

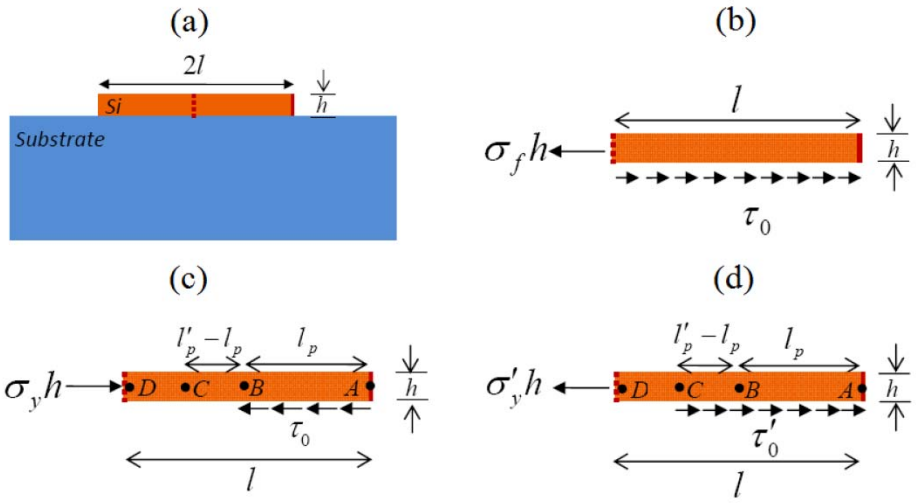

Figure 6.1: Schematic of a Si island on substrate under cyclic lithiation and delithiation. (a) Geometry of the entire system and (b) the free-body diagram of half of the island. Free-body diagrams at the end of (c) intercalation half-cycles and (d) deintercalation half-cycles.

Consider an array of Si islands adhering on a substrate. Taking advantage of the symmetry and periodicity of the problem, only half of a single island needs to be considered in the analysis. A shear cohesive zone model is adopted to describe the interfacial sliding of the Si islands on the substrate surface. Within the cohesive zone, the shear traction is related to interfacial sliding according to a rigid-perfectly plastic law with a strength of τ_{th}, i.e. interfacial sliding is not allowed wherever the interfacial shear stress falls below τ_{th} but sliding occurs freely once τ_{th} is reached. The value of τ_{th} is set to τ_0 during lithiation half-cycles and to τ_0' during delithiation half-cycles. Figure 6.2 shows the cohesive law relating the interfacial shear traction τ and sliding displacement u. During the lithiation half-cycles, interfacial sliding occurs freely as soon as the

threshold stress τ_0 is reached. Subsequent unloading during the delithiation half cycles would first reduce the shear traction without further sliding, until the delithiated threshold stress τ_0' is reached, at which point sliding would again occur freely in the reverse direction. Similarly, the yield stress of the island is set to σ_y during lithiation half-cycles and to σ_y' during delithiation half-cycles.

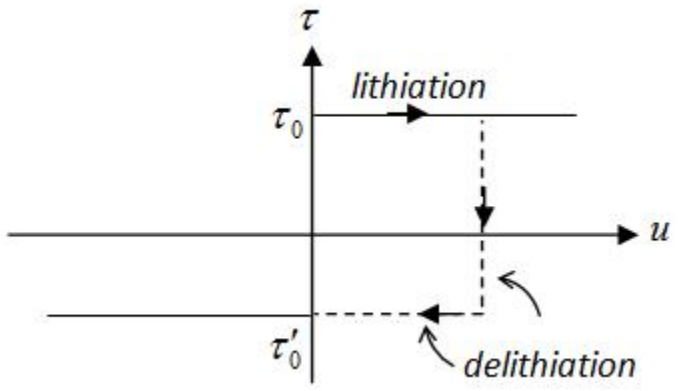

Figure 6.2: The rigid-perfectly plastic cohesive law used for modeling the interfacial sliding with differential sliding resistance during lithiation and delithiation half cycles. Here, τ_0 denotes the interfacial sliding strength during the lithiation half-cycle and τ_0' denotes the sliding strength during the delithiation half-cycle.

In general, the cyclic plastic deformation of Si islands under intercalation strain ε^* should depend on the ratios $\varepsilon^*/\varepsilon_y$ and $\varepsilon^*/\varepsilon_y'$ where $(\varepsilon_y, \varepsilon_y') = (\sigma_y, \sigma_y')/E$ (E being the Young's modulus) is the elastic strain of the island at yielding. However, knowing that the overall intercalation strain in Li-ion battery is associated with up to 400% volume expansion, while the elastic yield strain should be less than 1-2%, we will assume $\varepsilon^* >> \varepsilon_y$ and $\varepsilon^* >> \varepsilon_y'$ in the following analysis. Referring to Figures 6.1c,d,

during the cycling, the island would flow at points "B" and "C" at distances $l_p = \sigma_y h / \tau_0$ (lithiation) and $l'_p = \sigma'_y h / \tau'_0$ (delithiation) from the edge of the island, respectively. For the convenience of analysis and without loss of generality, we assume that $l'_p > l_p$. Stress within the region "AB" can never reach the yield stress of Si (as shown in Figures 6.1c,d). Therefore, there is no net change in length of "AB" in a full cycle, as its deformation is entirely elastic. Furthermore, since the axial stress within the region "CD" is uniform, the shear stress at the interface underneath this region must remain zero during cycling. Therefore, interfacial sliding is impossible within "CD", and length of this region cannot change during cycling. To determine the change in length of the island within the region "BC", consider the island at the end of a deintercalation half-cycle at which point the island has already yielded within the region "CD", as shown in Figure 6.1d. During the subsequent half-cycle, the interfacial shear stress in the region "BC" will decrease from τ'_0 to zero (see Figure 6.1c), and, according to the irreversible cohesive response discussed above, no sliding could occur along the interface underneath this region. Hence, the length of "BC" remains unchanged during this half-cycle. In the subsequent deintercalation half-cycle, deformation within the region "BC" is entirely elastic, as this region does not yield in tension (see Figure 6.1d). During this half-cycle, change in the elastic strain within "BC" is given by $\varepsilon_y + \varepsilon'_y x / l'_p$, where x is the distance from the edge of the patch. Therefore, the length of "BC" would change by $\int_{l_p}^{l'_p} (\varepsilon_y + \varepsilon'_y x / l'_p - \varepsilon^*)\, dx$. This integral can be approximated as $(\varepsilon_y + \varepsilon'_y - \varepsilon^*)(l'_p - l_p)$ for $(l'_p - l_p)/l'_p << 1$. The above analysis shows that, as the island goes through one full

cycle (excluding the first cycle), the length of "BC" changes by $(\varepsilon^* - \varepsilon_y - \varepsilon'_y)(l_p - l'_p)$. Noting that $\varepsilon^* >> \varepsilon_y + \varepsilon'_y$, a net compressive (tensile) strain would be accumulated per each cycle, under the condition $l_p < l'_p$ ($l_p > l'_p$), leading to compressive (tensile) ratcheting failure of the island. This net accumulation of deformation leads to severe plastic localization, and could be followed by failure and fracture after a limited number of cycles.

In order to demonstrate the validity of the above calculations and illustrate how this phenomenon leads to localized deformation, we have also performed finite element (FEM) simulations for the model system of a periodic array of 4 μm long, 50 nm thick silicon islands on a rigid substrate, subject to a cyclic misfit strain of 10 %. The yield stress and Young's modulus of Si were taken as $\sigma_y = \sigma'_y =$ 900 MPa and $E = 40$ GPa, and the interfacial shear strengths during lithiation/delithiation as $\tau_0 = 35$ MPa and $\tau'_0 = 25$ MPa, respectively. With these parameter values, according to Equation (6.1), a 4 μm long island would be large enough to induce plastic deformation and compressive ratcheting in the Si islands. Figures 6.3a and 6.3b show deformation of a periodic array of islands, after one and ten cycles, respectively. The results clearly demonstrate accumulation of compressive strain in the islands during cycling, which leads to contraction of the islands in the lateral direction, and hence, widening of the gap between them. Deformation within half of a single island is shown in Figure 6.4 after 1, 2, 5 and 10 cycles.

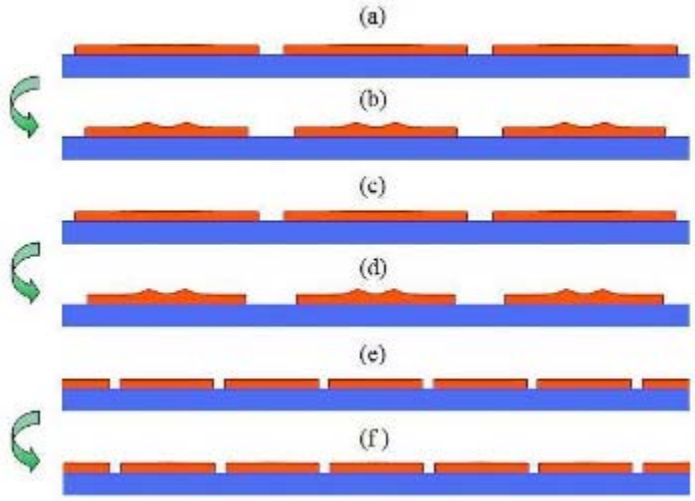

Figure 6.3: Finite element simulations of deformation in a periodic array of islands. Ratcheting of the islands after (a) 1 cycle and (b) 10 cycles with differential sliding resistance and $l > l_{cr}$. Ratcheting of the islands after (c) 1 and (d) 10 cycles with differential yield stress for Si and $l > l_{cr}$. Elastic reversible response of an array of islands with $l < l_{cr}$ after (e) 1 cycle and (f) 10 cycles. The thickness direction has been magnified by a factor of 4.

A similar ratcheting phenomenon also emerges from a mismatch between the yield stress of Si in compression and tension, if one adopts a lower yield stress for Si in compression as compared to tension. Figures 6.3c and 6.3d show deformation obtained by FEM simulations for the same system mentioned above after one and ten cycles, respectively, when the yield stress of Si is allowed to vary from $\sigma_y' = 900$ MPa during delithiation to $\sigma_y = 650$ MPa during lithiation, while the interfacial sliding strength is fixed at $\tau_0 = \tau_0' = 25$ MPa. The FEM simulations show a rate of strain accumulation within 10% of our analytical predictions mentioned above. This comparison is given in

Figure 6.5, where solid lines are obtained from the theoretical results and dots are from the FEM simulations.

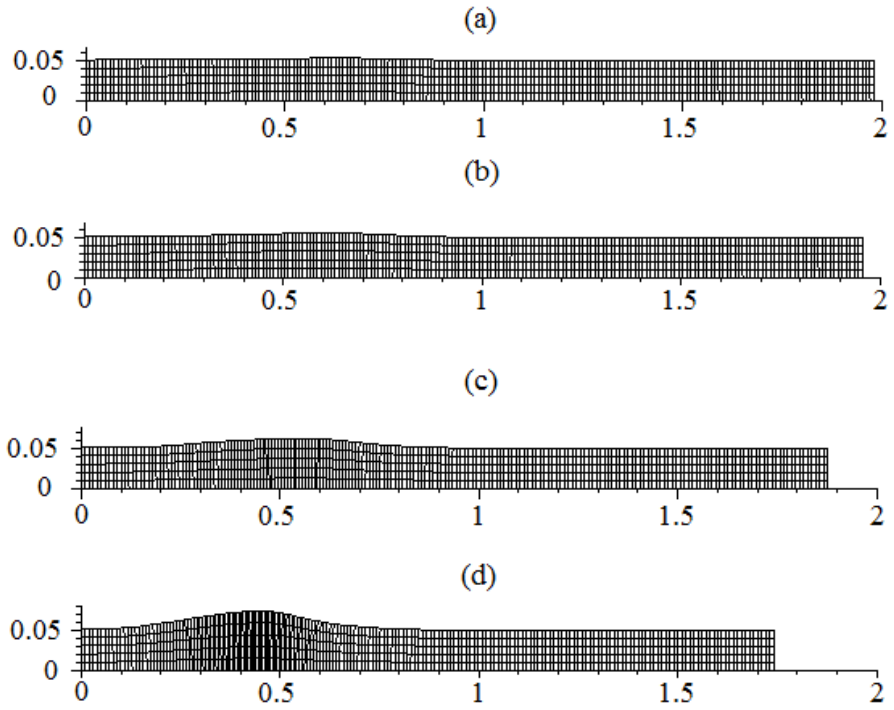

Figure 6.4: Deformation within half of a single island, after (a) 1, (b) 2, (c) 5, and (d) 10 cycles with differential sliding resistance and $l > l_{cr}$ The thickness direction has been magnified by a factor of 2. The figure shows incremental accumulation of compressive deformation with cycling.

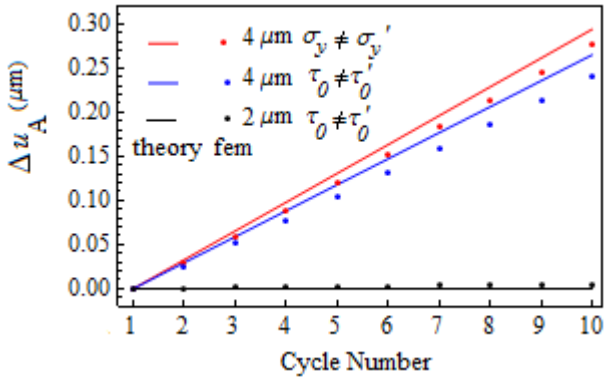

Figure 6.5: Displacement of the edge of the island (point A in Figure 6.1), in absolute value, vs. the number of cycles. Comparison of the theoretical predictions with the FEM calculations.

The above analysis shows that, in the presence of plastic deformation, any non-proportional change in the flow stress of Si and/or sliding resistance of the interface from half-cycle to half-cycle would activate ratcheting. The same analysis also indicates that ratcheting can be suppressed simply by reducing the lateral size of the islands below the critical length scale given by Equation (6.1). To confirm this size effect, Figures 6.3e and 6.3f show deformation in a periodic array of 2 μm long and 50 nm thick islands after one and ten cycles, respectively. The results show fully reversible deformation during cycling, where $\sigma_y = \sigma_y' =$ 900 MPa, $\tau_0 = 35$ MPa and $\tau_0' = 25$ MPa. Indeed, with the chosen parameters, according to Equation (6.1), 2 μm long islands are below the minimum critical size required for plastic deformation in the islands, and therefore not subject to the ratcheting instability.

Existing experiments also suggest ratcheting as an active failure modes in Si thin film electrodes [15]. Figure 6.6a shows plan view of a 250 nm thick Si film on Cu substrate which has fractured into islands after one cycle at the cycling rate of C/2.5. Figure 6.6b shows the same fracture pattern after 30 cycles [15]. Note that the gap between the fractured islands increases upon cycling. On the other hand, the edges of most islands seem to match, suggesting that the broadening gaps between the islands are not likely due to film delamination from the substrate. Comparing our FEM simulations in Figure 6.3 and the experiments in Figure 6.6 indicates that compressive ratcheting may have caused individual islands to contract in lateral dimensions, leading to widened gaps between them. Another observation from Figure 6.6 is that the surface roughness of the islands has increased during cycling from Figure 6.6a to 6.6b. This is also consistent with the mechanism proposed here, as our numerical simulations show that compressive ratcheting would manifest itself through localized thickening of the film, leading to formation of rougher surfaces (see Figures 6.3b, 6.3d).

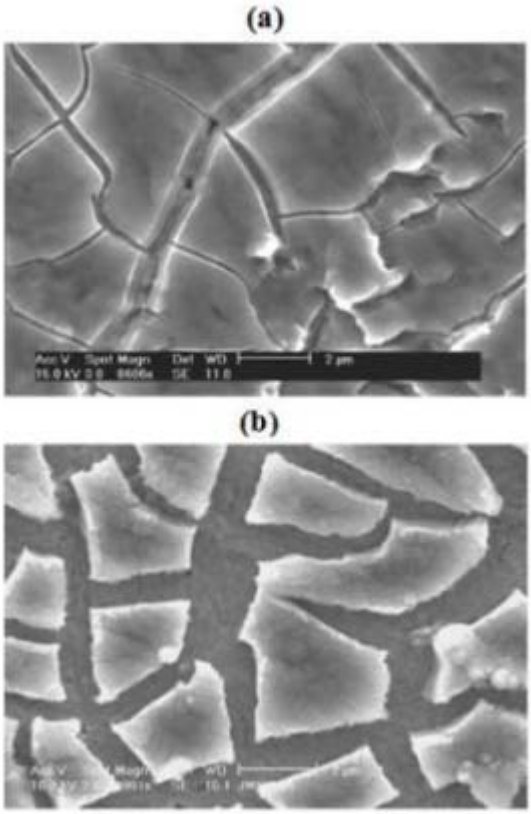

Figure 6.6: Plan view of a 250 nm thick Si continuous film cycled at C/2.5 rate. (a) Film has fractured after 1 cycle. (b) The gap between the islands has substantially widened after 30 cycles. The matching edges and roughened surface of the islands suggest that the lateral dimensions of the islands have shrunk. The scale bars correspond to 2 μm of the actual dimensions. (Reprinted with permission from Ref. [15]. Copyright 2006, The Electrochemical Society).

While our study suggests that the lateral contraction of Si islands parallel to the substrate could lead to cyclic plastic failure, it should not be interpreted as contradictory to experimental observations that most of the volume change during cycling of thin film electrodes occurs in the thickness direction [157]. Even a small amount of lateral sliding along the interface could activate the ratcheting mechanism and, since the process is accumulative, could lead to severe strain localization and failure after a sufficient number

of cycles. Also, recent experiments have clearly revealed that lateral dimensions of the Si islands on substrate do change during lithiation/delithiation half-cycles [135].

The above results showed possibility of compressive ratcheting within the islands. However, it is also possible that the mismatch between the ratio of the yield stress and interfacial resistance in intercalation and deintercalation half-cycles leads to a tensile ratcheting. This is shown in Figure 6.7, where the yield stress varies from $\sigma_y' = 650$ MPa during delithiation to $\sigma_y = 900$ MPa during lithiation, while the interfacial sliding strength is fixed at $\tau_0 = \tau_0' = 25$ MPa.

In summary, we have performed theoretical analysis and numerical simulations of a ratcheting failure mechanism in Si islands induced by differential yield stress and/or interfacial sliding resistance during lithiation and delithiation half-cycles. This form of cyclic plasticity results in an accumulation of plastic strain with each charging cycle and could cause rapid capacity fading in Si electrodes on current collectors. Our analysis suggests a simple solution to the problem by reducing the size of the islands below the minimum critical length scale required for initiation of the plastic yielding in the island,

$$l_{cr} = \min\left(\frac{\sigma_y h}{\tau_0}, \frac{\sigma_y' h}{\tau_0'}\right).$$

The above condition prevents plastic deformation and ratcheting from occurring in the electrodes.

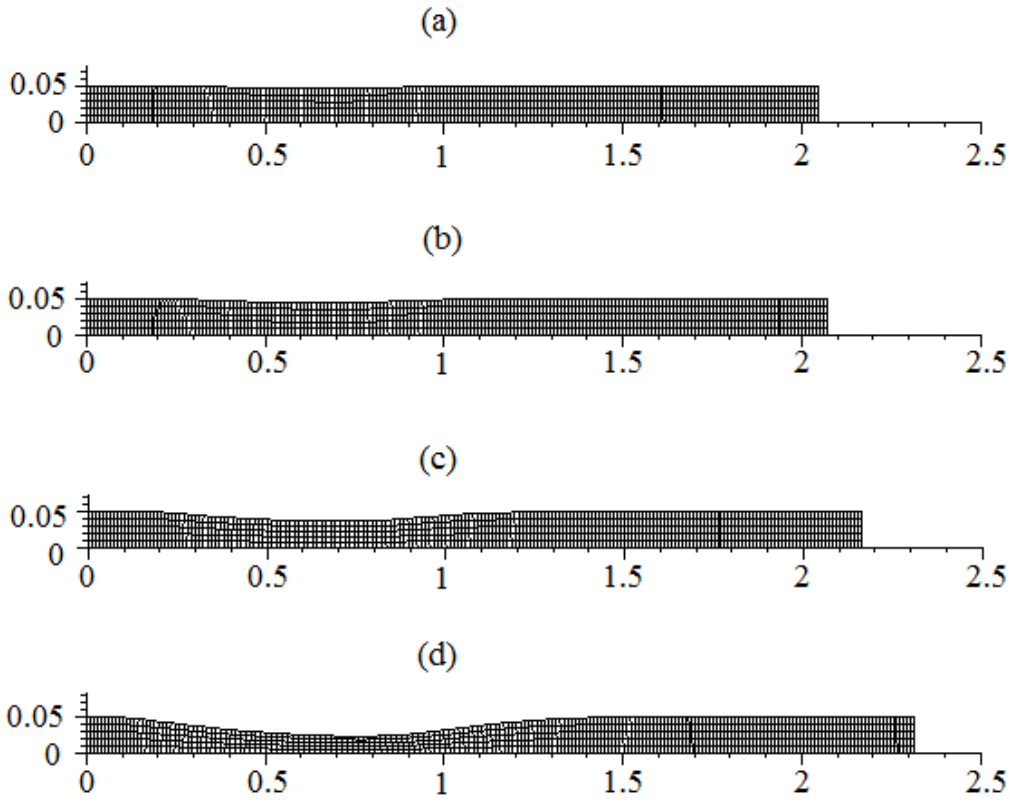

Figure 6.7: Tensile ratcheting deformation within half of a single island, after (a) 1, (b) 2, (c) 5, and (d) 10 cycles with differential sliding resistance and $l > l_{cr}$ The thickness direction has been magnified by a factor of 2. The figure shows incremental accumulation of tensile deformation.

Chapter 7

Concluding Remarks

This last chapter is aimed to present a summary of main results of this thesis on a chapter-to-chapter basis. This summary includes some discussions on the main limitations of the present work as well as possible research directions for the future.

7.1. Summary of the results

7.1.1. Chapter 2

- A continuum model for predicting evolution of the concentration profile in an infinitely long free-standing plate was discussed.
- It was shown that the diffusion-induced stresses could significantly alter the diffusivity, and hence, the diffusion process.
- Effect of binding energy and existence of a maximum stoichiometric limit on the evolution of the concentration profile was also discussed.
- The continuum model was tested against atomistic simulations of hydrogen in nickel. The model was proved capable of predicting the concentration profiles within the host.

7.1.2. Chapter 3

- A particular specialization of the continuum model developed in Chapter 1 was used to study the effect of coupling between the diffusion-induced stresses and the diffusivity coefficient.

- It was shown that the coupling introduced in the model gives rise to a self-limiting behavior, or surface locking, in which the added ions instead of diffusing inside the particle, jam on the surface.
- A similar self-limiting phenomenon has been widely reported in the literature with regard to thermal oxidation of silicon, based on continuum modeling [158-161], atomistic simulations[162, 163] and experimental findings [164-166], where most of the arguments revolve around stress-retardation effect.

7.1.3. Chapter 4

- Crack spacing in thin film silicon electrodes on substrate was discussed in terms of coexistence of plastic deformation within Si film, and interfacial sliding and/or plastic deformation within the substrate. It was shown that the ratio between the estimate of ~ 40 MPa for the shear stresses along the interface and the yield stress of lithiated silicon ~1-1.7 GPa can explain the remarkable difference between the observed crack spacing of ~5-10 μm, and the film thickness of 100 nm.
- It was shown that the interface-limited behavior could allow for lateral expansion of silicon island thin films on metallic substrate. This behavior leads to a critical lateral size (width) below which the islands deform primarily elastic during cycling.
- The prediction was consistent with the experimental *in-situ* stress measurements, suggesting stress reversibility for sufficiently small islands.
- A modified Stoney equation was also developed to quantify the interfacial shear stresses and it was found that the interface stresses are ~13.4 to 18.4 MPa.
- Based on the stress measurements, it was concluded that sliding along the interface can significantly relax stress within the islands, as the estimated interfacial shear stresses are much smaller than the shear yield stress of the substrate (here the titanium thin-film current collector).

7.1.4. Chapter 5

- A theory of film delamination for elastic islands was used to explain the size effects observed in delamination of silicon thin film patterned electrodes.
- The theory predicts length scales associated with interfacial delamination of silicon islands on substrates in the presence of interfacial sliding.
- The analysis was presented for plane strain as well as axisymmetric cases, in the presence of edge and center interface cracks.
- The theory also explains why the crack spacing in a continuous film is so correlated with the size effect observed in the delamination of islands from the substrate.

7.1.5. Chapter 6

- A plastic failure mechanism, based on incremental accumulation of plastic strain or ratcheting, was discussed for silicon islands on substrate.
- It was shown that as soon as the lateral size of the islands becomes large enough to induce plastic deformation in the islands, the ratcheting mode could get activated.
- The ratcheting mechanism is based on the hypothesis that mechanical properties of lithiated silicon as well as interface can change with the lithium content in the system during lithiation and delithiation. It was shown that differential sliding resistance/yield stress from half-cycle to half-cycle, could activate a range of tensile as well as compressive ratcheting mechanisms.
- The theoretical study highlights the importance of avoiding plastic deformation in silicon electrodes, which can be achieved by keeping the lateral size of the islands below the minimum size needed for the onset of plastic deformation.

7.2. Limitations of the present work, and possible future research directions

7.2.1. Chapter 2

- The model developed here has been focused on identifying various coupling phenomena in the diffusion process, while keeping the mechanics part of the problem in a simple form which is indeed sufficient for the case of hydrogen diffusion in nickel. However, for other materials systems, such as lithium diffusion in silicon, plastic deformation, amorphization, large deformation and phase transformations should also be taken into consideration.

7.2.2. Chapter 3

- The instability presented in this chapter was a diffusion-limited study. One could consider the case in which diffusion and reaction front evolve simultaneously, where the effect of diffusion-induced stresses on the reaction rate needs to be studied as well.
- In this study, we have focused on the stress effect on the kinetics of the problem. Stress effect on the thermodynamics of the problem should also be taken into consideration in the future. Large diffusion-induced stresses could affect the driving force for reaction, making the otherwise spontaneous reaction energetically unfavorable.

7.2.3. Chapter 4

- The effect of interfacial sliding on the mechanisms of crack formation in continuous silicon thin films on substrate could be studied. The model presented in this chapter was based on strain localization in the film. It is also possible to have instantaneous fracture in the film (most likely in the first charging and discharging cycle). The effect of interfacial sliding on the instantaneous fracture could also be studied.

- Further experiments could also shed more light on the problem of crack formation in silicon thin film electrodes. For instance, one insightful study would be the effect of different current collectors (or substrates) on the crack patterns, and whether or not the crack spacing changes remarkably from one current collector to another.
- Another interesting question to ask is whether a very thin film, e.g. 50 nm thick film, fractures after a large number of cycles. The importance of such a study lies in the fact that some theoretical studies based on the Griffith criterion predict that there is a critical size for the film thickness, below which the film does not fracture. The existing literature suggests that this critical size is ~130 nm. However, significant plastic deformation could also induce fracture in films thinner than this critical size, possibly after sufficient number of cycles, even under small cycling rates. It is therefore insightful to study the long-cycle behavior of sub-critical thin films.
- Direct experimental measurement of sliding resistance at the interface between lithiated silicon and the underlying metallic current collector is also crucial.

7.2.4. Chapter 5

- Although the simple theory presented here predicts size effects in delamination of silicon islands, factors such as charging/discharging rate, plasticity within the film and substrate could also play important roles and require further investigation.
- To our knowledge, there is no systematic study of delamination in patterned electrodes on different substrates. It is also important to study the potential effect of plastic deformation in the substrate on the film delamination.

7.2.5. Chapter 6

- The ratcheting phenomenon studied here could be further studied in continuous films rather than in finite islands. Such a study can shed light on the mechanism of crack formation in a continuous thin film.
- Effects of film/substrate roughness on the onset of ratcheting could also be added to the model and requires further investigation.

Appendix

Equations (3.22, 3.24, 3.25) read

$$\tilde{i}_n\tilde{r} = \exp[\frac{\mu}{4}(f_{avg}(\tilde{r}) - 4f)]\frac{df}{\partial\tilde{r}}, \qquad f_{avg}(1) = 0, \tag{3.22}$$

$$\tilde{i}_n\tilde{r} = \exp[\frac{\mu}{4}(p(0) - 4p)]\frac{dp}{\partial\tilde{r}}, \qquad p_{avg}(1) = 0, \tag{3.24}$$

$$\tilde{i}_n\tilde{r} = \exp[-\mu q]\frac{dq}{\partial\tilde{r}}, \qquad q_{avg}(1) = 0. \tag{3.25}$$

These equations imply that f, p and q are increasing functions of $\tilde{r}$, and therefore f_{avg}, p_{avg} and q_{avg} are also increasing functions of $\tilde{r}$.

$$0 = f_{avg}(1) > f_{avg}(\tilde{r}) > f_{avg}(0) = f(0) \qquad \text{for} \qquad 1 > \tilde{r} > 0 \tag{A.1}$$

By dividing Eq. (3.25) by Eq. (3.22), and knowing that $f_{avg}(\tilde{r}) < 0$ for $1 > \tilde{r} \geq 0,$ we obtain

$$\frac{\frac{dq}{d\tilde{r}}}{\frac{df}{d\tilde{r}}} = \exp[\mu(q-f)]\exp[\frac{\mu}{4}f_{avg}(\tilde{r})] < \exp[\mu(q-f)] \text{ for } 1 > \tilde{r} > 0. \tag{A.2}$$

Now suppose that $q(0) < f(0) < 0$. This implies that there exists a sufficiently small ε for which $q(\varepsilon) < f(\varepsilon)$. According to Equation (A.2), $\frac{dq}{d\tilde{r}}(\tilde{r} = \varepsilon) < \frac{df}{d\tilde{r}}(\tilde{r} = \varepsilon)$, and

consequently $q(\tilde{r}) < f(\tilde{r})$ for all $\tilde{r} > \varepsilon$. Hence, $q_{avg}(\tilde{r}) < f_{avg}(\tilde{r})$ for all $\tilde{r} > \varepsilon$, including for $\tilde{r} = 1$, i.e. $q_{avg}(1) < f_{avg}(1) = 0$, which is in contradiction with Equation (3.25), i.e. $q_{avg}(1) = 0$. Therefore the assumption $q(0) < f(0)$ is invalid, and therefore, $q(0) > f(0)$.

Similarly, by deviding Equation (3.24) by Equation (3.22), we obtain

$$\frac{\frac{dp}{d\tilde{r}}}{\frac{df}{d\tilde{r}}} = \exp[\mu(p-f)]\frac{\exp[\frac{\mu}{4} f_{avg}(\tilde{r})]}{\exp[\frac{\mu}{4} p(0)]}, \quad \text{for} \quad 1 \geq \tilde{r} > 0, \tag{A.3}$$

and since $f_{avg}(\tilde{r}) \geq f(0)$,

$$\frac{\frac{dp}{d\tilde{r}}}{\frac{df}{d\tilde{r}}} > \exp[\mu(p-f) - \frac{\mu}{4}\{p(0) - f(0)\}], \quad \text{for} \quad 1 \geq \tilde{r} > 0. \tag{A.4}$$

Now suppose that $p(0) > f(0)$. This implies that there exists a sufficiently small ε for which $p(\varepsilon) > f(\varepsilon)$, and $\frac{dp}{d\tilde{r}}(\tilde{r} = \varepsilon) > \frac{df}{d\tilde{r}}(\tilde{r} = \varepsilon)$. Therefore, according to Equation (A.4), $p(\tilde{r}) > f(\tilde{r})$ for all $\tilde{r} > \varepsilon$. Hence, $p_{avg}(\tilde{r}) > f_{avg}(\tilde{r})$ for all $\tilde{r} > \varepsilon$, including for $\tilde{r} = 1$, i.e. $p_{avg}(1) > f_{avg}(1) = 0$, which is in contradiction with Equation (3.24), i.e. $p_{avg}(1) = 0$. Therefore the assumption $p(0) > f(0)$ is invalid, and therefore, $p(0) < f(0)$.

In summary, we have shown that

$$p(0) < f(0) < q(0) < 0\,. \tag{A.5}$$

But since $p_{avg}(1) = f_{avg}(1) = q_{avg}(1) = 0$, and since f, p and q are increasing functions of $\tilde{r}$, Equation (A.5) implies that

$$p(1) > f(1) > q(1)\,. \tag{A.6}$$

Now, rewriting Equations (3.22, 3.24, 3.25) for $\tilde{r} = 1$, we obtain

$$\frac{df}{d\tilde{r}}(\tilde{r} = 1) = \tilde{i}_n \exp[\mu f(1)]\,, \tag{A.7}$$

$$\frac{dp}{d\tilde{r}}(\tilde{r} = 1) = \tilde{i}_n \exp[\mu p(1) - \frac{\mu}{4} p(0)]\,, \tag{A.8}$$

$$\frac{dq}{d\tilde{r}}(\tilde{r} = 1) = \tilde{i}_n \exp[\mu q(1)]\,. \tag{A.9}$$

Finally, from inequalities (A.5, A.6), and Equations (A.7-A.9), it can be seen that

$$\frac{dp}{d\tilde{r}}(\tilde{r} = 1) > \frac{df}{\partial\tilde{r}}(\tilde{r} = 1) > \frac{dq}{d\tilde{r}}(\tilde{r} = 1)\,. \tag{3.23}$$

Bibliography

1. Kasavajjula, U., C.S. Wang, and A.J. Appleby, *Nano- and bulk-silicon-based insertion anodes for lithium-ion secondary cells.* Journal of Power Sources, 2007. **163**(2): p. 1003-1039.
2. Tarascon, J.M. and M. Armand, *Issues and challenges facing rechargeable lithium batteries.* Nature, 2001. **414**(6861): p. 359-367.
3. Armand, M. and J.M. Tarascon, *Building better batteries.* Nature, 2008. **451**(7179): p. 652-657.
4. Kim, M.H., et al., *Electrochemical characteristics of a Si/Ge multilayer anode for lithium-ion batteries.* Journal of the Korean Physical Society, 2006. **49**(3): p. 1107-1110.
5. Boukamp, B.A., G.C. Lesh, and R.A. Huggins, *All-Solid Lithium Electrodes with Mixed-Conductor Matrix.* Journal of the Electrochemical Society, 1981. **128**(4): p. 725-729.
6. Netz, A., R.A. Huggins, and W. Weppner, *The formation and properties of amorphous silicon as negative electrode reactant in lithium systems.* Journal of Power Sources, 2003. **119**: p. 95-100.
7. Kim, I., P.N. Kumta, and G.E. Blomgren, *Si/TiN nanocomposites - Novel anode materials for Li-ion batteries.* Electrochemical and Solid State Letters, 2000. **3**(11): p. 493-496.
8. Kim, I., G.E. Blomgren, and P.N. Kumta, *Nanostructured Si/TiB2 composite anodes for Li-ion batteries.* Electrochemical and Solid State Letters, 2003. **6**(8): p. A157-A161.
9. Kim, H., et al., *The insertion mechanism of lithium into Mg2Si anode material for Li-ion batteries.* Journal of the Electrochemical Society, 1999. **146**(12): p. 4401-4405.
10. Hwang, S.M., et al., *Lithium Insertion in SiAg Powders Produced by Mechanical Alloying.* Electrochemical and Solid State Letters, 2001. **4**(7): p. A97-A100.
11. Beaulieu, L.Y., et al., *The electrochemical reaction of Li with amorphous Si-Sn alloys.* Journal of the Electrochemical Society, 2003. **150**(2): p. A149-A156.
12. Graetz, J., et al., *Nanocrystalline and thin film germanium electrodes with high lithium capacity and high rate capabilities.* Journal of the Electrochemical Society, 2004. **151**(5): p. A698-A702.
13. Graetz, J., et al., *Highly reversible lithium storage in nanostructured silicon.* Electrochemical and Solid State Letters, 2003. **6**(9): p. A194-A197.
14. Maranchi, J.P., A.F. Hepp, and P.N. Kumta, *High capacity, reversible silicon thin-film anodes for lithium-ion batteries.* Electrochemical and Solid State Letters, 2003. **6**(9): p. A198-A201.
15. Maranchi, J.P., et al., *Interfacial properties of the a-Si/Cu : active-inactive thin-film anode system for lithium-ion batteries.* Journal of the Electrochemical Society, 2006. **153**(6): p. A1246-A1253.
16. Sethuraman, V.A., et al., *In situ measurements of stress evolution in silicon thin films during electrochemical lithiation and delithiation.* Journal of Power Sources, 2010. **195**(15): p. 5062-5066.
17. Soni, S.K., et al., *Thickness effects on the lithiation of amorphous silicon thin films.* Scripta Materialia, 2011. **64**(4): p. 307-310.

18. Sethuraman, V.A., et al., *In Situ Measurements of Stress-Potential Coupling in Lithiated Silicon.* Journal of the Electrochemical Society, 2010. **157**(11): p. A1253-A1261.
19. Sethuraman, V.A., et al., *In situ measurement of biaxial modulus of Si anode for Li-ion batteries.* Electrochemistry Communications, 2010. **12**(11): p. 1614-1617.
20. Li, J.C., et al., *Crack Pattern Formation in Thin Film Lithium-Ion Battery Electrodes.* Journal of the Electrochemical Society, 2011. **158**(6): p. A689-A694.
21. Wang, Y.H., et al., *Investigation of crack patterns and cyclic performance of Ti-Si nanocomposite thin film anodes for lithium ion batteries.* Journal of Power Sources, 2012. **202**: p. 236-245.
22. Xiao, X., et al., *Improved cycling stability of silicon thin film electrodes through patterning for high energy density lithium batteries.* Journal of Power Sources, 2011. **196**(3): p. 1409-1416.
23. Soni, S.K., et al., *Diffusion Mediated Lithiation Stresses in Si Thin Film Electrodes.* Journal of the Electrochemical Society, 2012. **159**(9): p. A1520-A1527.
24. Zhao, K.J., et al., *Inelastic hosts as electrodes for high-capacity lithium-ion batteries.* Journal of Applied Physics, 2011. **109**(1).
25. Takamura, Y., et al., *Spatial firing properties of lateral septal neurons.* Hippocampus, 2006. **16**(8): p. 635-644.
26. Takamura, T., et al., *High capacity and long cycle life silicon anode for Li-ion battery.* Journal of Power Sources, 2006. **158**(2): p. 1401-1404.
27. Chan, C.K., X.F. Zhang, and Y. Cui, *High capacity Li ion battery anodes using Ge nanowires.* Nano Letters, 2008. **8**(1): p. 307-309.
28. Chan, C.K., et al., *High-performance lithium battery anodes using silicon nanowires.* Nature Nanotechnology, 2008. **3**(1): p. 31-35.
29. Liu, X.H., et al., *Lithium fiber growth on the anode in a nanowire lithium ion battery during charging.* Applied Physics Letters, 2011. **98**(18).
30. Liu, X.H., et al., *Anisotropic Swelling and Fracture of Silicon Nanowires during Lithiation.* Nano Letters, 2011. **11**(8): p. 3312-3318.
31. Liu, X.H., et al., *Ultrafast Electrochemical Lithiation of Individual Si Nanowire Anodes.* Nano Letters, 2011. **11**(6): p. 2251-2258.
32. Huang, J.Y., et al., *In Situ Observation of the Electrochemical Lithiation of a Single SnO2 Nanowire Electrode.* Science, 2010. **330**(6010): p. 1515-1520.
33. Zhong, L., et al., *Multiple-Stripe Lithiation Mechanism of Individual SnO2 Nanowires in a Flooding Geometry.* Physical Review Letters, 2011. **106**(24).
34. Kushima, A., et al., *Leapfrog Cracking and Nanoamorphization of ZnO Nanowires during In Situ Electrochemical Lithiation.* Nano Letters, 2011. **11**(11): p. 4535-4541.
35. Lee, S.W., et al., *Anomalous Shape Changes of Silicon Nanopillars by Electrochemical Lithiation.* Nano Letters, 2011. **11**(7): p. 3034-3039.
36. Pharr, M., et al., *Kinetics of Initial Lithiation of Crystalline Silicon Electrodes of Lithium-Ion Batteries.* Nano Letters, 2012. **12**(9): p. 5039-5047.
37. Lee, S.W., et al., *Fracture of crystalline silicon nanopillars during electrochemical lithium insertion.* Proceedings of the National Academy of Sciences of the United States of America, 2012. **109**(11): p. 4080-4085.
38. Liu, X.H. and J.Y. Huang, *In situ TEM electrochemistry of anode materials in lithium ion batteries.* Energy & Environmental Science, 2011. **4**(10): p. 3844-3860.

39. Christensen, J. and J. Newman, *Stress generation and fracture in lithium insertion materials.* Journal of Solid State Electrochemistry, 2006. **10**(5): p. 293-319.
40. Christensen, J. and J. Newman, *A mathematical model of stress generation and fracture in lithium manganese oxide.* Journal of the Electrochemical Society, 2006. **153**(6): p. A1019-A1030.
41. Zhang, X.C., A.M. Sastry, and W. Shyy, *Intercalation-induced stress and heat generation within single lithium-ion battery cathode particles.* Journal of the Electrochemical Society, 2008. **155**(7): p. A542-A552.
42. Zhang, X., W. Shyy, and A.M. Sastry, *Numerical simulation of intercalation-induced stress in Li-ion battery electrode particles (vol 154, pg A910, 2007).* Journal of the Electrochemical Society, 2007. **154**(12): p. S21-S21.
43. Deshpande, R., Y.T. Cheng, and M.W. Verbrugge, *Modeling diffusion-induced stress in nanowire electrode structures.* Journal of Power Sources, 2010. **195**(15): p. 5081-5088.
44. Cheng, Y.T. and M.W. Verbrugge, *Evolution of stress within a spherical insertion electrode particle under potentiostatic and galvanostatic operation.* Journal of Power Sources, 2009. **190**(2): p. 453-460.
45. Cheng, Y.T. and M.W. Verbrugge, *Diffusion-Induced Stress, Interfacial Charge Transfer, and Criteria for Avoiding Crack Initiation of Electrode Particles.* Journal of the Electrochemical Society, 2010. **157**(4): p. A508-A516.
46. Cheng, Y.T. and M.W. Verbrugge, *The influence of surface mechanics on diffusion induced stresses within spherical nanoparticles.* Journal of Applied Physics, 2008. **104**(8).
47. Cheng, Y.T. and M.W. Verbrugge, *Evolution of stress within a spherical insertion electrode particle under potentiostatic and galvanostatic operation (vol 190, pg 453, 2009).* Journal of Power Sources, 2011. **196**(4): p. 2430-2431.
48. Cheng, Y.T. and M.W. Verbrugge, *Application of Hasselman's Crack Propagation Model to Insertion Electrodes.* Electrochemical and Solid State Letters, 2010. **13**(9): p. A128-A131.
49. Yang, F.Q., *Interaction between diffusion and chemical stresses.* Materials Science and Engineering a-Structural Materials Properties Microstructure and Processing, 2005. **409**(1-2): p. 153-159.
50. Wang, W.L., S. Lee, and J.R. Chen, *Effect of chemical stress on diffusion in a hollow cylinder.* Journal of Applied Physics, 2002. **91**(12): p. 9584-9590.
51. Bower, A.F., P.R. Guduru, and V.A. Sethuraman, *A finite strain model of stress, diffusion, plastic flow, and electrochemical reactions in a lithium-ion half-cell.* Journal of the Mechanics and Physics of Solids, 2011. **59**(4): p. 804-828.
52. Bower, A.F. and P.R. Guduru, *A simple finite element model of diffusion, finite deformation, plasticity and fracture in lithium ion insertion electrode materials.* Modelling and Simulation in Materials Science and Engineering, 2012. **20**(4).
53. Bhandakkar, T.K. and H.J. Gao, *Cohesive modeling of crack nucleation in a cylindrical electrode under axisymmetric diffusion induced stresses.* International Journal of Solids and Structures, 2011. **48**(16-17): p. 2304-2309.
54. Bhandakkar, T.K. and H.J. Gao, *Cohesive modeling of crack nucleation under diffusion induced stresses in a thin strip: Implications on the critical size for flaw tolerant battery electrodes.* International Journal of Solids and Structures, 2010. **47**(10): p. 1424-1434.
55. Huggins, R.A. and W.D. Nix, *Decrepitation Model For Capacity Loss During Cycling of Alloys in Rechargeable Electrochemical Systems.* Ionics, 2000. **6**(1-2): p. 57-63.

56. Zhao, K.J., et al., *Fracture of electrodes in lithium-ion batteries caused by fast charging.* Journal of Applied Physics, 2010. **108**(7).
57. Woodford, W.H., Y.M. Chiang, and W.C. Carter, *"Electrochemical Shock" of Intercalation Electrodes: A Fracture Mechanics Analysis.* Journal of the Electrochemical Society, 2010. **157**(10): p. A1052-A1059.
58. Zhao, K.J., et al., *Concurrent Reaction and Plasticity during Initial Lithiation of Crystalline Silicon in Lithium-Ion Batteries.* Journal of the Electrochemical Society, 2012. **159**(3): p. A238-A243.
59. Zhao, K.J., et al., *Large Plastic Deformation in High-Capacity Lithium-Ion Batteries Caused by Charge and Discharge.* Journal of the American Ceramic Society, 2011. **94**: p. S226-S235.
60. Grantab, R. and V.B. Shenoy, *Location- and Orientation-Dependent Progressive Crack Propagation in Cylindrical Graphite Electrode Particles.* Journal of the Electrochemical Society, 2011. **158**(8): p. A948-A954.
61. Zhao, K.J., et al., *Fracture and debonding in lithium-ion batteries with electrodes of hollow core-shell nanostructures.* Journal of Power Sources, 2012. **218**: p. 6-14.
62. Newman, J. and W. Tiedemann, *Porous-Electrode Theory with Battery Applications.* Aiche Journal, 1975. **21**(1): p. 25-41.
63. Darling, R. and J. Newman, *Modeling a porous intercalation electrode with two characteristic particle sizes.* Journal of the Electrochemical Society, 1997. **144**(12): p. 4201-4208.
64. Doyle, M., T.F. Fuller, and J. Newman, *Modeling of Galvanostatic Charge and Discharge of the Lithium Polymer Insertion Cell.* Journal of the Electrochemical Society, 1993. **140**(6): p. 1526-1533.
65. Fuller, T.F., M. Doyle, and J. Newman, *Simulation and Optimization of the Dual Lithium Ion Insertion Cell.* Journal of the Electrochemical Society, 1994. **141**(1): p. 1-10.
66. Prussin, S., *The Generation and Distribution of Dislocations by Solute Diffusion.* Journal of the Electrochemical Society, 1961. **108**(9): p. C213-C213.
67. Chenminli, J. and R.F. Mehl, *Physical-Chemistry of Some Microstructural Phenomena.* Metallurgical Transactions a-Physical Metallurgy and Materials Science, 1978. **9**(10): p. 1353-1380.
68. Christensen, J., *Modeling Diffusion-Induced Stress in Li-Ion Cells with Porous Electrodes.* Journal of the Electrochemical Society, 2010. **157**(3): p. A366-A380.
69. Verbrugge, M.W. and Y.T. Cheng, *Stress and Strain-Energy Distributions within Diffusion-Controlled Insertion-Electrode Particles Subjected to Periodic Potential Excitations.* Journal of the Electrochemical Society, 2009. **156**(11): p. A927-A937.
70. Haftbaradaran, H., et al., *Continuum and atomistic models of strongly coupled diffusion, stress, and solute concentration.* Journal of Power Sources, 2011. **196**(1): p. 361-370.
71. Wu, C.H., *Stress-driven diffusion in a deforming and evolving elastic circular tube of single component solid with vacancies.* International Journal of Fracture, 2007. **147**(1-4): p. 227-234.
72. Porter, D.A. and K.E. Easterling, *Phase transformations in metals and alloys*1981, New York: Van Nostrand Reinhold. xii, 446 p.
73. Svoboda, J. and F.D. Fischer, *Vacancy-driven stress relaxation in layers.* Acta Materialia, 2009. **57**(16): p. 4649-4657.

74. Suwanayuen, S. and R.P. Danner, *Gas-Adsorption Isotherm Equation Based on Vacancy Solution Theory.* Aiche Journal, 1980. **26**(1): p. 68-76.
75. Suwanayuen, S. and R.P. Danner, *Vacancy Solution Theory of Adsorption from Gas-Mixtures.* Aiche Journal, 1980. **26**(1): p. 76-83.
76. Ding, L.P. and S.K. Bhatia, *Application of heterogeneous vacancy solution theory to characterization of microporous solids.* Carbon, 2001. **39**(14): p. 2215-2229.
77. Ding, L.P., S.K. Bhatia, and F. Liu, *Kinetics of adsorption on activated carbon: application of heterogeneous vacancy solution theory.* Chemical Engineering Science, 2002. **57**(18): p. 3909-3928.
78. Koter, S. and A.P. Terzyk, *Two-dimensional gas and vacancy solution approaches in the thermodynamic description of adsorption equilibrium.* Journal of Colloid and Interface Science, 2005. **282**(2): p. 335-339.
79. Picu, R.C. and D. Zhang, *Atomistic study of pipe diffusion in Al-Mg alloys.* Acta Materialia, 2004. **52**(1): p. 161-171.
80. Olmsted, D.L., L.G. Hector, and W.A. Curtin, *Molecular dynamics study of solute strengthening in Al/Mg alloys.* Journal of the Mechanics and Physics of Solids, 2006. **54**(8): p. 1763-1788.
81. Prausnitz, J.M., *Molecular thermodynamics of fluid-phase equilibria*. Prentice-Hall international series in the physical and chemical engineering sciences1969, Englewood Cliffs, N.J.,: Prentice-Hall. xiii, 523 p.
82. Shenoy, V.B., P. Johari, and Y. Qi, *Elastic softening of amorphous and crystalline Li-Si Phases with increasing Li concentration: A first-principles study.* Journal of Power Sources, 2010. **195**(19): p. 6825-6830.
83. Qi, Y., et al., *Threefold Increase in the Young's Modulus of Graphite Negative Electrode during Lithium Intercalation.* Journal of the Electrochemical Society, 2010. **157**(5): p. A558-A566.
84. Olmsted, D.L., R. Phillips, and W.A. Curtin, *Modelling diffusion in crystals under high internal stress gradients.* Modelling and Simulation in Materials Science and Engineering, 2004. **12**(5): p. 781-797.
85. Aziz, M.J., P.C. Sabin, and G.Q. Lu, *The Activation Strain Tensor - Nonhydrostatic Stress Effects on Crystal-Growth Kinetics.* Physical Review B, 1991. **44**(18): p. 9812-9816.
86. Barvosa-Carter, W., et al., *Kinetically driven growth instability in stressed solids.* Physical Review Letters, 1998. **81**(7): p. 1445-1448.
87. Haftbaradaran, H., H.J. Gao, and W.A. Curtin, *A surface locking instability for atomic intercalation into a solid electrode.* Applied Physics Letters, 2010. **96**(9).
88. Foiles, S.M., M.I. Baskes, and M.S. Daw, *Embedded-Atom-Method Functions for the Fcc Metals Cu, Ag, Au, Ni, Pd, Pt, and Their Alloys.* Physical Review B, 1986. **33**(12): p. 7983-7991.
89. Angelo, J.E., N.R. Moody, and M.I. Baskes, *Trapping of Hydrogen to Lattice-Defects in Nickel.* Modelling and Simulation in Materials Science and Engineering, 1995. **3**(3): p. 289-307.
90. Song, J. and W.A. Curtin, *A nanoscale mechanism of hydrogen embrittlement in metals.* Acta Materialia, 2011. **59**(4): p. 1557-1569.
91. Hoover, W.G., *Canonical Dynamics - Equilibrium Phase-Space Distributions.* Physical Review A, 1985. **31**(3): p. 1695-1697.

92. Nose, S., *A Unified Formulation of the Constant Temperature Molecular-Dynamics Methods.* Journal of Chemical Physics, 1984. **81**(1): p. 511-519.
93. Hoover, W.G., *Constant-Pressure Equations of Motion.* Physical Review A, 1986. **34**(3): p. 2499-2500.
94. Melchionna, S., G. Ciccotti, and B.L. Holian, *Hoover Npt Dynamics for Systems Varying in Shape and Size.* Molecular Physics, 1993. **78**(3): p. 533-544.
95. Zhao, K.J., et al., *Reactive Flow in Silicon Electrodes Assisted by the Insertion of Lithium.* Nano Letters, 2012. **12**(8): p. 4397-4403.
96. Zhao, K.J., et al., *Lithium-Assisted Plastic Deformation of Silicon Electrodes in Lithium-Ion Batteries: A First-Principles Theoretical Study.* Nano Letters, 2011. **11**(7): p. 2962-2967.
97. Obrovac, M.N., et al., *Alloy design for lithium-ion battery anodes.* Journal of the Electrochemical Society, 2007. **154**(9): p. A849-A855.
98. Johari, P., Y. Qi, and V.B. Shenoy, *The Mixing Mechanism during Lithiation of Si Negative Electrode in Li-Ion Batteries: An Ab lnitio Molecular Dynamics Study.* Nano Letters, 2011. **11**(12): p. 5494-5500.
99. Chevrier, V.L. and J.R. Dahn, *First Principles Studies of Disordered Lithiated Silicon.* Journal of the Electrochemical Society, 2010. **157**(4): p. A392-A398.
100. Chevrier, V.L., J.W. Zwanziger, and J.R. Dahn, *First principles study of Li-Si crystalline phases: Charge transfer, electronic structure, and lattice vibrations.* Journal of Alloys and Compounds, 2010. **496**(1-2): p. 25-36.
101. Kim, H., et al., *Structure and Properties of Li-Si Alloys: A First-Principles Study.* Journal of Physical Chemistry C, 2011. **115**(5): p. 2514-2521.
102. Lee, S.J., et al., *Stress effect on cycle properties of the silicon thin-film anode.* Journal of Power Sources, 2001. **97-8**: p. 191-193.
103. Ryu, J.H., et al., *Failure modes of silicon powder negative electrode in lithium secondary batteries.* Electrochemical and Solid State Letters, 2004. **7**(10): p. A306-A309.
104. Li, H., et al., *A high capacity nano-Si composite anode material for lithium rechargeable batteries.* Electrochemical and Solid State Letters, 1999. **2**(11): p. 547-549.
105. Bourderau, S., T. Brousse, and D.M. Schleich, *Amorphous silicon as a possible anode material for Li-ion batteries.* Journal of Power Sources, 1999. **81**: p. 233-236.
106. Yang, J., M. Winter, and J.O. Besenhard, *Small particle size multiphase Li-alloy anodes for lithium-ion-batteries.* Solid State Ionics, 1996. **90**(1-4): p. 281-287.
107. Winter, M. and J.O. Besenhard, *Electrochemical lithiation of tin and tin-based intermetallics and composites.* Electrochimica Acta, 1999. **45**(1-2): p. 31-50.
108. Maskell, W.C. and J.R. Owen, *Cycling Behavior of Thin-Film Lial Electrodes with Liquid and Solid Electrolytes.* Journal of the Electrochemical Society, 1985. **132**(7): p. 1602-1607.
109. Chen, J., et al., *Mechanical analysis and in situ structural and morphological evaluation of Ni-Sn alloy anodes for Li ion batteries.* Journal of Physics D-Applied Physics, 2008. **41**(2).
110. Beaulieu, L.Y., et al., *Colossal reversible volume changes in lithium alloys.* Electrochemical and Solid State Letters, 2001. **4**(9): p. A137-A140.
111. Laforge, B., et al., *Study of germanium as electrode in thin-film battery.* Journal of the Electrochemical Society, 2008. **155**(2): p. A181-A188.
112. Chen, C.P. and M.H. Leipold, *Fracture-Toughness of Silicon.* American Ceramic Society Bulletin, 1980. **59**(4): p. 469-472.

113. Bagdahn, J. and W.N. Sharpe, *Fatigue of polycrystalline silicon under long-term cyclic loading.* Sensors and Actuators a-Physical, 2003. **103**(1-2): p. 9-15.
114. Griffith, A.A., *Phenomena of Rupture and Flow in Solids.* Asm Transactions Quarterly, 1968. **61**(4): p. 871-&.
115. Freund, L.B. and S. Suresh, *Thin film materials : stress, defect formation, and surface evolution*. 1st pbk. ed2009, Cambridge, England ; New York: Cambridge University Press. xviii, 750 p.
116. Hutchinson, J.W. and Z. Suo, *Mixed-Mode Cracking in Layered Materials.* Advances in Applied Mechanics, Vol 29, 1992. **29**: p. 63-191.
117. Tada, H., P.C. Paris, and G.R. Irwin, *The stress analysis of cracks handbook*. 3rd ed2000, New York: ASME Press. xx, 677 p.
118. Thouless, M.D., *Crack Spacing in Brittle Films on Elastic Substrates.* Journal of the American Ceramic Society, 1990. **73**(7): p. 2144-2146.
119. Ye, T., Z. Suo, and A.G. Evans, *Thin-Film Cracking and the Roles of Substrate and Interface.* International Journal of Solids and Structures, 1992. **29**(21): p. 2639-2648.
120. Xia, Z.C. and J.W. Hutchinson, *Crack patterns in thin films.* Journal of the Mechanics and Physics of Solids, 2000. **48**(6-7): p. 1107-1131.
121. Bai, T., D.D. Pollard, and H. Gao, *Explanation far fracture spacing in layered materials.* Nature, 2000. **403**(6771): p. 753-756.
122. Shenoy, V.B., A.F. Schwartzman, and L.B. Freund, *Crack patterns in brittle thin films.* International Journal of Fracture, 2001. **109**(1): p. 29-45.
123. Yin, H.M., *Fracture saturation and critical thickness in layered materials.* International Journal of Solids and Structures, 2010. **47**(7-8): p. 1007-1015.
124. Huang, R., et al., *Channel-cracking of thin films with the extended finite element method.* Engineering Fracture Mechanics, 2003. **70**(18): p. 2513-2526.
125. Begley, M.R., et al., *Fracture of nanoscale copper films on elastomer substrates.* Applied Physics Letters, 2009. **95**(23).
126. Bai, T.X., D.D. Pollard, and H.J. Gao, *Spacing of edge fractures in layered materials.* International Journal of Fracture, 2000. **103**(4): p. 373-395.
127. Kindle, E.M., *Notes on mud crack and ripple mark in recent calcareous sediments.* Journal of Geology, 1923. **31**(2): p. 138-145.
128. Goehring, L., L. Mahadevan, and S.W. Morris, *Nonequilibrium scale selection mechanism for columnar jointing.* Proceedings of the National Academy of Sciences of the United States of America, 2009. **106**(2): p. 387-392.
129. Li, Q.Y. and K.S. Kim, *Micromechanics of friction: effects of nanometre-scale roughness.* Proceedings of the Royal Society a-Mathematical Physical and Engineering Sciences, 2008. **464**(2093): p. 1319-1343.
130. Hu, M.S. and A.G. Evans, *The Cracking and Decohesion of Thin-Films on Ductile Substrates.* Acta Metallurgica, 1989. **37**(3): p. 917-925.
131. Agrawal, D.C. and R. Raj, *Measurement of the Ultimate Shear-Strength of a Metal Ceramic Interface.* Acta Metallurgica, 1989. **37**(4): p. 1265-1270.
132. Soni, S.K., et al., *Stress Mitigation during the Lithiation of Patterned Amorphous Si Islands.* Journal of the Electrochemical Society, 2012. **159**(1): p. A38-A43.
133. Chason, E. and B.W. Sheldon, *Monitoring stress in thin films during processing.* Surface Engineering, 2003. **19**(5): p. 387-391.

134. Stoney, G.G., *The tension of metallic films deposited by electrolysis.* Proceedings of the Royal Society of London Series a-Containing Papers of a Mathematical and Physical Character, 1909. **82**(553): p. 172-175.
135. Haftbaradaran, H., et al., *Modified Stoney Equation for Patterned Thin Film Electrodes on Substrates in the Presence of Interfacial Sliding.* Journal of Applied Mechanics-Transactions of the Asme, 2012. **79**(3).
136. Haftbaradaran, H., et al., *Method to deduce the critical size for interfacial delamination of patterned electrode structures and application to lithiation of thin-film silicon islands.* Journal of Power Sources, 2012. **206**: p. 357-366.
137. Freund, L.B., *The Stress-Distribution and Curvature of a General Compositionally Graded Semiconductor Layer.* Journal of Crystal Growth, 1993. **132**(1-2): p. 341-344.
138. Brown, M.A., et al., *Thin film substrate systems featuring arbitrary film thickness and misfit strain distributions. Part II: Experimental validation of the non-local stress curvature relations.* International Journal of Solids and Structures, 2007. **44**(6): p. 1755-1767.
139. Feng, X., Y. Huang, and A.J. Rosakis, *On the Stoney formula for a thin film/substrate system with nonuniform substrate thickness.* Journal of Applied Mechanics-Transactions of the Asme, 2007. **74**(6): p. 1276-1281.
140. Ngo, D., et al., *Thin film/substrate systems featuring arbitrary film thickness and misfit strain distributions. Part I: Analysis for obtaining film stress from non-local curvature information.* International Journal of Solids and Structures, 2007. **44**(6): p. 1745-1754.
141. Freund, L.B., *Substrate curvature due to thin film mismatch strain in the nonlinear deformation range.* Journal of the Mechanics and Physics of Solids, 2000. **48**(6-7): p. 1159-1174.
142. Shen, Y.L., S. Suresh, and I.A. Blech, *Stresses, curvatures, and shape changes arising from patterned lines on silicon wafers.* Journal of Applied Physics, 1996. **80**(3): p. 1388-1398.
143. Wikstrom, A., P. Gudmundson, and S. Suresh, *Thermoelastic analysis of periodic thin lines deposited on a substrate.* Journal of the Mechanics and Physics of Solids, 1999. **47**(5): p. 1113-1130.
144. Bower, A.F., *Applied mechanics of solids*2010, Boca Raton: CRC Press. xxv, 794 p.
145. Howatson, A.M., P.G. Lund, and J.D. Todd, *Engineering tables and data*1972, London: Chapman and Hall. viii, 167 p.
146. He, M.Y., A.G. Evans, and J.W. Hutchinson, *Convergent debonding of films and fibers.* Acta Materialia, 1997. **45**(8): p. 3481-3489.
147. He, M.Y., A.G. Evans, and J.W. Hutchinson, *Effects of morphology on the decohesion of compressed thin films.* Physica Status Solidi a-Applied Research, 1998. **166**(1): p. 19-35.
148. Yu, H.H., M.Y. He, and J.W. Hutchinson, *Edge effects in thin film delamination.* Acta Materialia, 2001. **49**(1): p. 93-107.
149. Yu, H.H. and J.W. Hutchinson, *Influence of substrate compliance on buckling delamination of thin films.* International Journal of Fracture, 2002. **113**(1): p. 39-55.
150. Shen, J. and R. Raj, *Silicon-oxycarbide based thin film anodes for lithium ion batteries.* Journal of Power Sources, 2011. **196**(14): p. 5945-5950.
151. Bree, J., *Elastic-plastic behaviour of thin tubes subjected to internal pressure and intermittent high-heat fluxes with application to fast-nuclear-reactor fuel elements.* The Journal of Strain Analysis for Engineering Design, 1967. **2**.

152. Jansson, S. and F.A. Leckie, *Mechanical-Behavior of a Continuous Fiber-Reinforced Aluminum Matrix Composite Subjected to Transverse and Thermal Loading.* Journal of the Mechanics and Physics of Solids, 1992. **40**(3): p. 593-612.
153. Begley, M.R. and A.G. Evans, *Progressive cracking of a multilayer system upon thermal cycling.* Journal of Applied Mechanics-Transactions of the Asme, 2001. **68**(4): p. 513-520.
154. Huang, M., Z. Suo, and Q. Ma, *Plastic ratcheting induced cracks in thin film structures.* Journal of the Mechanics and Physics of Solids, 2002. **50**(5): p. 1079-1098.
155. Suresh, S., *Fatigue of materials*. 2nd ed1998, Cambridge ; New York: Cambridge University Press. xxi, 679 p.
156. Haftbaradaran, H. and H.J. Gao, *Ratcheting of silicon island electrodes on substrate due to cyclic intercalation.* Applied Physics Letters, 2012. **100**(12).
157. Tian, Y., A. Timmons, and J.R. Dahn, *In Situ AFM Measurements of the Expansion of Nanostructured Sn-Co-C Films Reacting with Lithium.* Journal of the Electrochemical Society, 2009. **156**(3): p. A187-A191.
158. Kao, D.B., et al., *Two-Dimensional Thermal-Oxidation of Silicon .2. Modeling Stress Effects in Wet Oxides.* Ieee Transactions on Electron Devices, 1988. **35**(1): p. 25-37.
159. Fazzini, P.F., et al., *Modeling stress retarded self-limiting oxidation of suspended silicon nanowires for the development of silicon nanowire-based nanodevices.* Journal of Applied Physics, 2011. **110**(3).
160. Chen, Y.J. and Y.H. Chen, *Modeling silicon dots fabrication using self-limiting oxidation.* Microelectronic Engineering, 2001. **57-8**: p. 897-901.
161. Ma, F.J., et al., *Modeling of Stress-Retarded Thermal Oxidation of Nonplanar Silicon Structures for Realization of Nanoscale Devices.* Ieee Electron Device Letters, 2010. **31**(7): p. 719-721.
162. Kim, I., et al., *Interfacial reaction-dominated full oxidation of 5 nm diameter silicon nanowires.* Journal of Applied Physics, 2012. **112**(9).
163. Khalilov, U., et al., *Self-Limiting Oxidation in Small-Diameter Si Nanowires.* Chemistry of Materials, 2012. **24**(11): p. 2141-2147.
164. Liu, H.I., et al., *Self-Limiting Oxidation of Si Nanowires.* Journal of Vacuum Science & Technology B, 1993. **11**(6): p. 2532-2537.
165. Liu, H.I., et al., *Self-Limiting Oxidation for Fabricating Sub-5 Nm Silicon Nanowires.* Applied Physics Letters, 1994. **64**(11): p. 1383-1385.
166. Buttner, C.C. and M. Zacharias, *Retarded oxidation of Si nanowires.* Applied Physics Letters, 2006. **89**(26).